Biomimicking Human Tactile Sensation using Flexible Tactile Sensors

Shashank Mishra

James Watt School of Engineering

A thesis submitted to the James Watt School of Engineering at the University of Glasgow in partial fulfilment of the requirements for the Degree of

Doctor of Philosophy

October 2024

Abstract

The sense of touch is essential for human interaction with the environment, allowing us to perform tasks ranging from simple actions to intricate procedures. Human tactile perception, through mechanoreceptors in the skin, enables the detection of various stimuli, including pressure, texture, temperature, and vibration. This sensory capability is fundamental to tasks such as grasping objects, maintaining balance, and communicating emotions. Mimicking the complexity of human touch in artificial systems has been a long-standing challenge in robotics, prosthetics, and wearable technology. Achieving human-like sensitivity in machines could transform industries, allowing robots to handle delicate objects, prosthetics to offer better tactile feedback for amputees, and wearables to enhance human-computer interaction. Advances in materials science and flexible electronics have opened new possibilities for developing tactile sensors that replicate the mechanical and sensory functions of human skin. Flexible sensors, which can conform to various surfaces and endure mechanical stress, are key to creating electronic skin (e-skin) capable of sensing pressure, strain, temperature, and other physical stimuli. This thesis explores the development of flexible tactile sensors that bio-mimic human tactile systems for use in robotics and prosthetics, while also leveraging computational simulations to improve design of these sensors.

Towards this, in response to the need for reliable and sensitive strain sensors, this work initially presents stretchable strain sensors that operate over a wide range and exhibit excellent gauge factors. The sensors, composed of elastomer, conductive filler, and graphene–carbon paste (GCP), demonstrated high stretchability and sensitivity. Molecular dynamics simulations showed that adding GCP to the composite material enhances sensor response. A strain sensor with a high gauge factor of 1,834,140 was also

developed. Additionally, a neuromorphic strain sensor system was developed using this piezoresistive sensor and a simulated neuron to mimic the behavior of mechanoreceptors. Applications of this neuromorphic strain sensing system in stretch and angle bending have been successfully demonstrated.

Next, a hybrid sensor system was developed combining capacitive pressure sensors and triboelectric nanogenerators, mimicking both slowly and rapidly adapting mechanoreceptors. The hybrid system successfully detected static and dynamic stimuli and showed good applications for impact detection and slip monitoring. Later, a simulation-based study investigated PDMS based soft capacitive pressure sensors enhanced with ZnO nanowires. Results indicated a significant improvement in sensor sensitivity by ~3 times, especially with vertically aligned ZnO nanowires. This work demonstrates the potential of using simulation methods to optimize sensor design and enhance tactile sensor performance for future applications in robotics, prosthetics, and human-machine interfaces.

Finally, atomistic simulations explored the behavior of water molecules trapped between a graphene and gold interface, which is a common issue in graphene-based devices due to the wet-transfer process. The effect of contaminants like water on the electronic properties of such devices is highly unexplored. The molecular dynamics simulations revealed that when the water film thickness is below 5 Å, it forms an ice-like structure, potentially causing strain in the graphene layer and affecting sensor performance. As the water thickness increases, the water transitions to a liquid state, reducing strain. This study provides critical insights into the challenges posed by trapped water at the graphene-Au interface, which can impact the performance of devices such as graphene-based field-effect transistors (GFETs). The research work presented in this thesis could provide a

foundation for future work in the field of flexible and hybrid sensor systems, with potential applications in robotics, prosthetics, and human-machine interfaces.

List of Publications

Journal Articles:

1. **Mishra, S.,** Liu, F., Shakthivel, D., Rai,B., Georgiev, V., Molecular Dynamics Simulation based Study to Analyse the Properties of Entrapped Water Between Gold and Graphene 2D Interface, *Nanoscale Advances*, 2371-2379 (2024)
2. **Mishra, S.,** Nair, NM., Khandelwal, G., Rai,B., Georgiev, V., Capacitive-Triboelectric based Hybrid Sensor System for Human-like Tactile Perception, *IEEE Sensors Letters*, 8, 5500404 (2024)
3. Min, G., Khandelwal, G., Dahiya, AS., **Mishra, S**., Tang, W., Dahiya, R., Multisource Energy Harvester on Textile and Plants for Clean Energy Generation from Wind and Rainwater Droplets, *ACS Sustainable Chemistry & Engineering*, 12, 695-705 (2024)
4. Kumaresan, Y*., **Mishra, S.***, Ozioko, O., Chirila, R., Dahiya, R., Ultra-High Gauge Factor Strain Sensor with Wide-Range Stretchability, *Advanced Intelligent Systems*, 4 (9), 2200043 (2022) *(*equal contribution)*

Conference Articles:

1. **Mishra, S**., John, D., Kumar, N., Rai, B., Georgiev, V., "Human-Inspired Stretch and Joint-Bend Sensing System Based on Flexible Sensors" accepted in *2023 IEEE SENSORS Conference, Vienna,* Austria, 2023
2. **Mishra, S**., Baghini, M.S., Shathivel, D., Rai, B., Dahiya, R., " sensitivity analysis of ZnO NWs based soft capacitive pressure sensors using finite element modeling", *2022 IEEE FLEPS Conference, Vienna,* Austria, 2022

Book Chapter:

1. Nair, N.M., **Mishra, S.,** Dahiya, R., “Graphene – based touch sensors” Encyclopedia of Materials: Electronics, Edited by Haseeb A.S.M.A., Academic Press, 2023, Pages 54-70

Acknowledgements

I would like to express my sincere gratitude to my supervisor, Prof. Vihar Georgiev, for his unwavering support and invaluable mentorship throughout the last two years of my PhD. I am also deeply thankful to my former supervisor, Prof. Ravinder Dahiya, for his guidance and encouragement during the initial phase of my research. I would also like thank Dr. Beena Rai from Tata Consultancy Services for supporting and mentoring me during my PhD journey.

I feel incredibly fortunate to have worked in two leading research labs—Bendable Electronics and Sensing Technologies (BEST) and the DeepNano group within the James Watt School of Engineering. I extend my heartfelt thanks to all the members of these labs with whom I had the privilege to collaborate. In particular, I would like to thank Dr. Gaurav Khandelwal, Dr. Yogeenth Kumaresan, Dr. Nitheesh Nair, Dr. Dina Anna John, Deepan Neethipathi, Dr. Guanbo Min, Dr. Fengyuan Liu, Dr. Dhayalan Shakthivel, Dr. Mahdieh Shojaei Bhagini, Dr. Naveen Kumar, Dr. Oliver Ozioko, and Radu Chirila for their invaluable support and collaboration.

I would also like to extend my heartfelt thanks to my friends, especially Dr. Ajay Beniwal, Dr. Rudra Mukherjee, Dr. Moupali Chakraborty, Dr. Sofia Sandhu, Dr. Satya Bairagi, Dr. Charchit Kumar, Dr. Bhavani Prasad Yalagala, Dr. Ankit Dixit, Satyam Bhatti, Dr. Dudul Das, Siddharth, Harshad and Himanshu for their constant encouragement and emotional support. I am truly grateful to the European Commission for funding my PhD through the Marie Skłodowska-Curie Innovative Training Network INTUITIVE project.

I would like to extend my deepest gratitude to my parents, Mr. Suresh Chandra Mishra and Mrs. Manju Mishra, for always believing in me and providing care and support throughout my PhD. I would also like to thank my brother Prashant and his wife Shikha,

my nephew Mayank, my niece Shipra, my in-laws (Mr. Amresh Kumar Mishra, Mrs. Nutan Mishra, Dr. Vaibhav and Dr. Snigdha), and my dear wife Indira. Your unconditional love, unwavering support, and constant encouragement have been my pillars of strength, especially during moments of doubt and loneliness. Your faith in me has been invaluable, and I could not have reached this achievement without you by my side.

Table of Contents

List of Figures

List of Tables

Author’s Declaration

I, Shashank Mishra, declare that, except where explicit reference is made to the contribution of others, this thesis is the result of my own work and has not been submitted for any other degree at the University of Glasgow or any other institution.

Where others have provided a scientific and experimental contribution to the work presented in this thesis, a note is provided highlighting their contribution under the heading of the section in which that work is presented.

Chapter 1

Introduction

The sense of touch is fundamental to human existence, guiding us through everyday actions, from the simple act of holding a cup to the intricate procedures performed by surgeons. Whether we're engaging in routine tasks or complex manoeuvres, touch provides the essential sensory information needed for success. This human sense of touch, also known as tactile sensation, is a fundamental aspect of how we interact with our environment. This intricate system allows us to perceive and respond to a variety of stimuli, such as pressure, texture, temperature, and vibrations. Embedded with mechanoreceptors and their connected neural pathways, the skin serves as the principal site for processing tactile information in humans and numerous other animals[1, 2]. Through these mechanoreceptors and their transduction mechanism, humans can discern subtle differences in surface roughness, detect minute changes in temperature, and experience complex tactile feedback that guides our interactions with objects and other beings[3]. These capabilities are essential for performing delicate tasks, maintaining balance, and even communicating emotions through physical contact

1.1. Research Motivation

Biomimicking this complex nature of human touch in artificial systems has long been a challenging goal in the fields of robotics, prosthetics, and wearable technology[4-6]. The

ability to endow machines with a sense of touch that matches human sensitivity could revolutionize numerous industries. For instance, robots equipped with tactile sensors could handle delicate objects with care, prosthetics with enhanced tactile feedback could significantly improve the quality of life for amputees, and wearable devices with advanced touch capabilities could enable new forms of human-computer interaction[7-10].

Recent advancements in materials science and flexible electronics have provided new opportunities for developing tactile sensors that closely mimic the mechanical properties and sensory functions of human skin. Flexible sensors, which can conform to various surfaces and withstand mechanical deformation, are particularly promising for creating artificial skin or electronic skin (e-skin) that can replicate human touch. These sensors are typically composed of flexible substrates integrated with sensing elements that detect pressure, strain, temperature and other physical parameters[11-14].

However, designing flexible sensors that can accurately replicate the nuanced and dynamic nature of human tactile sensation presents several challenges. These challenges include achieving high sensitivity, reliability, and durability within this e-skin sensors[4, 15]. Furthermore, the development of these sensors requires a deep understanding of the biomechanics of human skin, as well as advanced modelling techniques to simulate and optimize sensor performance. Modeling and simulation, utilizing various computational techniques such as molecular dynamics (MD) and finite element methods (FEM), are crucial tools in the design of flexible sensors. They provide a deeper understanding of sensor behaviour, enable optimization and innovation, reduce costs and development time, and ultimately lead to the creation of more reliable and high-performing sensors tailored to specific applications.

Additionally, during the fabrication of key functional materials and interfaces for high-performance tactile sensors, achieving ultra-clean surfaces or interfaces is highly challenging[16]. Unwanted foreign particles or materials often get deposited at these surfaces. For instance, in Graphene based Field Effect Transistors (GFETs), the wet transfer process of graphene onto metallic substrates like gold can trap water molecules. These foreign particles, particularly water, form specific structural configurations that significantly impact the electrical and mechanical properties of the sensors. However, the structure of these trapped water molecules and their influence on properties of GFETs based sensors properties remain unexplored.

1.2. Objectives and key findings

The aim of this thesis is to understand human tactile sensation and then leveraging it to develop artificial flexible e-skin sensors (as shown in schematic Figure 1.1) which can meet following objectives:

- To develop e-skin tactile sensors that biomimics the human tactile perception process.
- To develop novel artificial strain sensing system based on advanced flexible strain sensors using carbon-based nanomaterials as sensing layer. Further, to study the effect of materials compositions in sensing layer on the performance of the strain sensor.
- To develop pressure sensor that can detect both static and dynamic pressure stimuli simultaneously just like human skin.
- To leverage modelling and simulation for designing better tactile sensors.
- To understand the structure and effect of unwanted foreign particles like water on the performance of GFETs.

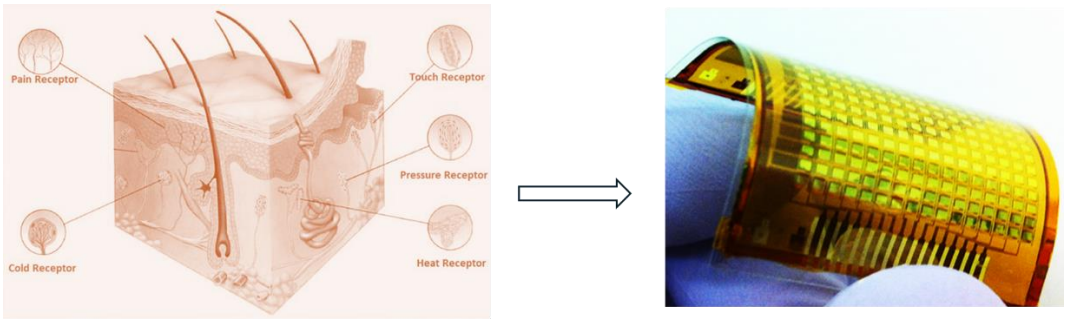

Figure 1.1: Schematic illustration depicting the main objective of this thesis. In this thesis, development of bioinspired e-skin sensors by leveraging the biophysical principles of human tactile sensation process has been presented.

The key findings/outcomes of this thesis are:

1. Developed neuromorphic strain sensing systems consisting of a flexible strain sensor, a wheatstone bridge, and a simulated neuron to detect stretching and bending movements. This involved fabricating stretchable strain sensors with tunable gauge factors and wide-range stretchability by combining elastomer (Ecoflex), conductive filler, and graphene-carbon paste (GCP), including sensors with an unprecedented gauge factor of 1,834,140.
2. Developed novel hybrid pressure sensing system based on stacking triboelectric and capacitive pressure sensors that can detect both static and dynamic quantities of input pressure stimulus simultaneously.
3. Theoretical study on incorporation on ZnO nanowires in PDMS based pressure sensor indicated that the addition of ZnO NWs enhanced the sensitivity of PDMS based sensors by ~3 times. Further, vertical ZnO NWs based sensors show better sensitivity than sensors with lateral ZnO NWs.
4. Atomistic simulations study revealed that trapped water molecules at the graphene–Au interface (present in few GFETs) form unusual ice-like structures when the

water film is thinner than 5 Å, potentially causing strain in the graphene layer and thus affecting the performance of these sensors.

1.3. Structure of thesis

Following the current chapter introduction, this thesis is organised as follows:

Chapter 2 covers the biophysical principles of human tactile sensation, detailing the types and functioning mechanisms of skin mechanoreceptors. It introduces the concept of e-skin and tactile sensors, elaborating on various types of tactile sensors and their transduction mechanisms. This chapter also provides an in-depth discussion of state-of-the-art tactile sensors, particularly pressure and strain sensors, along with their functional materials and fabrication methods.

Chapter 3 describes a strain sensing system that integrates a flexible strain sensor, a wheatstone bridge, and a simulated neuron, designed to detect stretching and bending movements. This chapter initially discusses the development and sensing properties of a flexible strain sensor made from an elastomer, carbon-based nanomaterials, and GCP. Later, the sensor is then incorporated into a circuit with a simulated Leaky-Integrate-and-Fire neuron, creating a system that generates neural spike signals, mimicking the function of neurons connected to skin mechanoreceptors.

Chapter 4 presents a hybrid pressure sensing system, combining a capacitive pressure sensor and a triboelectric nanogenerator to detect both static and dynamic pressure stimuli. This chapter focuses on the fabrication process, sensor performance, and the application of the system in hardness assessment, slip detection, and vibration sensing.

Chapter 5 details finite element method (FEM) simulations on soft capacitive pressure sensors, which incorporate ZnO nanowires within a polydimethylsiloxane (PDMS) dielectric material. These simulations investigate the piezoelectric properties of the ZnO NWs and their impact on sensor sensitivity, as well as how the orientation and aspect ratio of the NWs affect the mechanical properties and sensitivity of the sensors.

Chapter 6 discusses atomistic simulations of the graphene–Au interface, where water molecules often become trapped during the transfer process. Using molecular dynamics (MD) simulations, the study explores the structural variations of trapped water and the traction–separation curve at the graphene-gold interface at 300 K. This research is particularly relevant for understanding GFETs used in pressure sensors, where unwanted water molecules can impact sensor performance.

Chapter 7 summarizes the thesis's key contributions and provides recommendations for future work in the field.

Chapter 2

Literature Review

2.1. Introduction

Human sense of touch is a sophisticated and multifaceted system, capable of detecting a wide range of stimuli such as pressure, texture, strain, shear, temperature, and vibration[17, 18]. This tactile sensation is crucial for various tasks, from object manipulation to social interactions. Replicating this complex sense in artificial systems presents a significant challenge but also offers immense potential for applications in robotics, prosthetics, and wearable devices[7, 8, 10].

Recent advancements in flexible electronics and materials science have opened new avenues for the development of tactile sensors that can closely mimic human skin. These sensors, designed to be both flexible and sensitive, aim to replicate the mechanical and sensory properties of human tactile receptors[19-23]. However, creating sensors that can accurately and reliably mimic the nuanced tactile sensations of human skin remains a formidable task[3, 24].

In this chapter, the current understanding of human tactile sense perception mechanism as well as about different flexible e-skin sensors and their fabrication techniques will be discussed. Initially, the underlying principles of human touch sense will be discussed. Following this, concept of e-skin and its associated sensors will be introduced to understand how we can biomimic the human skin touch sense mechanism. Later, various design approaches and materials used in the development of flexible tactile sensors (especially pressure and strain sensors) will be discussed. Finally, the current challenges in developing these tactile sensors and how these sensors can be used to create artificial sensing system will also be discussed. This work contributes to the ongoing efforts to bridge the gap between human sensory perception and artificial tactile systems, paving the way for more responsive and human-like interactions in technology.

2.2. Human Skin tactile mechanism

In mammals, including humans, and other animal species, the skin is divided into physiologically, morphologically, and functionally distinct regions, such as hairy skin and non-hairy (glabrous) skin[25]. These skin regions vary in tactile sensitivity due to the different distribution patterns of tactile sensors within them[26, 27]. The sense of touch is derived from various sensory receptors embedded in the skin, including mechanoreceptors (which respond to mechanical stimuli), thermoreceptors (which respond to temperature changes), and nociceptors (which respond to pain)[17]. This section will primarily focus on mechanoreceptors and the touch mechanism. Several review papers provide detailed descriptions of skin mechanoreceptors, their afferent fibers, and the mechanotransduction process[1, 17, 26-29]. A summary of these mechanoreceptors and the touch mechanism is presented below.

2.2.1. Skin Mechanoreceptors

Skin mechanoreceptors present at different depths within the skin detect mechanical stimuli such as pressure, vibration, or movement on the skin's surface[1]. They are categorized into two types: slow-adapting receptors (SA-I and SA-II), which respond to static and quasi-static stimuli, providing a sustained response to a stable and constant stimulus; and fast-adapting receptors (FA-I and FA-II), which react to dynamic stimuli like vibrations[1, 30, 31]. These receptors are connected to specialized nerve fibers that vary in structure and conduction velocity[1]. Figure 2.1 illustrates the skin's mechanoreceptors and the nerves that innervate them and Table 2.1 details the characteristics of glabrous skin mechanoreceptors. Figure 2.2 depicts response properties of low-threshold glabrous cutaneous mechanoreceptors.

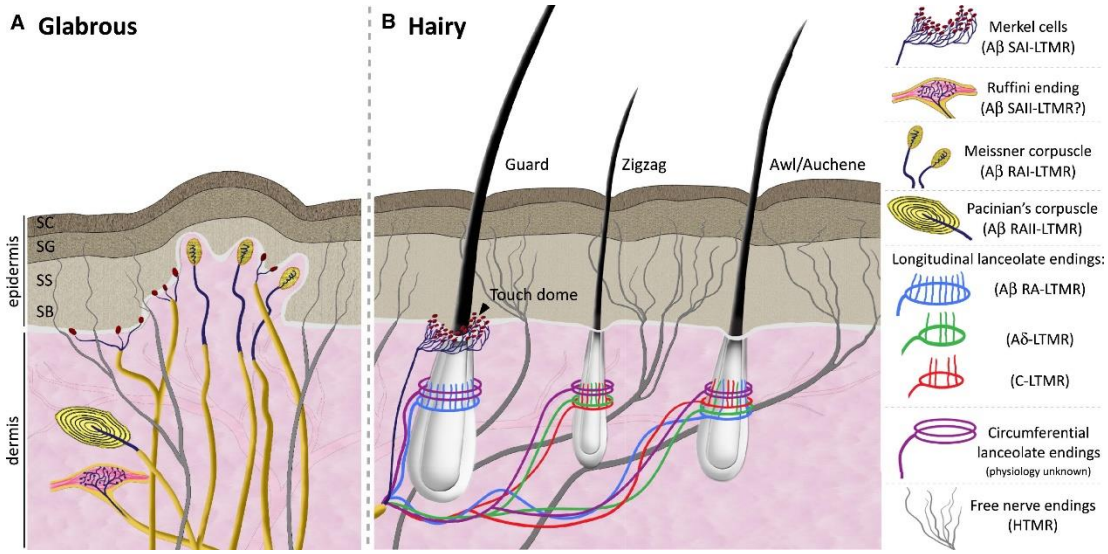

Figure 2.1: Different mechanoreceptors present in (a) Glabrous and (b) Hairy Skin [1] (Copyright © 2013 Elsevier)

Table 2.1: Properties of glabrous skin mechanoreceptors[4]

	FA I Meissner	**SAI Merkel**	**FAII Pacinian**	**SA II Ruffini**
Receptive Field radius (mm)	1.5-2	1.5-2	>10	>5
Spatial Acuity (mm)	3-4	0.5	10+	7+

Responsive to	Dynamic skin perturbations at relatively low frequency (~5-50 Hz)	Dynamic skin perturbations at low frequency (~<5 Hz)	High frequency vibration (~40-400 Hz)	Mostly to static deformations
Location at fingertip	Dermal papillage of the fingertip	Fingertip epidermis layer	Dermal and subcutaneous tissue; distributed throughout the hand	Dermal and subcutaneous tissue; distributed throughout the hand
Density at fingertip	70-140/cm^2	70-140/cm^2	20/cm^2	50/cm^2

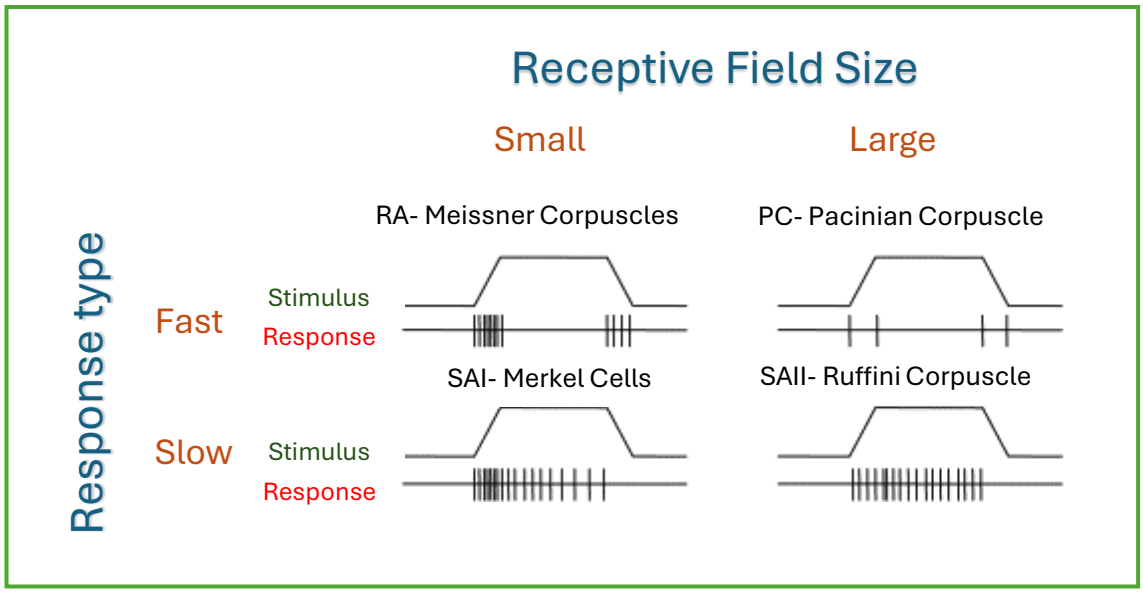

Figure 2.2: Response properties of low-threshold glabrous mechanoreceptors.

2.2.2. Cutaneous touch mechanism

Figure 2.3 illustrates the flowchart of the mechanotransduction mechanism involved for touch sense perception in the skin, showing how mechanical stimuli acting on skin surface are detected and subsequently converted into electrical signals. Mechanotransduction is

a fundamental process that enables organisms to perceive mechanical changes in their environment, such as pressure, stretch, and vibration, through specialized sensory receptors embedded in the skin.

When a mechanical stimulus is applied to the skin, it is first detected by cutaneous mechanoreceptors. These receptors are finely tuned to respond to various types of mechanical stimuli, conveying four essential types of information: modality, location, intensity, and timing[4]. Modality refers to the type of stimulus, such as a gentle touch, vibration, stretch, or injurious force**.** Location indicates the specific area on the skin where the stimulus is applied. Intensity reflects the strength of the stimulus, while timing conveys the duration and temporal pattern of the stimulus.

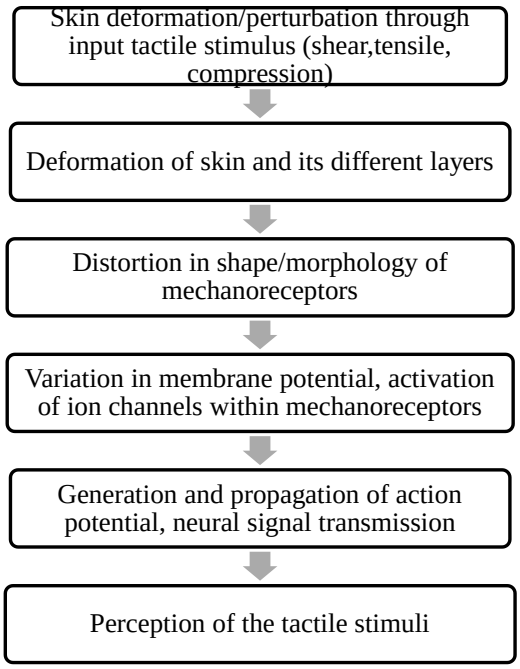

Figure 2.3: Flowchart of human tactile perception mechanism

After detection of input stimulus by mechanoreceptors they transduce the mechanical energy into an electrical signal by generating a change in membrane potential, known as the receptor potential (Figure 2.4 (a))[18, 28, 31]. This is the first critical step in the

mechanotransduction process. The receptor potential is a graded response, meaning its magnitude varies with the intensity of the stimulus. The stronger the stimulus, the greater the change in membrane potential. This receptor potential is then converted into a neural pulse code, where the information is encoded in the form of action potentials, or "spikes," when the receptor potential crosses a threshold value (Figure 2.4 (b))[31, 32]. And then these spike signals are transmitted along the sensory neurons. The frequency of these action potentials is proportional, to some extent, to the amplitude of the receptor potential[26, 33]. This encoding process allows the nervous system to interpret the strength and nature of the mechanical stimulus, facilitating appropriate responses or sensations.

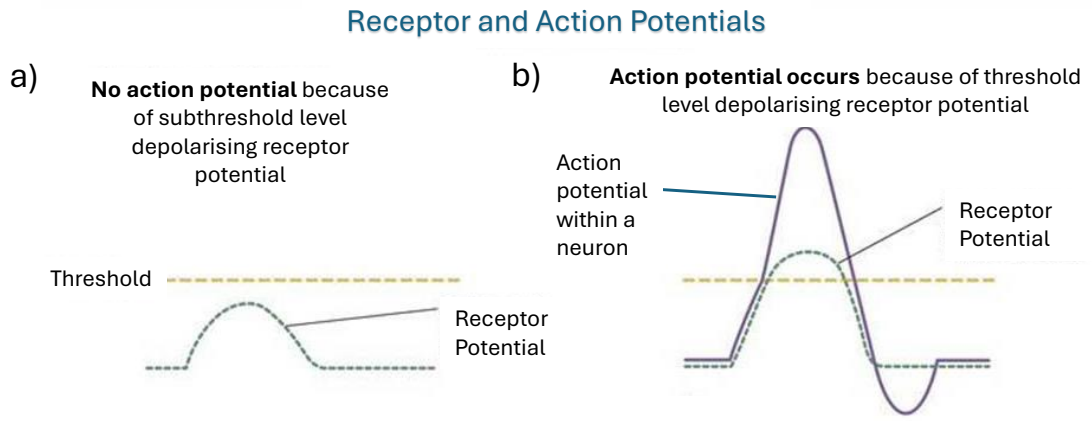

Figure 2.4: Spiking mechanism of a mechanoreceptor (a) Receptor potential below threshold (b)Receptor potential above threshold giving rise to an action potential or a spike in nerve attached to the mechanoreceptor.

Understanding this process requires a comprehensive grasp of several interrelated factors. First, the biomechanics of the skin play a crucial role in how mechanical stimuli are transferred and filtered as they move through the various layers of the skin. The skin's structural properties, including its elasticity, thickness, and composition, significantly influence the initial detection of stimuli by mechanoreceptors[33, 34].

Second, it is essential to consider the mechanoreceptors themselves—specialized cells that are adapted to detect specific types of mechanical changes. These receptors are equipped with ion channels that respond to mechanical deformation by allowing ions to flow across the cell membrane, thereby initiating the receptor potential[2, 28, 35, 36]. Additionally, the other cells and tissues in the skin, such as connective tissue, hair follicles, and underlying muscle layers, contribute to how the mechanical stimulus is transmitted and perceived[1, 26, 27]. The interactions between these structures can modulate the stimulus before it even reaches the mechanoreceptors, influencing the final sensory output.

Finally, the structure and gating mechanisms of ion channels within the mechanoreceptors are crucial for the accurate transduction of mechanical stimuli[2, 36, 37]. These ion channels are responsible for converting the mechanical deformation of the receptor membrane into a biochemical signal, ultimately leading to the generation of action potentials as discussed previouly. I will now briefly discuss about this mechanosensitive ion-channels present within the mechanoreceptors.

2.2.3. Mechanosensitive ion-channels

Ion channels are pore-forming membrane proteins that allow ions to pass through the channel pore, and they are found in all cells of the body[2, 28, 33, 36, 38]. In mechanoreceptors, these channels play a crucial role in maintaining the resting membrane potential and regulating action potentials by controlling ion flow across the membrane. They are composed of specific transmembrane proteins surrounded by lipid molecules.

Ion channels can be selective, permitting only certain ions like Na^+, K^+, Ca^{2+}, or Cl^- to pass through, or non-selective, allowing multiple types of ions to move through[27, 36, 39, 40]. Based on their gating mechanisms, ion channels can be classified as follows:

- **Voltage-Gated Channels**: Activated by changes in membrane potential, these channels, such as voltage-gated sodium and potassium channels, are typically selective to specific ions[17, 41].
- **Mechanosensitive Channels**: Activated by changes in lipid tension around the transmembrane protein, examples include DEG/ENaC channels and piezo channels. These channels can be either selective or non-selective[2, 17, 35, 36, 39, 40, 42].
- **Lipid-Gated Channels**: Activated by the binding of certain chemicals to the transmembrane protein, these channels are involved in neurotransmission and synaptic processes[27, 43].
- **pH-Gated Channels**: Triggered by changes in pH near the membrane protein, with ASIC channels being a key example[2].

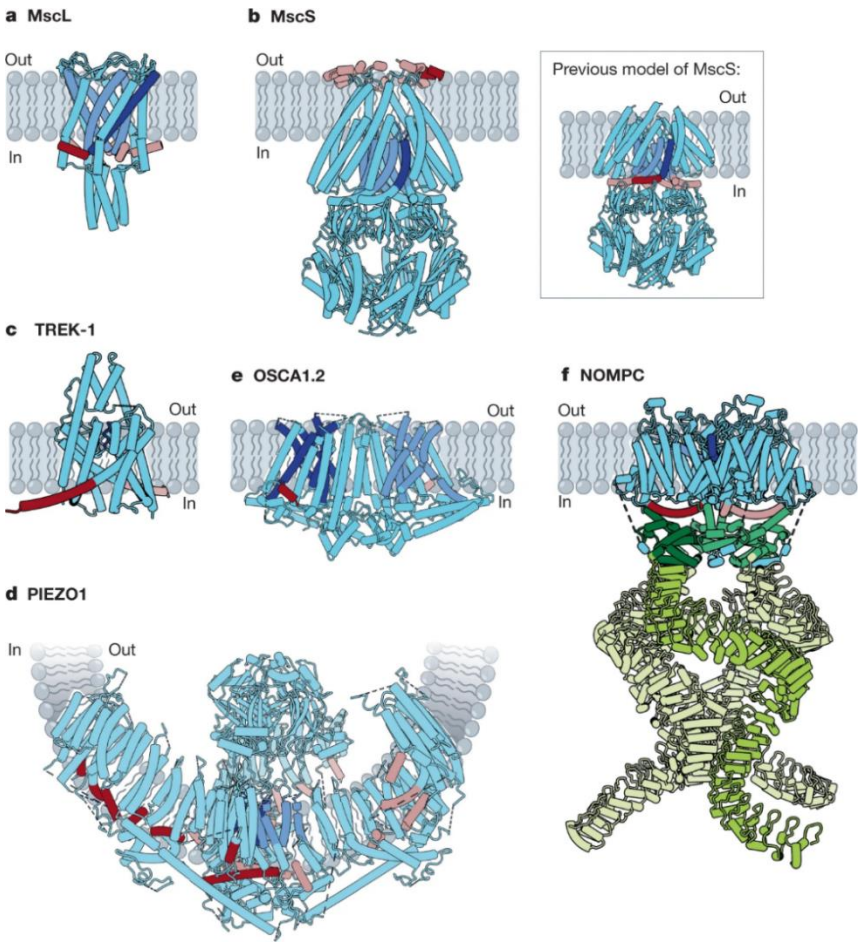

Figure 2.5: Various mechanosensitive ion-channels present in mammals[39] (Copyright © 2020, Springer Nature Limited)

In mechanoreceptors, mechanosensitive channels are the first to respond, detecting shear, tension, or pressure on the skin. Subsequently, voltage-gated channels activate to regulate membrane potential and initiate action potentials[44, 45]. Figure 2.5 illustrates structures of few mechanosensitive ion channels.

2.3. E-skin and its sensors

As discussed in previous section, skin has numerous receptors that sense external tactile stimuli. Inspired by this biophysical mechanism of skin, development of flexible electronic devices consisting of multiple sensors resembling skin sensory receptors has attracted considerable attention in recent years to provide sensory and/or haptic feedback

in growing areas such as robotics, prosthetics, human-machine interactive systems etc as depicted in Figure 2.6[4, 6, 15, 20, 46]. These electronic devices popularly known as electronic skin or e-skin are flexible, stretchable, and often made of self-healing material that mimics the properties and functionalities of human skin[5, 8, 13, 46-52]. It is embedded with electronic sensors and circuits, to detect various stimuli like pressure[12, 23, 53-55], temperature[8, 13, 56, 57], strain[19, 58-62], humidity[63-66], etc.

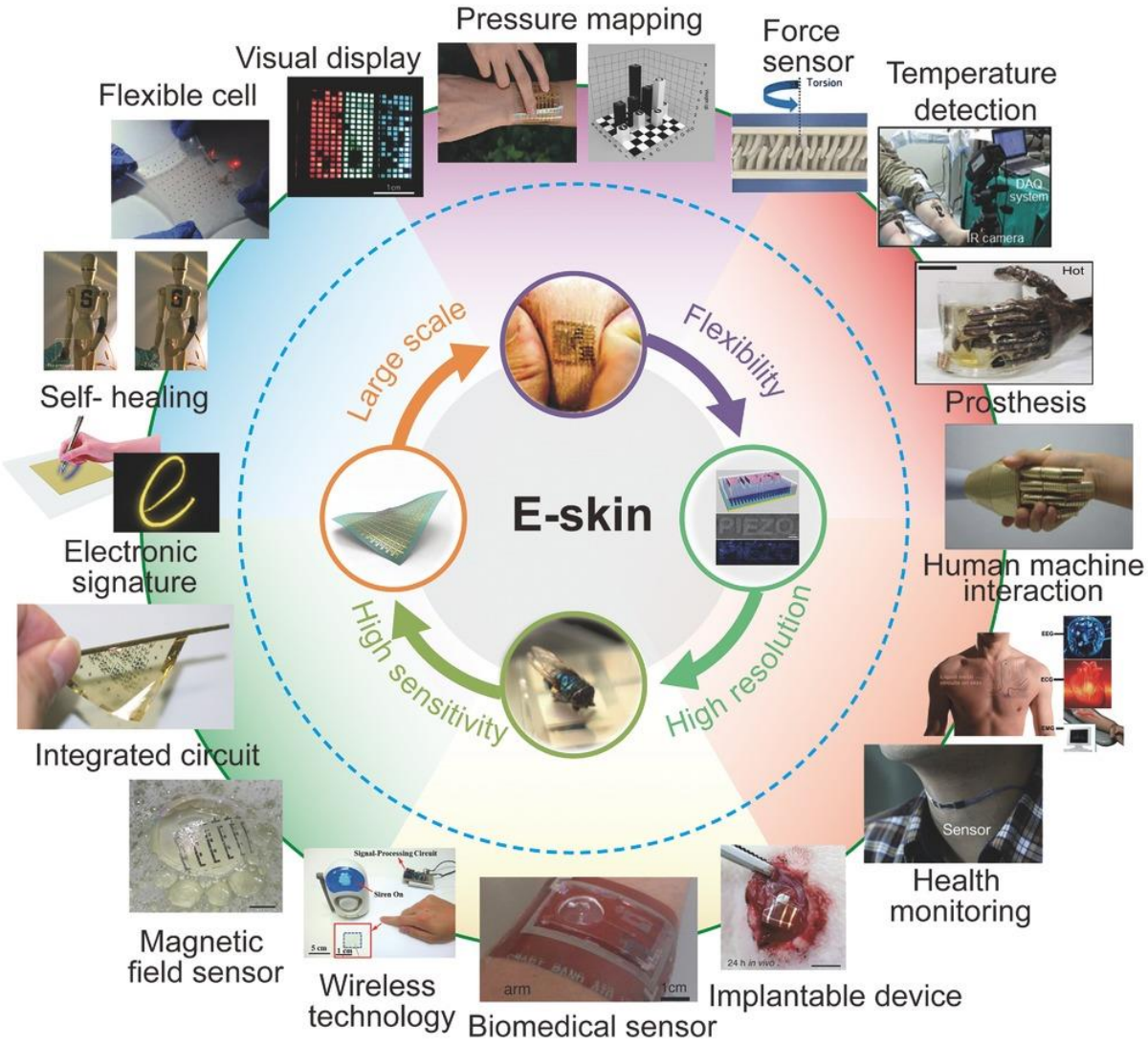

Figure 2.6: E-skin properties and their applications in current times[51].

The key components of an e-skin device include flexible substrate (like PDMS), physical sensors (flexible/rigid), power sources, flexible interconnects, and read out circuits or data

processing units[51]. Out of all these components, development of flexible sensors for e-skins has gained attention in recent times. There are various types of sensors embedded in e-skin like temperature, pressure, strain etc[67]. Among these sensors, pressure and strain sensors, which imitate the biological mechanoreceptors responsible for our sense of touch, have gained significant attention. These sensors are crucial in developing artificial systems capable of providing human-like tactile experiences.

Tactile sensors, which convert applied pressure or strain into electrical signals, are essential components of flexible electronics. This field has evolved into an interdisciplinary domain, bringing together device and system engineering, signal processing, and material sciences, and now incorporates emerging artificial intelligence technologies. In next few sections, I will discuss in detail about different types of these physical tactile sensors, materials involved, fabrication techniques and their applications.

2.3.1. Types of tactile sensors

Figure 2.7 depicts different type of sensors present in e-skin. Mechanical sensors like strain and pressure sensors typically employ various transduction mechanisms, including resistive, piezoresistive, capacitive, piezoelectric, and triboelectric methods as shown in Figure 2.7[67]. While resistive, piezoresistive, and capacitive sensors are more established technologies, they face challenges in achieving high spatial resolution and require an external power supply to operate. Piezoelectric sensors are also well-established and holds promise for self-powered sensors. Additionally, triboelectric sensors are emerging as a self-powered option, utilizing the triboelectrification or contact electrification effect. I will now discuss about these sensors in brief below.

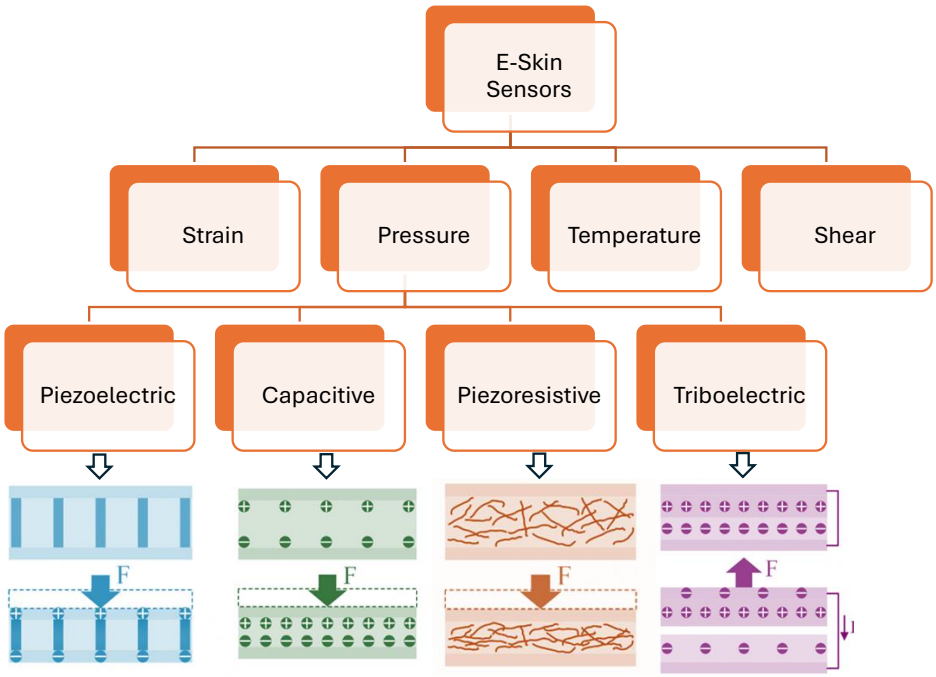

Figure 2.7: Types of e-skin sensors and their classification based on physical principles involved.

2.3.1.1. Piezoresistive Sensors

Piezoresistive resistive sensors work by converting mechanical deformations—such as pressure or strain—into electrical signals. Piezoresistive sensors operate by detecting changes in resistance when mechanical strain or pressure is applied. This resistance is determined by the equation $R = \rho L/A$, where ρ is the material's resistivity, L is the conductor's length, and A is the cross-sectional area. The resistance change in these sensors can be attributed to two main factors: (1) changes in intrinsic resistance and (2) variations in contact resistance[68]. Intrinsic resistance changes are primarily due to alterations in the material's electronic band structure during deformation, which is observed in materials like graphene[58], graphene oxide[69], metal dichalgonides[70] and CNTs[71]. These changes, driven by stress-induced shifts in electronic properties, are widely used in mechanical sensors, with material structure significantly influencing

sensing performance. Contact resistance variations arise from changes in the density of the conductive material, contact area, and conductive paths formed by distortion[68, 72].

When these sensors experience uniaxial strain, their electrical response is defined by the resistance values R_0 (the initial resistance without deformation) and R (the resistance under deformation). The sensitivity of these strain sensors is measured by the gauge factor (GF), calculated as $GF=(\Delta R/R_0)/(\Delta l/l_0)$, where Δl is the change in length and l_0 is the initial length of the sensor[68].

Simple resistive strain sensors, such as metal strain gauges, have relatively gauge factor, typically ranging from 1 to 5[21, 72, 73]. To improve sensitivity, especially on flexible substrates like polydimethylsiloxane (PDMS), metallic thin films with intricate geometric patterns (e.g., serpentine or kirigami) are used[74]. When the device is stretched, the change in geometry alters its dimensions, resulting in a change in electrical resistance. Enhancing sensitivity further, techniques like creating microcracks in the metallic films have shown promising results, though device stability remains a concern[75].

Polymer nanocomposites offer an alternative solution by combining viscoelastic polymers like PDMS or Ecoflex with conductive fillers, which can be 1D, 2D, or 3D nanomaterials like graphene[58, 76], carbon nanotubes (CNT)[77, 78], carbon black[79] etc. These polymer nanocomposite- based sensors are not only lightweight and flexible but also provide accurate and reliable sensing capabilities. Figure 2.8 shows an example polymer nanocomposite based resistive transparent strain sensor made using PDMS and carbon nanotubes developed by Chen et al[80], it’s performance and application in mouth opening detection

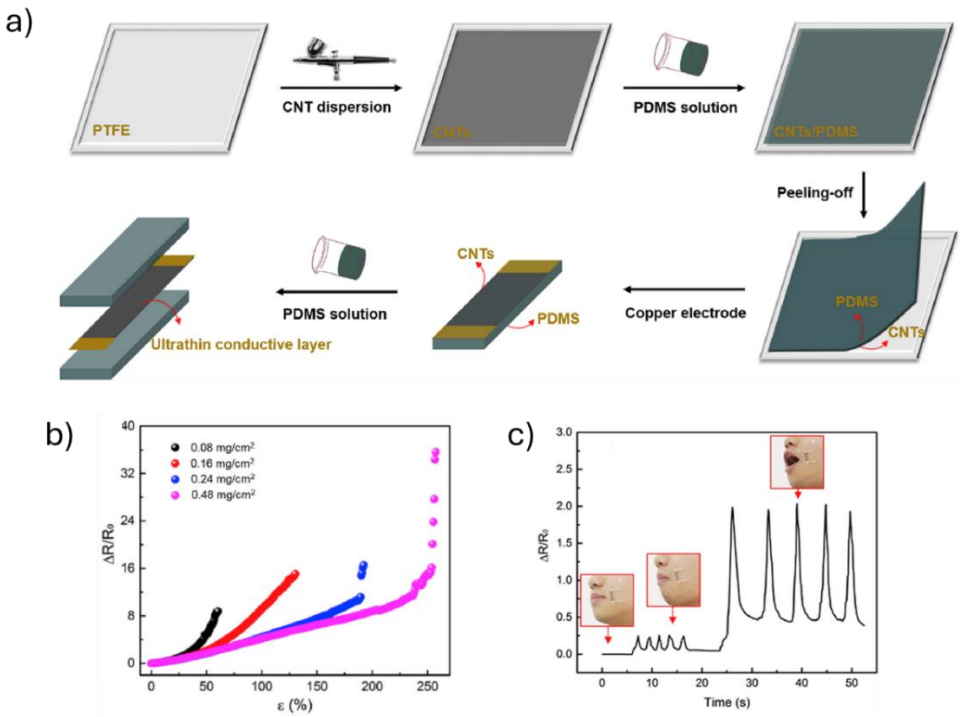

Figure 2.8: An example PDMS-CNT piezo resistive strain sensor (a) Schematic illustrations of fabrication procedures for PDMS/CNTs/PDMS strain sensor, (b) Resistance change variation in these sensors at different CNT concentrations and (c) mouth opening detection using this sensor[80](Copyright© 2019 Elsevier Ltd.)

2.3.1.2. Capacitive Sensors

In capacitive physical sensors, external mechanical stimuli are translated into changes in capacitance. The capacitance (C) of a parallel plate capacitor can be calculated using the formula $C=\varepsilon A/d$ where ε is the dielectric constant or relative permittivity of the dielectric, A is the surface area of the parallel plates and d is the distance between the plates. The distance d is affected by normal forces, while the area A responds to tensile strain and shear forces. Capacitive sensors offer high sensitivity, low power consumption, and better temperature stability. However, their sensitivity is limited by the area A, which decreases as the device size reduces[23, 72]. Increasing the sensitivity of capacitive sensors remains a challenge.

Typically, capacitive sensors consist of a dielectric layer with two electrodes. To enhance sensitivity, low modulus dielectrics (such as Ecoflex or PDMS) are often used due to their

ability to undergo large deformations[72, 81]. Despite this, the response time and sensitivity of these sensors can be affected by the incompressible and viscoelastic nature of the elastomeric dielectrics. To address this issue, researchers have developed dielectric materials with various microstructures [57, 82, 83](e.g., micro pyramids, pores, beads, and cylinders) or embed them with other high dielectric materials like ZnO nanowires[84], barium titanate particles[85] etc. to improve their performance.

Figure 2.9 depicts couple of recently developed capacitive sensors. Figure 2.9(a-e) shows fabrication method, structure, design and performance of a 3d-printed PDMS based capacitive pressure sensor with microgroves[86]. Due to this presence of this microgroves the sensitivity of these sensors increased 8100 times when compared to planar PDMS based pressure sensors in the pressure range of 0-0.2 kPa. Similarly, Figure 2.9(f-g) shows a capacitive pressure sensor and it's performance developed by Kumaresan et al[87] where ZnO interlayers were added between the electrodes and PDMS dielectric to improve its' sensitivity.

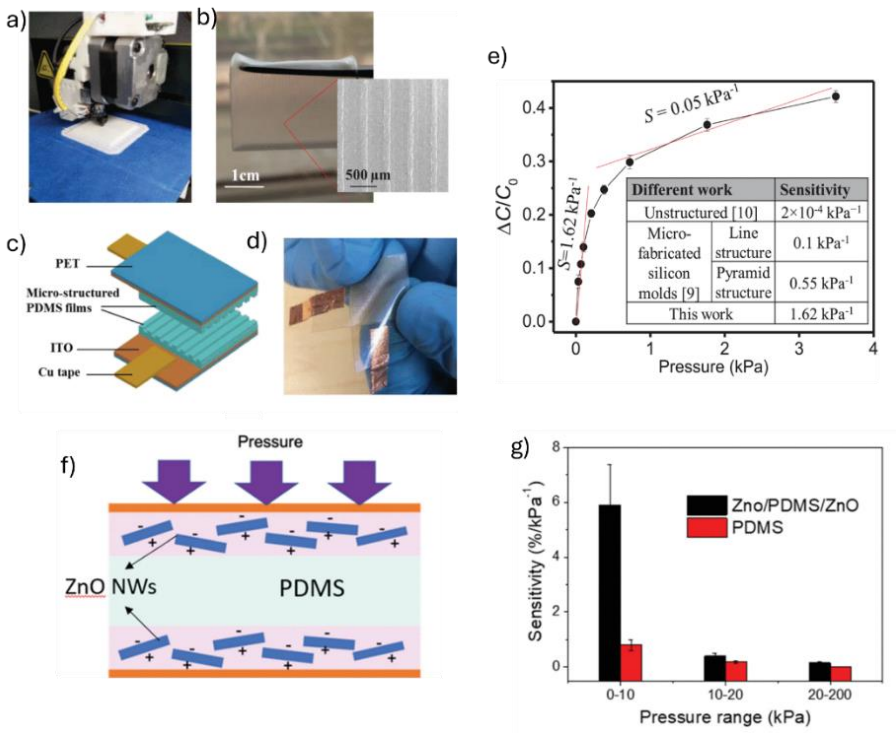

Figure 2.9: Examples of capacitive pressure sensor (a) 3D-printed pressure sensor[86], (b) Optical microscope image of the printed PDMS based sensor with microgrooves[86], (c) Structure of this PDMS based sensor[86] (d) an actual image of the sensor[86], (e) Sensor performance[86], (f) structure of ZnO-PDMS-ZnO pressure sensor developed by Kumaresan et al.[87] (g) performance of this sensor[87]

2.3.1.3. Piezoelectric Sensors

Piezoelectric sensors convert mechanical input into electrical signals through the principle of electromechanical coupling. These sensors work on the piezoelectric effect, where materials generate electrical charges in response to applied mechanical force, pressure, or strain. When subjected to mechanical force, a potential difference, known as piezoelectric potential, develops between the top and bottom electrodes. This potential arises from the displacement of cations and anions within the piezoelectric material, creating a microscale dipole moment. The collective polarization of these dipoles results in a macroscopic potential, or "piezopotential," along the direction of strain[67, 72].

Traditional piezoelectric sensors, typically made from ceramics like lead zirconium titanate (PZT)[88], offer the advantage of being energy-autonomous. However, these materials lack flexibility and contain toxic lead, making them unsuitable for wearable

applications. To address these limitations, two main strategies have been explored to enhance flexibility in piezoelectric devices: (i) using inherently soft materials and (ii) innovating device structures[68]. Recent advances in material science and nanotechnology have introduced flexible materials such as inorganic nanomaterials and organic/inorganic hybrid networks[20, 89]. Among these approaches, various soft piezoelectric materials—such as Glycine−Chitosan[90], ZnO nanowires[91], and poly(vinylidene fluoride-co-trifluoroethylene) (P(VDF-TrFE))[92]—have been explored for developing soft piezoelectric generators and sensors. Below Figure 2.10 depicts the fabrication method and performance as well as working mechanism of a pressure sensor composed of an organic ferroelectric, namely single protonated 1,4-diazabicyclo[2.2.2]octane fluoroborate ([Hdabco]BF_4) embedded in PVDF polymer[93]. This piezoelectric pressure sensor showed a high sensitivity of 0.4 V/kPa and a linear response for external compressive pressures that ranged between 1.6 and 12.8 kPa.

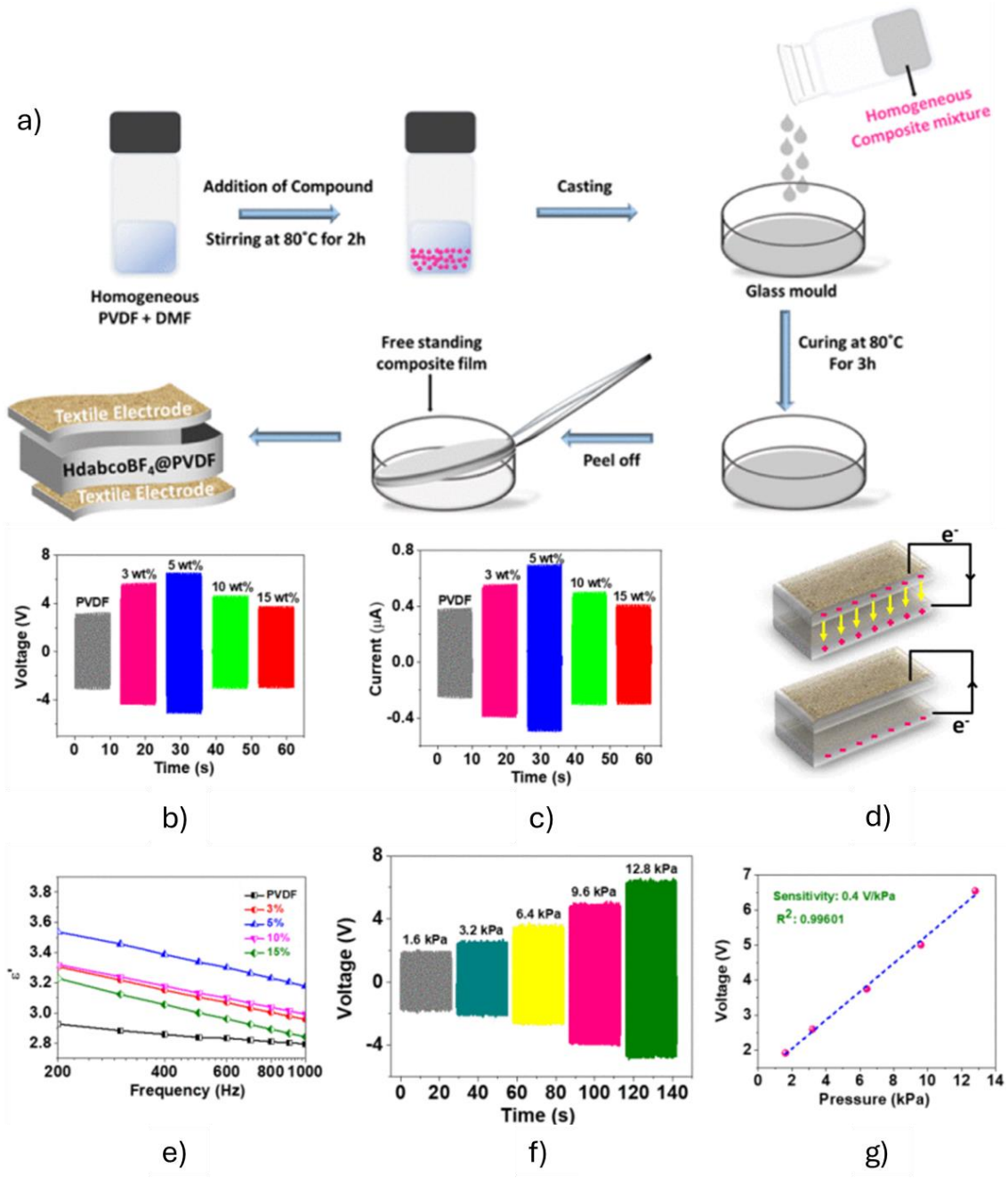

Figure 2.10: An example piezoelectric sensor[93] (a) fabrication method of [Hdabco]BF_4@PVDF sensor(b) output voltage and (b) current obtained from varied wt% composites devices of [Hdabco]BF_4 @PVDF at a dynamic pressure of 12.8 kPa and a frequency of 8 Hz. (c) Schematic diagram illustrating the working principle of a piezoelectric device. (d) Real part of complex dielectric permittivity spotted as a function of frequency at room temperature. (e) Output response from the best performing 5 wt% [Hdabco]BF_4 @PVDF device as a function of applied pressure. (f) Calculated sensitivity of the self-powered piezoelectric pressure sensor[93] ((a-g) Copyright © 2023, IEEE)

2.3.1.4. Triboelectric Sensors

Triboelectric physical sensors are self-powered sensors that convert mechanical signals into electrical signals using triboelectric effects. Recently, triboelectric nanogenerators

(TENGs) have been extensively studied in this field. In 2012, Wang et al.[94] introduced the first transparent TENG designed for a self-powered pressure sensor. TENGs can operate in four modes: (i) free-standing mode, (ii) vertical-contact separation mode, (iii) lateral sliding mode, and (iv) single-electron mode[95]. Among these, the single-electron mode and vertical-contact separation mode are commonly used in physical sensors. The performance of a TENG is influenced by the magnitude and frequency of the mechanical stimuli[68, 95]. To improve the performance and sensitivity of triboelectric nanogenerators (TENGs), two main strategies have been explored: (i) selecting materials from opposite ends of the triboelectric series (one being electropositive and the other electronegative) and (ii) modifying surface morphologies to increase the contact area and thus enhance the triboelectric effect[67, 96-98]. These approaches have led to the development of soft, skin-like TENGs designed for biomechanical energy harvesting and tactile sensing[95, 96]. High-performance soft TENGs have been created by combining elastomers with ionic hydrogels as the electrification layer and electrode, respectively[99]. These self-powered pressure sensors exhibit exceptional stretchability (with a uniaxial strain of 1160%) and transparency (with an average visible light transmittance of 96.2%). The stretchable TENGs demonstrated pressure sensitivity (approximately 0.013 kPa^{-1}), making them suitable for applications like artificial e-skin for touch and pressure detection.

Figure 2.11 shows an example TENG based pressure sensor composed of polyvinylidene fluoride and polyvinylpyrrolidone electrospun fibers-based surfaces as active layers[100]. The working mechanism of this device is based on the coupling effect between the triboelectrification and electrostatic induction. Figure 2.11(d) shows the maximum current output as a function of pressure, with results averaged over five cycles per

pressure while Figure 2.11(e) depicts its output current and its sensitivity at different pressure values.

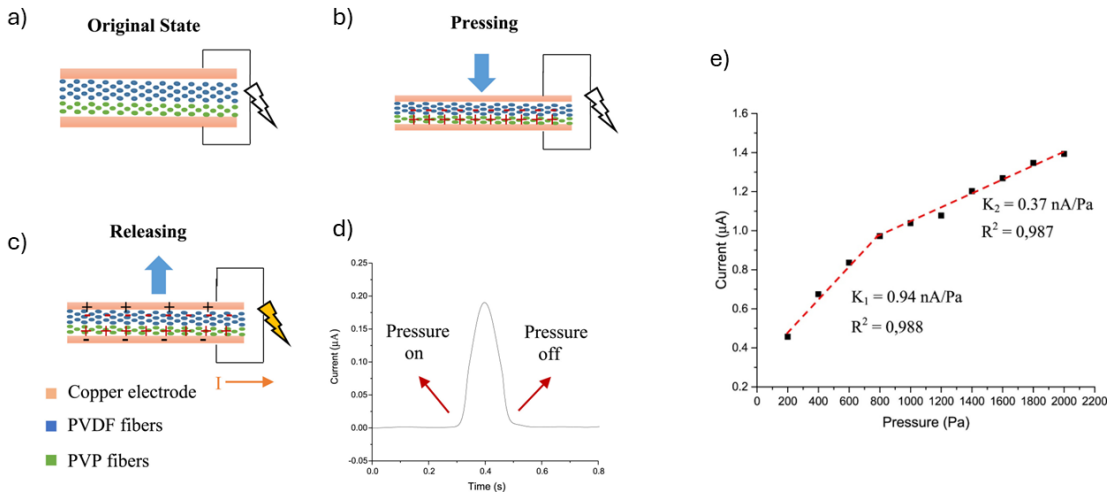

Figure 2.11:An example triboelectric pressure sensor composed of PVDF and PVP fibers (a-c) structure and working mechanism of this triboelectric sensor (b) variation of current in the time domain due to one contact-separation caused by one finger tap (c) current output as a function of the pressures in the range from 200 to 2000 Pa[100] (a-e Copyright © 2018 Elsevier Ltd.).

2.3.2. Materials for physical tactile sensors

Typically, physical tactile sensors like pressure or strain sensors are composed of two kinds of materials i.e., a substrate material and an active material. In some sensors like in capacitive and piezoresistive sensors, electrode materials are also needed. In this section, I will discuss about these materials in brief:

2.3.2.1. Substrate materials:

Substrate materials play a crucial role in the fabrication of tactile sensors, providing the foundation on which the sensing elements and other components are built. The choice of substrate material depends on factors like flexibility, biocompatibility, thermal stability, and mechanical properties, which are critical for the sensor's intended application[101]. Below is some common substrate materials used in tactile sensors:

- **Polymers:**
  - **Polydimethylsiloxane (PDMS):** A widely used silicone-based elastomer known for its flexibility, biocompatibility, and ease of processing. It is ideal for applications that require stretchable and conformable sensors[101, 102].
  - **Polyimide (PI):** Known for its excellent thermal stability, mechanical strength, and flexibility, polyimide is commonly used in flexible electronics and high-temperature applications[103].
  - **Polyurethane (PU):** Offers good elasticity, toughness, and resistance to wear, making it suitable for durable tactile sensors[104].
  - **Polyethylene Terephthalate (PET):** A flexible and transparent polymer that is often used in low-cost, flexible sensors and electronic devices[105, 106].
  - **Ecoflex:** A highly stretchable silicone-based elastomer used for soft and flexible tactile sensors, especially in applications requiring large deformations[107].
- **Textiles and Fabrics:** Offer good flexibility and breathability. They are often coated with conductive materials like conductive polymers to create the sensing elements[72, 108-111].
- **Paper and Paper-like Materials:** A biodegradable and flexible substrate that can be used in low-cost, disposable sensors.[63, 65, 112]
- **Metal Foils:** Copper and aluminium foils are used in flexible printed circuits and sensors due to its excellent electrical conductivity[113, 114].
- **Hydrogels:** Simple/Ionic hydrogels serve as soft, stretchable substrates that can also act as the sensing material in some tactile sensors, particularly in wearable and biomedical applications[51, 60, 67, 115].

These substrate materials are selected based on the specific requirements of the tactile sensor application, such as flexibility, stretchability, durability, and biocompatibility.

They provide the necessary support while allowing the sensor to maintain its functional properties under various conditions.

2.3.2.2. Active materials:

Active materials in tactile sensors are those that directly respond to external stimuli (such as pressure, touch, or strain) and convert these mechanical inputs into electrical signals. The choice of active material is crucial as it determines the sensor's sensitivity, response time, durability, and overall performance. Below are some common active materials used in the fabrication of tactile sensors:

- **Piezoelectric Materials**
  - **Lead Zirconate Titanate (PZT)**: A widely used piezoelectric ceramic that generates an electrical charge in response to applied mechanical stress. It is known for its high sensitivity but is rigid and brittle[88].
  - **PVDF and its copolymers (e.g., P(VDF-TrFE))**: Flexible piezoelectric polymers that are used in applications requiring flexibility and stretchability[12, 116].
  - **ZnO Nanowires**: Employed for their excellent piezoelectric properties at the nanoscale, making them suitable for highly sensitive tactile sensors[59, 87, 117].
  - **Barium Titanate ($BaTiO_3$):** Another piezoelectric ceramic used for its high piezoelectric coefficients, though it is less flexible than polymeric alternatives like PVDF[85].
- **Piezoresistive Materials**
  - **Carbon Nanotubes (CNTs):** Known for their high electrical conductivity and mechanical strength, CNTs change resistance under mechanical deformation, making them ideal for piezoresistive sensors[71, 80, 118-120].

- **Graphene:** A single layer of carbon atoms in sp2 hybridisation with exceptional electrical properties that changes resistance when subjected to strain or pressure[47, 58, 76, 121, 122].
- **Carbon Black:** A conductive filler used in composite materials that exhibit piezoresistive behavior when integrated with flexible polymers[79, 120].
- **Conductive Polymers (e.g., Polypyrrole, PEDOT:PSS):** Polymers that exhibit changes in electrical resistance under mechanical strain, making them suitable for flexible and stretchable sensors[123-126].

❖ **Capacitive Materials**

- **Dielectric Elastomers (e.g., PDMS, Ecoflex):** Used as the dielectric layer in capacitive sensors. These materials undergo changes in dielectric properties when deformed, affecting the capacitance[101, 127].
- **Ionic Liquids and Hydrogels:** Act as stretchable and flexible dielectric materials that can significantly alter capacitance under mechanical stress[60, 128-131].

❖ **Triboelectric Materials**

- **Polytetrafluoroethylene (PTFE):** Known for its strong negative triboelectric properties, PTFE is commonly used in triboelectric nanogenerators (TENGs)[94, 95, 98].
- **Nylon:** Exhibits positive triboelectric properties and is often paired with materials like PTFE in TENGs[132, 133].

These active materials are often chosen and engineered based on the specific requirements of the tactile sensor application, such as sensitivity, flexibility, transparency, and durability. They can be used individually or in combination to create multifunctional and high-performance tactile sensors.

2.3.2.3. Electrode Materials

Electrode materials are crucial components of tactile sensors, as they facilitate the detection and measurement of electrical signals generated in response to mechanical stimuli. The choice of electrode material directly influences the sensor's sensitivity, flexibility, conductivity, and overall performance. Some of the common electrode materials are metals (gold, silver, copper, etc.)[5, 65, 134, 135], conductive polymers (PEDOT, Polyaniline)[136, 137], transparent conductive oxides (Indium Tin oxide (ITO))[14, 138], printed conductive inks (silver ink, graphene conductive ink)[63, 139, 140] etc.

2.3.3. Fabrication methodology

There are various methods for fabricating tactile sensors and these methods are tailored to meet specific application requirements, such as flexibility, sensitivity, durability, and cost-effectiveness. These methods can be broadly categorized into the following key approaches:

- **Material Compositing:** This is one of the widely used method that involves the integration of various functional materials into a single composite structure that exhibits the desired sensing properties.

  - **Blending and Doping**: Functional materials like conductive fillers (e.g., carbon black, graphene, metal nanoparticles) are mixed into a soft polymer or elastomer matrix[71].
  - **Encapsulation:** In this technique, the active sensing material is sandwiched between protective layers of flexible substrates. This enhances the durability and sensitivity of the sensor, making it suitable for various tactile applications[95].

- **Drop Casting:** Drop casting involves depositing a liquid solution of functional material onto a substrate and allowing it to dry, forming a solid film. This method is simple and cost-effective, often used to create thin-film sensors consisting of active materials like ZnO NWs, CNT, graphene etc. with relatively uniform thickness[141-143].

➢ **Pattern Transferring:** These methods are employed to develop precise geometries and microstructures in the sensor, which are crucial for enhancing its performance.

- **Photolithography:** Photolithography is a common technique used to transfer a pattern onto a photosensitive material. This method involves coating a substrate with a photosensitive layer, exposing it to light through a mask, and then developing the exposed areas to create the desired pattern. It's widely used for creating fine features and microstructures in tactile sensors[101, 144].
- **Screen Printing**: Screen printing involves using a mask or stencil to apply a functional ink or paste onto a substrate. This method is cost-effective and scalable, making it ideal for producing large-area tactile sensors. The technique is especially useful for creating patterns of conductive traces or sensing elements on flexible substrates[63, 139, 140].
- **Inkjet Printing**: Inkjet printing is a precise method for depositing materials layer by layer to create thin-film sensors. This technique allows for high-resolution patterning and is suitable for producing sensors with complex geometries[145-147].
- **3D Printing:** 3D printing enables the fabrication of tactile sensors with complex three-dimensional structures. This technique is particularly useful for creating

sensors with integrated features or custom shapes that conform to specific surfaces[72, 148-151].

- **E-beam Lithography**: E-beam lithography is an advanced patterning technique that uses a focused beam of electrons to draw custom patterns on a substrate coated with an electron-sensitive resist. It offers extremely high resolution, making it ideal for fabricating nanoscale features in tactile sensors[152, 153].

➢ **Microfabrication Techniques:** These methods are essential for creating tactile sensors with high sensitivity and small form factors.

- **Micromolding:** Micromolding involves creating a mold with the desired microstructure and then filling it with a sensor material. Once the material solidifies, it is released from the mold to form a tactile sensor with precise micro-scale features[86, 154].
- **Laser Cutting and Engraving**: Laser cutting and engraving are used to create intricate patterns and microstructures on sensor substrates. These techniques are highly precise and can be used to fabricate stretchable sensors with complex designs like serpentine or kirigami patterns[155, 156].

➢ **Coating Techniques:** This involves sequentially depositing different materials to build up the sensor structure. This method is particularly useful for creating multilayered sensors with distinct functional layers.

- **Spin Coating:** It is used to apply uniform thin films of materials onto a substrate. Multiple layers can be sequentially coated to create a multilayer sensor structure[157, 158].

- **Spray Coating:** Spray coating involves atomizing a solution of functional material and spraying it onto a substrate, forming a thin, uniform layer. This method is scalable and can be used to coat large or irregularly shaped surfaces[80, 159, 160].

- **Chemical Vapor Deposition (CVD):** CVD is a process where vapor-phase chemicals are used to deposit thin films of material onto a substrate. This method is commonly used to create high-quality, uniform films of materials like graphene or carbon nanotubes, which are often used in tactile sensors for their excellent electrical properties[118, 119].
- **Electrodeposition:** Electrodeposition or electrospinning involves depositing a material onto a substrate by applying an electric current through an electrolyte solution containing the desired material. This technique is commonly used for creating metal or conductive polymer layers like PEDOT or PANI on flexible substrates, enhancing the electrical properties of tactile sensors[116, 124, 125, 136].
- **Transfer Printing:** Transfer printing is a technique used to transfer pre-fabricated microstructures or thin films from one substrate to another. This method is particularly useful for creating flexible sensors by transferring rigid, high-performance materials onto a flexible substrate[72, 161].

Tables 1 and 2 below provide detailed information on the materials and fabrication methods used, along with their corresponding sensitivity and gauge factors, for various pressure and strain sensors reported in the literature.

Table 2.2: Some pressure sensors from literature with their active material, substrate, fabrication method, sensing mechanism and sensitivity

Active material	Substrate	Fabrication method	Sensing mechanism	Sensitivity/Pressure Range	References
MXene Film	Polyimide	Inkjet printing, Drop casting	Piezo-resistive	180 kPa^{-1}(~40 kPa)	[162]
Polyimide/Graphene foam	Acrylic bar	Freeze drying, thermal annealing	Tribo-electric	0.52 N^{-1}(~30 N)	[163]
Micro-structured graphene	PDMS	Spray Coating, assembling	Piezo-resistive	1.2 kPa^{-1}(~30 kPa)	[164]
$CaCu_3Ti_4O_{12}$ - PDMS	PDMS	Electro-spinning	Piezo-capacitive	1.66 kPa^{-1}(~ 0.64 kPa)	[165]
PVA/H_3PO_4	Polyimide	E-beam evaporation, spin coating	Piezo-capacitive	200 kPa^{-1}(~320 kPa)	[166]
rGO	PET	Drop casting	Piezo-resistive	178.5 kPa^{-1}(~42 Pa)	[167]
Nested wrinkling PPy	PDMS	Chemical oxidation polymerization	Piezo-resistive	19.32 kPa^{-1}(~2.036 kPa)	[168]
Graphite paste	PDMS	3D Printing	Resistive	0.346 kPa^{-1}	[169]
Silver Paste	PDMS	3D Printing	Capacitive	0.25 kPa^{-1}	[170]

Table 2.3: Some strain sensors from literature with their active material, substrate, fabrication method, sensing mechanism and sensitivity

Active material	Substrate	Fabrication method	Sensing mechanism	Gauge factor/ Max. Strain	References
CNT Fiber	Ecoflex	Dry CVD	Piezo-resistive	48(ε~400%–700%)	[171]
Ag NWs	PDMS	Drop casting and Peeling	Piezo-resistive	14(ε~70%)	[172]
ZnO NW array	PET	Hydrothermal	Piezo-electric	1813	[173]
CNT ink	PU Yarn	Swelling and Sonication	Piezo-resistive	1344.1(~200%)	[174]
CNT/PDMS composite	PDMS	Spray deposition and Printing	Piezo-resistive	35(~45%)	[175]
Graphene nanosheets/Au film/ Graphene nanosheets	PU Yarn	Layer by layer assembly and sputtering	Piezo-resistive	661.59(~50%)	[176]
Ag@CNTs	PDMS	Microfluidics	Resistive	172	[177]

2.4. Current challenges in developing tactile sensors

Developing tactile sensors require careful design and fabrication considerations. The most basic requirements for a tactile sensor are high sensitivity/gauge factor, low hysteresis, lower cost and easy fabrication and good reliability and shelf life[4, 72, 178]. Among these, the most crucial requirement is attaining high sensitivity (or gauge factor for a strain sensor) without using sophisticated fabrication techniques. Tactile sensors need to detect a wide range of stimuli, from very light touches to strong pressures. Achieving this sensitivity across such a broad range while maintaining accuracy is a significant challenge[21, 23]. The sensitivity of these sensors is highly dependent on materials selection as well as their composition in making these sensors. Most existing research has focused primarily on reporting physical tactile sensors based on specific performance metrics (such as sensitivity, gauge factor or flexibility) without thoroughly exploring how modifications in the active materials selection and their composition can affect the sensor's response[21, 67].

Additionally, due to use of various fabrication techniques and processes, some defects or contaminants are intrinsically found in these sensors[16, 75, 120]. These defects or contaminants can either enhance (like creation of microcracks in strain sensors[120]) or impair (like presence of water molecules on graphene surfaces in graphene-based field-effect transistor or sensors[179, 180]) the sensitivity of the sensor. However, the nature of these defects and their effect on the sensor performance has not been studied extensively in literature.

Modelling and simulation are also essential tools in developing tactile sensors as they enable researchers to predict and optimize sensor performance before physical prototypes are made. These techniques assist in selecting appropriate materials by predicting their performance under various mechanical stimuli, ensuring the chosen materials offer the

best balance of sensitivity and durability[181, 182]. They also allow for the optimization of sensor designs, helping to refine geometries and configurations to meet specific performance requirements such as high sensitivity or accurate response characteristics[181, 183, 184]. These computational techniques also reduce the need for extensive physical prototyping, saving both time and resources. Additionally, simulations provide insights into the long-term performance of sensors, helping to anticipate potential issues related to durability and stability before manufacturing. Effect of nanoscale or microscale defects can also be studied theoretically using these techniques.

2.5. From Sensors to Artificial Sensing System

Artificial tactile sensation systems advance the capabilities of tactile sensors by incorporating them into more sophisticated systems that not only detect but also interpret and respond to tactile stimuli, closely mimicking the human sense of touch. These systems integrate various components, including sensors, signal processing units, and feedback mechanisms, to create a comprehensive perception of touch[49, 185, 186]. These systems enable to detect high frequency vibrations as well as high pressure loads with same sensing systems[100, 187]. Furthermore, these systems could contribute to the development of smart gloves and prosthetics that are both integrable with human anatomy and biocompatible[6].

As discussed earlier in Section 2.1, the human tactile perception system consists of slowly adapting (SA) and fast adapting (FA) mechanoreceptors, which together perceive both static and dynamic stimuli. The human nervous system then analyzes signals from these receptors to produce a coherent tactile perception[31]. To replicate this functionality in artificial systems, it is necessary to couple and integrate different types of sensors that can simultaneously achieve both static and dynamic sensing. While much of the current research in tactile sensors has focused on developing systems that target either static or

dynamic sensing, as previously illustrated in Tables, there are relatively few studies that successfully combine both types of sensors. In this regard, Chun *et al*[30] developed a self-powered mechanoreceptor sensor based on an artificial ion-channel system combined with a piezoelectric film, which can simultaneously implement FA and SA pulses like human skin. This device detects stimuli with high sensitivity and broad frequency band without external power. Later, an artificial neural tactile system was developed by coupling a piezoresistive sensor with a piezoelectric sensor[188]. Similarly, in another work, a piezoresistive sensor array (mimicking SA) based on graphene based sensors was coupled with a TENG device (mimicking RA) to develop an artificial pressure sensing system (shown in Figure 2.12)[187].

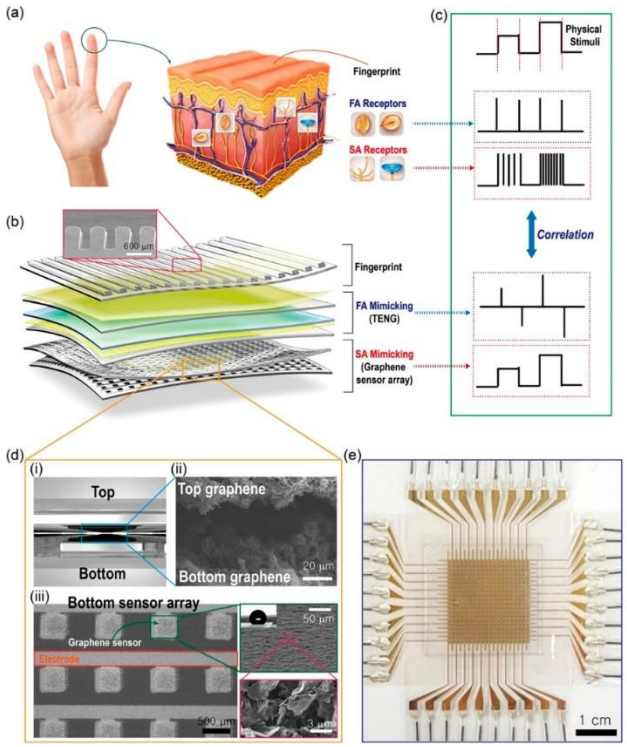

Figure 2.12 Flexible electronic mechanoreceptors mimicking human finger skin. (a)Schematic of finger skin and fingerprint structure consisting of SA and FA receptors. (b) Schematic illustration of the tactile sensor. This tactile device is composed of a bottom panel with a SA-mimicking sensor, a top panel with an FA-mimicking sensor, and an artificial fingerprint structure with microlines. (c) Correlation between neural spikes of human skin and electrical output signals of an NTS device for slow and fast adaptation in response to physical stimuli, respectively. (d) Interlocked percolative graphene sensor array. (d(i)) Schematic of individual interlocked top and bottom GNP films. (d(ii)) SEM image showing graphene morphology of the interlocked region. With natural force, top and bottom graphene films are slightly interlocking with distance. (d(iii)) Optical image of the bottom graphene film array and top-view GNP film. (e) Photograph of completed SA-mimicking sensor array as bottom panel[187] (Copyright © 2019, American Chemical Society).

Additionally, it's necessary to transform the data generated by e-skin sensors into neural spikes form. This translation is important because it allows the system to mimic the way the human nervous system processes sensory information, where signals from various parts of the body are rapidly and efficiently processed to form a cohesive understanding of touch, pressure, and other tactile sensations[3, 24]. By converting sensor data into neural spikes, the system can manage and analyze inputs from a wide array of sensors more efficiently, much like how our brains handle sensory data[3]. This approach not only improves the system's efficiency but also makes it easier to integrate artificial intelligence models that can interpret and learn from the neural spike data[189]. For example, these AI models can be trained to recognize different textures[190], detect gestures[191], or perform other complex tasks by analyzing patterns[188] in the neural spikes.

This fusion of tactile sensing and neuromorphic processing represents a significant step towards creating more advanced, responsive, and intelligent tactile systems. By harnessing the power of neural spike data, these systems can perform complex sensory tasks more efficiently and effectively, paving the way for innovations in areas like robotics, prosthetics, and human-machine interfaces.

2.6. Summary

This chapter explores the current understanding of human tactile perception and its application in developing flexible e-skin sensors. Initially, the principles behind the human sense of touch were explained, followed by an introduction to e-skin technology and its related sensors, highlighting how these devices can mimic the tactile sensing mechanisms of human skin. This chapter then delves into the various design strategies and materials used in creating flexible tactile sensors, with a focus on pressure and strain sensors. The current challenges in developing these sensors as well as method to develop artificial sensing systems from e-skin sensors have also been discussed.

Based on the principles of human tactile sensing and methods of fabricating e-skin sensors, this thesis aims to address the discussed challenges in the field of e-skin sensors. The main focus of the remaining thesis will be on developing artificial sensors and associated systems that biomimics the human tactile sensation. Studies on modelling and simulation to design and optimise pressure sensors as well as theoretical understanding of defects in these sensors has also been discussed. In Chapter 3, I will begin by discussing the fabrication of flexible strain sensors using Ecoflex and carbon-based nanomaterials. This chapter will also cover how the chemical composition influences the gauge factor of these sensors and explore the development of an artificial strain sensing system incorporating these sensors. Chapter 4 introduces a hybrid flexible sensor system composed of a capacitive pressure sensor (CPS), which mimics SA mechanoreceptors, stacked over a triboelectric nanogenerator (TENG), which mimics RA mechanoreceptors. Chapter 5 will focus on modelling and simulation of PDMS and ZnO NWs based pressure sensor to design and optimise their performance. Later, in chapter 6, I will discuss about a simulation study on investigation of the structural variations of the trapped water molecules present in GFETs based pressure sensors.

Chapter 3

Development of Soft Stretchable Strain Sensors for Neuromorphic Sensing Applications

The work is based on following publications:

Journal Articles:

- Kumaresan, Y*., **Mishra, S.*,** Ozioko, O., Chirila, R., Dahiya, R., Ultra-High Gauge Factor Strain Sensor with Wide-Range Stretchability, *Advanced Intelligent Systems*, 4 (9), 2200043 (2022) (*equal contribution)

Conference Papers:

- **Mishra, S.,** John, D., Kumar, N., Rai, B., Georgiev, V., "Human-Inspired Stretch and Joint-Bend Sensing System Based on Flexible Sensors" presented in *2023 IEEE Sensors Conference,* Vienna, Austria

Abstract

The development of stretchable strain sensors for detecting human motion necessitates a combination of wide-range stretchability, high sensitivity (indicated by a high gauge factor), and reliability. This chapter introduces a high-performance stretchable strain sensor with a tunable gauge factor and multi-strain range, achieved by incorporating carbon-based fillers and graphene-carbon paste (GCP) into an elastomer matrix.

A systematic investigation of various combinations of elastomer, conductive filler, and GCP revealed that excellent stretchability is attained when filler particles are dispersed

within the elastomer, owing to its inherent mechanical properties. In contrast, high sensitivity is achieved when filler particles are combined with GCP, due to the formation of multiple cracks and fragmentation of the paste under small strains. The integration of GCP with the elastomer-filler composite synergistically enhances the sensor's performance, providing both wide-range stretchability and high sensitivity. The elastomer-filler composite facilitates a percolation path that bridges the paste fragments under large strains.

Specifically, a strain sensor with a 50 wt.% GCP loading demonstrated 500% stretchability with a gauge factor of 504. Increasing the GCP loading to 150 wt.% resulted in 45% stretchability with an unprecedented gauge factor of 1,834,140. These sensors are capable of detecting both small- and large-scale strains, making them suitable for monitoring facial expressions and joint movements.

Additionally, bio-mimicking of human tactile sensing systems using flexible and reliable sensors and electrical circuits has become increasingly important for the development of advanced robots and prosthetics with enhanced sensory capabilities. This chapter also describes the development of an artificial tactile system that includes proprioception functionalities. This system employs strain sensor developed in this work, integrated with a Wheatstone bridge and a simulated leaky-integrate-and-fire (LIF) neuron. Under strain condition, this system generated neural spike trains, with firing rates varying from 7 to 26 spikes per minute as the strain levels increased from 5% to 50%. This spiking behavior mimics an afferent neuron connected to a slowly-adapting mechanoreceptor. The relationship between firing rate and different stretch and bending angles in the sensor was also examined to develop an artificial proprioception system.

3.1. Introduction

As described in previous chapter, there is a growing demand for real-time monitoring of mechanical deformations like bending, rotation and strain associated with the activities of humans, robots, and machines[4, 11, 20, 46, 48]. This demand is driven by applications in wearable electronics, health monitoring, human-machine interfaces, and robotics[192, 193]. Consequently, various types of strain sensors have been developed using different materials, gauge factors, stretchability, and transduction mechanisms, including piezoresistive, capacitive, inductive, and optical methods[48, 54, 60, 76, 107, 194-197]. These sensors convert mechanical strain into measurable physical parameters such as electrical resistance, capacitance, inductance, and optical wavelengths[106]. Among these, piezoresistive strain sensors are particularly popular due to their high sensitivity, ease of fabrication, diverse material choices, designs, and potential for use in various environments and applications[67, 198].

As mentioned in Chapter 2, stretchable piezoresistive strain sensors typically consist of a film of active material, which provides a conductive network, and a stretchable polymeric substrate, such as Ecoflex or polydimethylsiloxane (PDMS), for stretchability. Composites made of electrically conductive nanomaterials and elastomers are commonly used as core materials for these sensors[19, 73, 108, 199]. Popular conductive fillers include graphene[122], carbon nanotubes (CNT)[77], silver nanowires[200], zinc oxide[59], carbon black[79], and graphite[201]. Carbon-based materials are especially favored due to their abundant availability, cost-effectiveness, tunable electrical properties, large operational window, dispersibility in various solvents, supportive matrix, and suitable mechanical features.

In piezoresistive strain sensors, applying strain causes geometrical deformation in the active material region, resulting in a corresponding change in electrical resistance. The sensitivity of a strain sensor is defined by its gauge factor (GF), which is the ratio of the percentage change in sensor response to the applied strain. Strain sensors with remarkable stretchability, reaching hundreds of times their original size, and sensitivity varying from low (under 10) to high (around 1000) have been developed for various applications[21, 75, 106, 194, 202, 203]. Additionally, the material type, morphology of the active region, and interaction of filler particles in that region are critical to the strain sensor's response. However, most studies have focused on strain sensors with specific figures of merit (e.g., gauge factor or stretchability) without systematically investigating how modifying the active materials (the conducting composite) affects the sensor's overall performance.

As discussed in Chapter 2, human tactile system consists of receptors and nerve fibers in the skin that perceive and transduce external stimuli like touch, pressure, and vibration into nerve signals sent to the brain (shown in Figure 3.1(a))[4, 193]. These low-threshold mechanoreceptors (LTMRs), including slowly-adapting (SA) and rapidly-adapting (RA) types, generate spiking signals in response to stimuli[31]. Additionally, the proprioceptive system detects location and enables precise movement for tasks like grasping objects[204]. Inspired by these mechanisms, recent works in artificial tactile perception systems use electronic devices to encode stimuli into action potentials, leading to efficient and accurate robotic and prosthetic sensory capabilities[3, 24]. These systems include flexible, sensitive sensors and circuits that convert data into neural signals, aiming to fully mimic LTMR and proprioceptive functions[190].

In this chapter, a neuromorphic artificial strain and joint-angle sensing system (as depicted in Figure 3.1(b)) is presented that generates neural spikes to achieve skin-like

sensing and proprioception. Initially, I will discuss development of a universal strain sensor by combining various conducting fillers within an elastomer matrix to achieve a tunable sensor response with wide-ranging stretchability. Three combinations of piezoresistive sensing materials by mixing elastomer, conductive filler, and graphene carbon paste (GCP) was investigated. Due to the elastomer's excellent mechanical properties, the elastomer-filler combination demonstrated excellent stretchability with moderate response. Conversely, the sensor with the paste-filler combination exhibited excellent sensor response but poor stretchability due to paste fragmentation. By introducing the paste into the elastomer-filler combination, we achieved an outstanding sensor response with tunable stretchability, as the elastomer-filler provided a percolation path to bridge paste fragments under large strain. The sensor exhibited tunable stretchability ranging from 0% to 625% strain, with the gauge factor varying from 0.8 to 1,834,140.

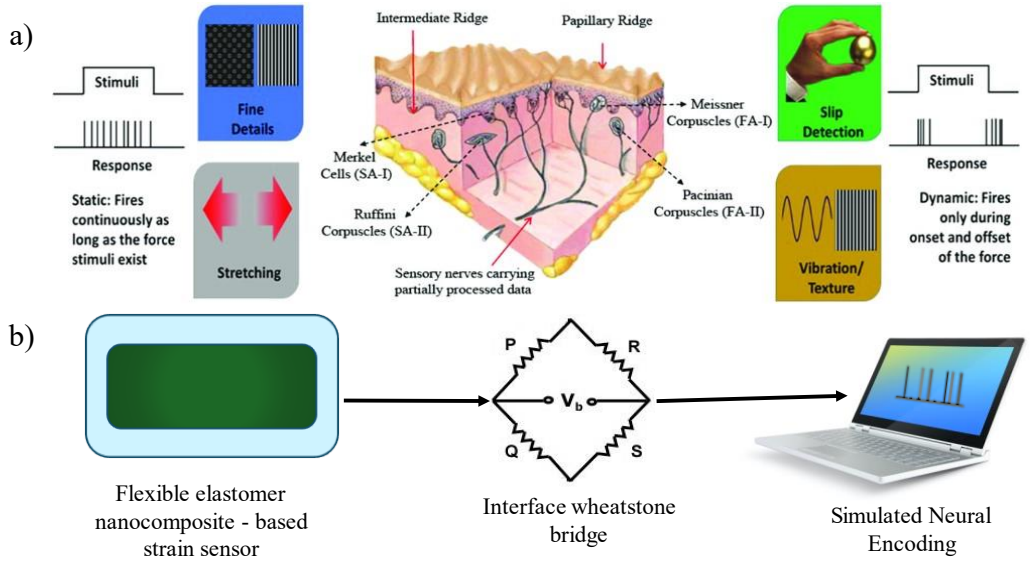

Figure 3.1: (a) Schematic representation of skin LTMRs, their functions, and spiking behavior, adapted from Navraj et al. [1] under a CC-BY 4.0 license. (b) Schematic illustration of the neuromorphic strain detection system developed in this study.

After discussing about the piezoresistive strain sensor development and performance, it's application in creating a neuromorphic artificial strain and joint-angle sensing system has also been shown. This sensor was connected to a wheatstone bridge to produce output voltage signals, which were then fed into a simulated leaky-integrate-and-fire (LIF) neuron model to encode the sensor data into spiking pulses. This neuromorphic system emulates the functionality of a SA-LTMR, a muscle spindle, or joints such as fingers, knees, and elbows in the human body. Such systems could advance the development of robots and prosthetics with enhanced somatosensory and proprioceptive capabilities.

3.2. Methodology

3.2.1. Sensor Fabrication and characterisation

Three combinations of piezoresistive sensing materials—elastomer-filler, paste-filler, and elastomer-paste-filler—were synthesized using ecoflex as the elastomer, GCP as the paste, and carbon nanotubes (CNT) and/or graphite as the filler.

Figure 3.2(a) illustrates the synthesis of the elastomer-filler composite-based piezoresistive material. First, the filler particles, either CNT or graphite, were separately added to Part A and Part B of the ecoflex at the desired weight percentage and manually stirred for 5 minutes to achieve uniform dispersion. Subsequently, Part A and Part B were combined and mixed for another 5 minutes, and the resulting mixture was immediately used to fabricate the elastomer-filler composite-based piezoresistive strain sensor, as shown in Figure 3.2(c).

A similar process was followed to synthesize the elastomer-paste-filler composite-based piezoresistive material. In this case, GCP was added and mixed with the filler before combining Part A and Part B (Figure 3.2(b)). For the paste-filler composite-based

piezoresistive material, the filler particles were directly added to the paste, manually mixed for 5 minutes, and then used for sensor fabrication.

Figure 3.2(c) illustrates the fabrication schematic of the piezoresistive strain sensor using the aforementioned sensing materials. The strain sensor consists of three layers: the bottom substrate, the sensing layer, and the encapsulation layer. First, a master mold with dimensions of 3.5 cm x 0.5 cm x 175 µm (length, width, height) was fabricated on PVC using a blade cutter tool. Ecoflex was then poured into the mold, cured, and separated from it to create a substrate with a 175 µm thick pit containing the inverse pattern of the mold. The piezoresistive sensing material was uniformly coated inside the pit using the doctor blade technique. After curing the sensing material, Ecoflex was used to encapsulate the sensing channel.

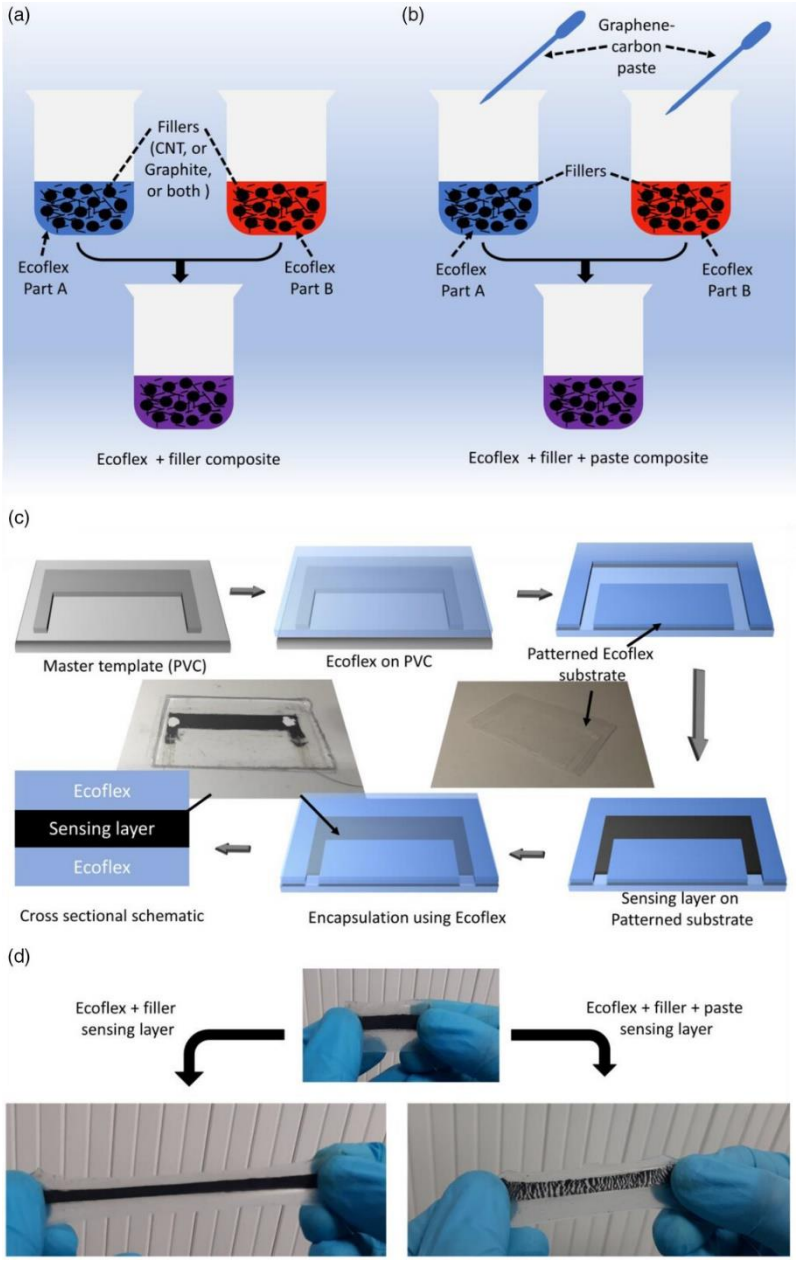

Figure 3.2: Schematic overview of the synthesis and fabrication process for stretchable strain sensors: a–b) Preparation of strain-sensing materials, specifically Ecoflex + filler composites: a) without graphene–carbon paste (GCP), and b) with GCP; c) Fabrication steps, including creating the master template, casting Ecoflex, removing the patterned Ecoflex substrate, applying the sensing layer using the doctor blade method, and encapsulating with Ecoflex. The inset shows a photographic image of the patterned Ecoflex substrate and the final stretchable strain sensor. d) Photographic image of the sensors, with and without GCP, under stretching conditions.

Device characterization was performed by clamping the sensor in a homemade stretching system consisting of two linear stage motors (VT-21 from Micronic USA) connected to LabVIEW software-driven Pollux Box, enabling precise control of stage movement. A digital multimeter (KEYSIGHT, 3446X) was used to record the resistance change.

Scanning electron microscopy (SEM) images were obtained using an FEI Nova NanoSEM. A Wheatstone bridge was also developed to transform the resistance change of the strain sensor to corresponding voltage value which was then fed to the neural spike generation program.

3.2.2. Neural Encoding Model

The LIF model is a simplified representation of the electrical activity of neurons. This model was employed to simulate an artificial neuron and convert the output voltage from the Wheatstone bridge circuit into neural spikes. In the LIF model, a parallel resistive-capacitive circuit represents a neuron. The capacitor stores the voltage, and the resistor controls the leakiness. Our model comprises two components: firstly, a linear differential equation[31]

$$\frac{dV_{mem}}{dt} = \frac{I_{sensor}}{C} - \frac{V_{mem}}{\tau_{mem}} \tag{3.1}$$

which represents the evolution of membrane voltage inside neuron V_{mem}.

In this equation, I_{sensor} is the output current from the sensor, which equals $G * V_{sensor}$. Here, V_{sensor} is the sensor's output voltage from the Wheatstone bridge, and G is a transconductance constant valued at 1 pS. τ_{mem} denotes the membrane time constant, defined as RC, where R and C are the membrane's leak resistance and capacitance, respectively. This time constant represents the duration the neuron takes to decay to its equilibrium voltage (V_{equi}) when no input current is present.

Secondly, a LIF neuron includes a threshold for neuron firing, where it generates a spike when $V_{mem} > V_{thr}$. Here, V_{thr} represents the threshold voltage, and once a spike is generated, V_{mem} is set to V_{equi}. The LIF neuron model is selected for its computational

simplicity and ability to mimic key features of biological neurons. In our implementation, based on our sensor's data, we set V_{equi} to 0V and V_{thr} to 0.2V. The membrane time constant τ_{mem} in our model was chosen as 20 seconds. Data from the Wheatstone bridge was acquired at a rate of 2.5 Hz, and the neuron model was coded in Python. Spiking rates were calculated at different strain levels when the sensor underwent uniaxial stretching and bending.

3.2.3. Molecular Dynamics Simulation Methodology

Molecular dynamics (MD) simulations were performed on the sensor materials to understand their behaviour under stretching conditions. Towards this, two systems were created using PDMS molecules as the elastomer. In the first system, 100 PDMS chains, each with 15 monomers, were placed in a box, along with two graphene sheets (5 nm × 5 nm, chirality (3,3)) and two single-walled carbon nanotubes (SWCNTs) (4.92 nm in length, 0.41 nm diameter, chirality (3,3)), maintaining a weight ratio of 1:0.2:0.015. In the second system, four additional graphene sheets and 60 C_{60} fullerene particles were introduced to simulate the spherical carbon particles in the GCP used in the experiments, keeping the weight ratio consistent.

Both systems underwent initial energy minimization followed by equilibration in the NPT ensemble at 0 atm and 300 K for 1 ns with a timestep of 1 fs. Next, a simulated annealing process raised the temperature from 300 K to 600 K over 1 ns, with relaxation at 600 K for another 1 ns. Afterward, the systems were cooled back to 300 K over 1 ns and equilibrated at 300 K for 5 ns. Once equilibrated, a tensile test was applied in the x-direction, maintaining zero pressure in the other two directions, using a strain rate of 10^{10} s^{-1}. All simulations were conducted in LAMMPS[205] using OPLSAA[206] forcefield parameters.

3.3. Results and Discussion

3.3.1. Sensing material characterisation

Three different composite materials (elastomer–filler, GCP–filler, and elastomer–GCP–filler) comprising different piezoresistive sensing layers were created using various combinations of carbon filler materials (CNT and/or graphite), Ecoflex, and GCP. In the elastomer–filler composite, a conductive path is formed through the continuous network of filler particles within the insulating elastomer matrix. There are two critical factors influencing the formation of this conduction path i.e., proper dispersion of filler within the elastomer matrix and the loading weight percentage (wt%) of filler particles. For instance, agglomeration of filler particles can lead to uneven distribution, resulting in highly conductive networks at agglomerated sites and insulating regions elsewhere. Observing the structural morphology using a scanning electron microscope (SEM) is a straightforward method to assess the distribution of filler particles in the elastomer matrix. Figure 3.3 depicts SEM images of CNT, graphite and Ecoflex–graphite–CNT composite based sensors. Generally, filler particles tend to agglomerate due to van der Waals forces (Figure 3.3(a-b)). To achieve uniform distribution, CNTs of appropriate weight percent (wt%) were added to Ecoflex Part A and continuously mixed/sonicated for 5 minutes. Similarly, graphite microparticles were added to Ecoflex Part B and sonicated. Finally, both Part A and Part B were mixed together to obtain the elastomer–filler composite. The SEM images show that the fillers, such as CNTs and graphite particles, are uniformly distributed throughout the insulating matrix (Figure 3.3(c-d)).

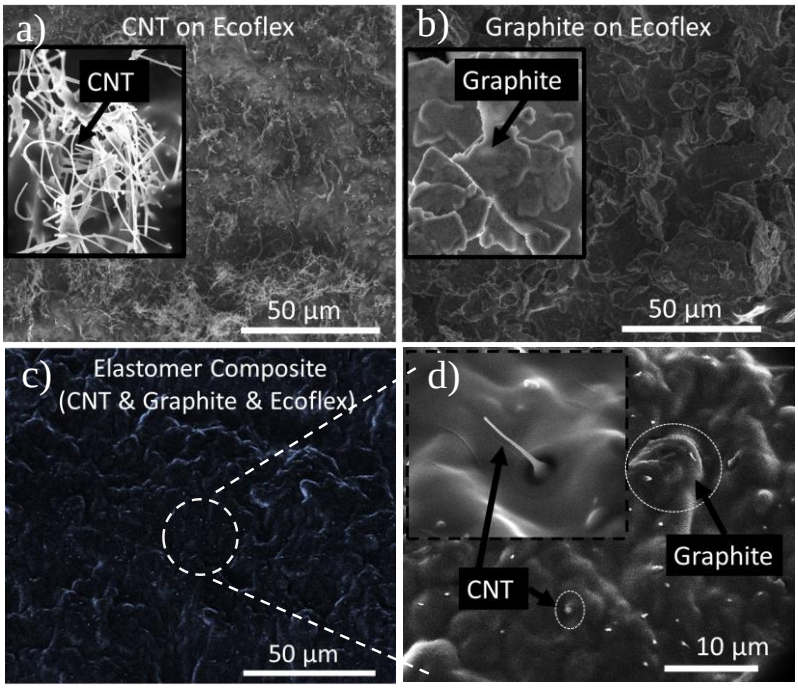

Figure 3.3: Scanning electron microscope (SEM) image of sensing material: a) CNT on Ecoflex, b) graphite particles on Ecoflex, and c) elastomer filler made of Ecoflex–CNT–graphite. d) zoomed image of Ecoflex–CNT–graphite

Further, X-ray diffraction (XRD) analysis was conducted to assess the filler loading within the elastomer, as shown in Figure 3.4. The presence of two peaks at $2\theta = 28°$ (002) and $2\theta = 44°$ (100) in the XRD pattern indicates strong carbon diffraction from the filler particles (graphite, CNT, and GCP). This confirms that the filler particles are successfully embedded within the Ecoflex matrix[120, 207].

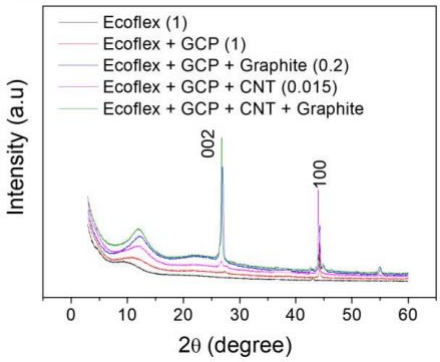

Figure 3.4: X-ray diffraction (XRD) graphs of pure Ecoflex with different sensing materials loading.

To understand the network formation of the elastomer–filler composition, samples (3.5 cm × 0.5 cm × 0.1 mm) with varying filler loading percentages were evaluated. The resistance values of these samples, measured with a digital multimeter across the two extreme corners, are listed in Figure 3.5(a). The specific filler loading at which a conductive network forms within the elastomer matrix is known as the percolation threshold. At this threshold, the filler particles may not be in direct contact, and electrons are primarily transported through tunneling. Generally, the maximum tunneling distance for continuous electron transport is reported to be less than 5 nm[208]. With a small amount of filler particles, there are very few conductive paths available, resulting in high resistance values ranging from tens of kΩ to MΩ.

As shown in Figure 3.5(b), a graphite loading ratio of either 10:1.5 or 20:0 resulted in a high resistance value of 40 kΩ. Additionally, working close to the percolation threshold can cause signal fluctuation, as small strains can disrupt the conductive network and significantly affect resistance. When the loading is below the percolation threshold, filler particles do not form a continuous conduction path, resulting in no electron flow and making the composite insulating. Accordingly, only graphite (up to 10 wt%) or only CNT (up to 2 wt%) exhibited insulating behavior (Figure 3.5(b)). In contrast, with higher loading, i.e., above the percolation threshold, filler particles come into direct contact, forming a connected network that creates a highly conductive (low resistance) path. Consequently, loading both graphite (>10 wt%) and CNT (>1.5 wt%) above their percolation threshold resulted in a well-connected conductive network with resistance values ranging from 200 Ω to 6 kΩ (Table 3.1).Further increasing the filler loading, especially beyond 20 wt% graphite or 3 wt% CNT, or a combination of >10 wt% graphite and >2 wt% CNT, made it challenging to achieve uniform distribution or cure the elastomer–filler composite.

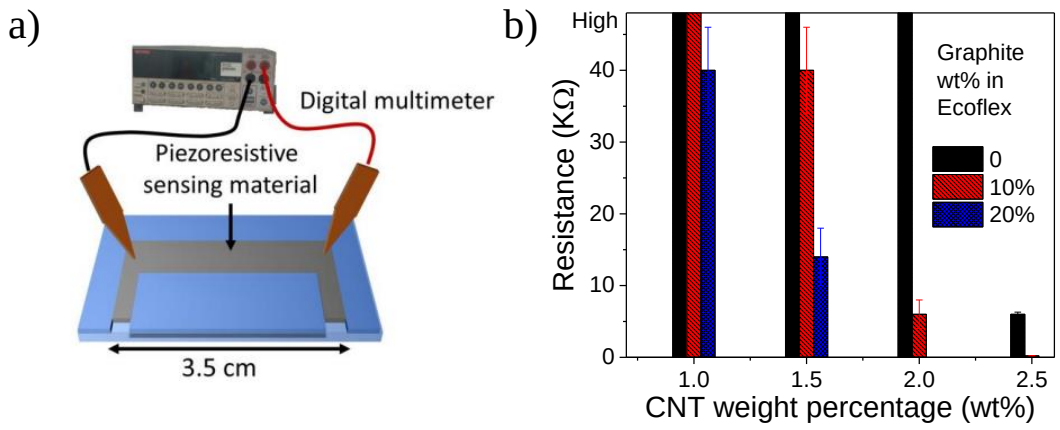

Figure 3.5: (a) Schematic illustration of base resistance measurement prior to stretching (b) resistance values at various loadings of CNT and graphite in Ecoflex

Table 3.1: Resistance value of various combinations in wt% of sensing materials

Ecoflex	Graphite	CNT	Resistance
100	0	(0-2)	Insulating
100	0	2.5	6kΩ
100	10	1	Insulating
100	10	1.5	40kΩ
100	10	2	6kΩ
100	10	2.5	0.2kΩ
100	20	0	Insulating
100	20	1	40kΩ
100	20	1.5	14kΩ

Based on these observations, we fabricated elastomer–filler composites with two different mixing ratios of elastomer: graphite: CNT: 10:1:3 (named Sample 1) and 10:2:1.5 (Sample 2). Typically, strain sensors with excellent stretchability and high gauge factors are achieved by generating intentional or unintentional microcracks[209]. Also, few analytical models predict that voltage distribution in crack-based strain sensors drops much faster than in flat sensors, leading to a greater resistance change during stretching[66, 180]. Therefore, an equal amount of GCP was added to Sample 2, with a mixing ratio of 1:1 (Sample 2) and its SEM image is shown in Figure 3.6. It is evident

that the surface of the GCP composite exhibited numerous cracks and boundaries. For a better understanding, the flow of various sample combinations used in this study is described in Figure 3.7.

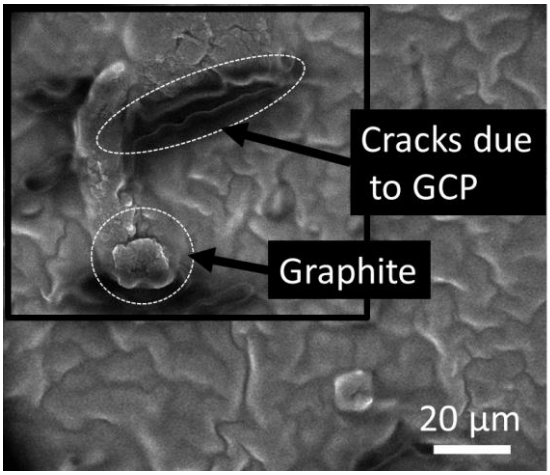

Figure 3.6: SEM image of Graphite+CNT+GCP+Ecoflex based sensing material

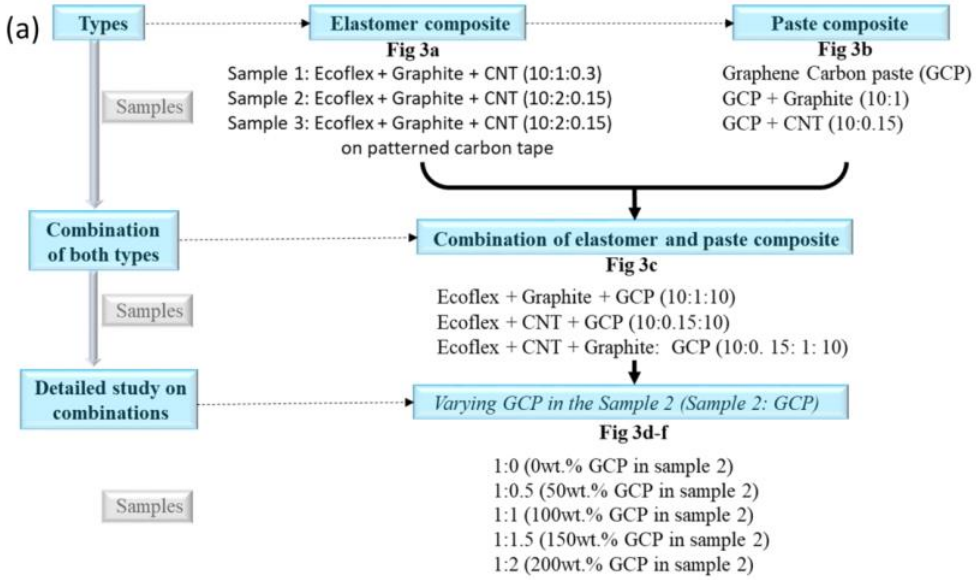

Figure 3.7: a) Flowchart illustration of different types of sensing materials.

3.3.2. Strain Sensor Performance

The electrical properties of different combinations of sensing channels, including elastomer–filler, GCP–filler, and elastomer–GCP–filler, are shown in Figure 3.8. The sensor response was evaluated by measuring resistance changes under strains ranging from 0 to 625%. As shown in Figure 3.8(a), Sample 1 and Sample 2 demonstrated high stretchability (up to 625%), with gauge factors varying between 0.3 and 10.8 at different strain levels. Notably, Sample 2 exhibited the higher gauge factor for strains below 200%, while both Sample 1 and 2 maintained excellent stretchability.

Additionally, as mentioned previously, three types of GCP-filler composites were fabricated: GCP only, GCP with graphite, and GCP with CNT. The pure GCP sample was not stretchable, showing no electron flow beyond 1% strain (Figure 3.8(b)). However, adding filler particles to the GCP paste enabled electron flow up to 20% strain. Among these, the CNT-filled sample displayed much greater stretchability (up to 20%) and a gauge factor of around 11,340, outperforming the graphite-filled composite.

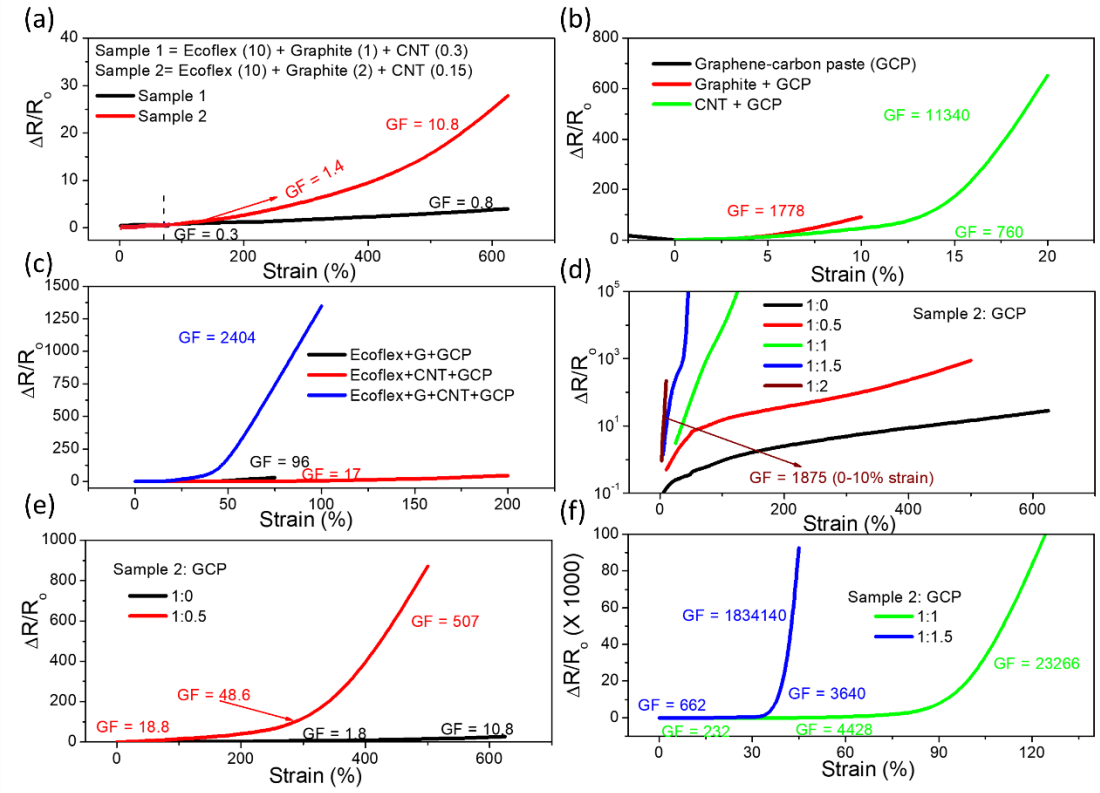

Figure 3.8: Comparison of strain sensor performance with various sensing channel combinations, including elastomer–filler, paste–filler, and elastomer–paste–filler composites. The relative change in resistance under different strain levels is shown for: a) elastomer–filler composite, b) GCP–filler composite, and c) elastomer–GCP–filler composite. d–f) Performance comparison of sensors with varying GCP (paste) loading in Sample 2: d) Logarithmic plot for all combinations; e) Linear plot focusing on the 1:0 and 1:0.5 Sample 2 ratios; f) Linear plot focusing on the 1:1 and 1:1.5 Sample 2 ratios.

While elastomer-filler composites demonstrated high stretchability, they were limited in their sensor response and gauge factor. Conversely, paste-filler composites showed low stretchability but excellent sensitivity. Thus, the combination of elastomer and filler materials aims to achieve both stretchability and high sensor response. Hence, three sensor types were made using different fillers—graphite, CNT, and a graphite-CNT mix—added to the GCP-elastomer matrix (Figure 3.8(c)). The CNT filler enhanced stretchability beyond 200% but with minimal resistance change (gauge factor of 0.8). The addition of graphite particles increased the gauge factor to 96, but reduced stretchability to 75% due to crack formation in the GCP-elastomer matrix. In contrast, CNTs formed a bridging network, improving sensor performance by connecting separated GCP regions

during stretching. The combined graphite-CNT filler yielded an optimal sensor response, with a gauge factor of ≈2404 and resistance change of ≈1400 at 100% strain.

For further analysis, five devices with varying GCP ratios in Sample 2 (0 wt%, 50 wt%, 100 wt%, 150 wt%, and 200 wt%) were fabricated, and their resistance changes under strain were plotted in Figures 3.8(d-f). As GCP content increased, stretchability decreased while the gauge factor increased. For example, adding 50 wt% GCP reduced stretchability from 625% to 500%, but increased the gauge factor from 10.8 to 570 (Figure 3.8(e)). Further increases in GCP loading (100 to 150 wt%) led to greater reductions in stretchability (125% to 45%) and dramatic rises in gauge factor (23,366 to 1,834,140) as shown in Figure 3.8(f).

The hysteresis behavior was systematically analyzed by incorporating varying ratios of GCP into Sample 2 (Figure 3.9(a–d)). Since GCP is inherently nonelastic and contains multiple grain boundaries that can separate under external strain, it tends to break into smaller islands, significantly reducing conductive pathways and increasing the film's resistance. When the stress is removed, these separated islands reconnect, re-establishing conductive paths nearly identical to the original film. A similar pattern was observed as GCP content increased in Sample 2, where the addition of GCP improved sensor performance and minimized hysteresis.

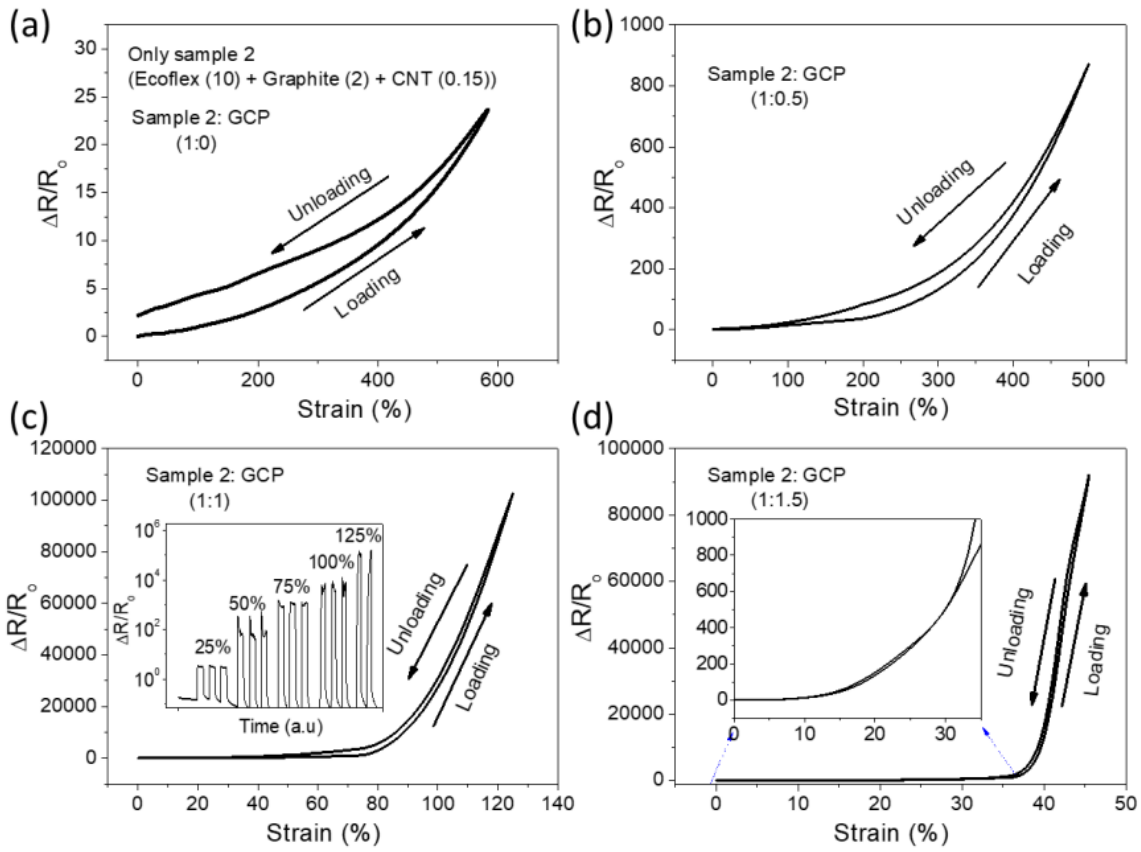

Figure 3.9: Comparison of sensor performance with different loading of GCP to sample 2 namely (a) 0wt.% GCP, (b) 50 wt.% GCP, (c) 100 wt.% GCP, and (d) 150 wt.% GCP. Inset in figure (c) shows the cyclic sensor response at different strain and the inset in figure (d) shows the magnified graph highlighting the sensor response in low strain region

The real-time sensor response was evaluated through systematic stretching and releasing cycles at various strain levels for the 100 wt% and 150 wt% GCP samples to assess their response time and reliability. During each cycle, the resistance was continuously measured as the sensor was stretched and held for 15 seconds, followed by a release for another 15 seconds, as shown in Figure 3.10(a-b). In both samples, the resistance sharply increased from the baseline when external strain was applied, with the relative change in resistance reaching a maximum of approximately 10^5. Notably, the sensors exhibited a fast response time of 0.4 seconds and a recovery time of 0.3 seconds (Figure 3.10(c)). Additionally, the sensors showed stable performance, with resistance returning to baseline in under a minute during a 10-second stretch-and-release cycle for over 1200 seconds (Figure 3.10(d)).

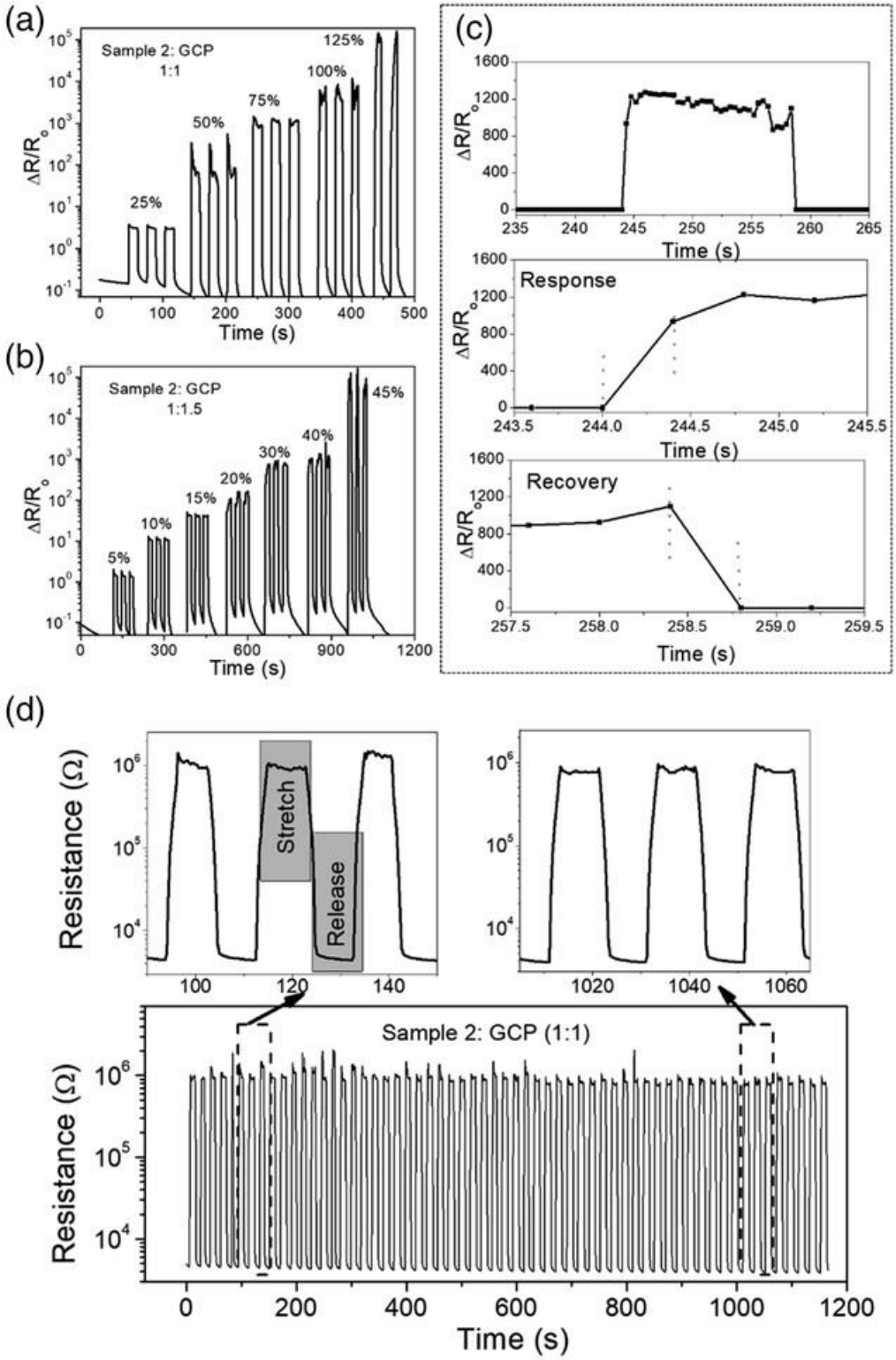

Figure 3.10: Electromechanical performance of elastomer–GCP–filler composite: The relative resistance change during systematic 15 s stretch cycles at various strain levels for sensors with: a) 100 wt% GCP in Sample 2, and b) 150 wt% GCP in Sample 2; c) Detailed sensor response and recovery time extracted from Figure 4a; d) Real-time resistance variation during a 10 s stretch-and-release cycle over 1200 s for 100 wt% GCP in Sample 2.

Sensors, with and without 150 wt% GCP, were also preserved for six months and they were subjected to 750 stretching cycles at 200% and 40% strain, respectively to check whether the sensors lose any properties with time. Interestingly, the sensor's performance, indicated by the relative change in resistance, remained stable even six months after fabrication (Figure 3.11(a-b)).

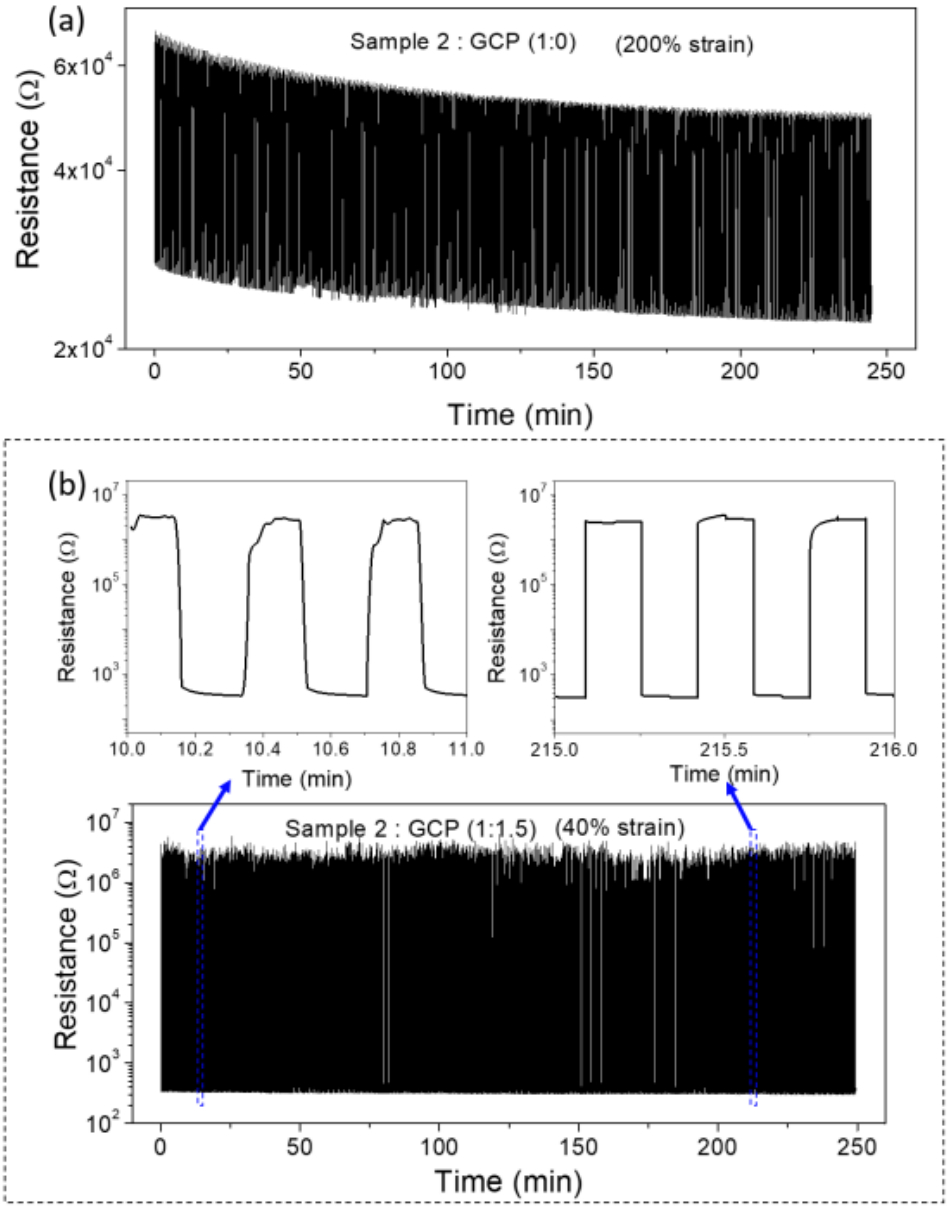

Figure 3.11: Real time resistance change under systematic stretch and release cycle of 10 s each for 750 cycles. The cyclic response is for sample 2 with (a) 0 wt.% GCP at 200% strain, and (b) 150 wt.% GCP at 40% strain.

Sensor performance reproducibility was also evaluated in this study. Five sensors with varying composition were fabricated and it was observed that the response across the five sensing devices was consistent, with a standard deviation of less than 5% (Figure 3.12). As GCP loading increased, the sensor's stretchability decreased; the sensor with 100 wt% GCP reached its maximum relative resistance change (10^5) at 125% strain, while the 150 wt% GCP sensors achieved this at a significantly lower strain of 45%.

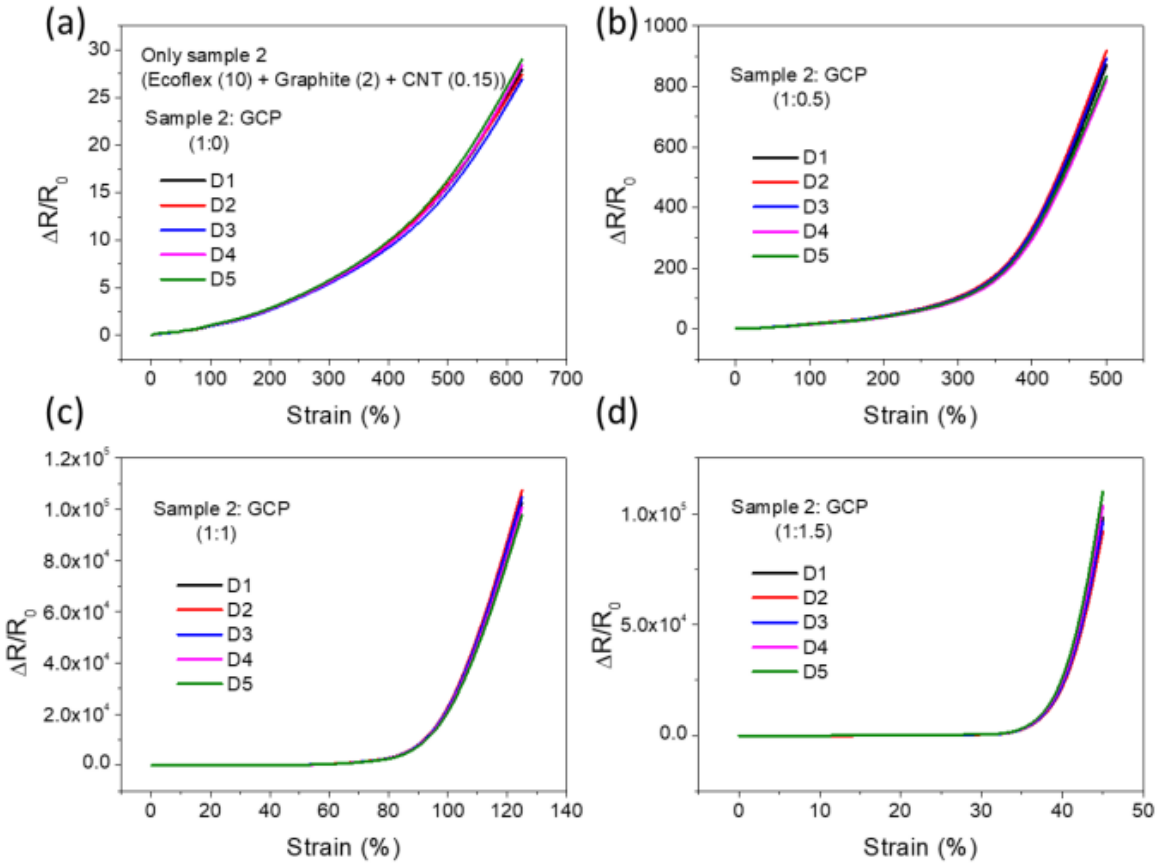

Figure 3.12: Device to device reliability test among 5 devices: (a) 0 wt.% GCP, (b) 50 wt.% GCP, (c) 100 wt.% GCP, and (d) 150 wt.% GCP in sample 2

3.3.3. MD simulations of sensing material

To investigate the role of GCP in sensor response and stretchability, MD simulations were conducted on the elastomer matrix, both with and without GCP. The simulation results, shown in Figure 3.13, demonstrate that the composite containing GCP exhibits voids at

around 70% strain, leading to cracking at 110% strain. In contrast, the composite without GCP shows no signs of cracking even at 110% strain. The graphene and carbon black in the GCP increase the density of fillers in the elastomer matrix, leading to strong particle-particle interactions and agglomeration due to weak van der Waals forces. It was also observed that microcracks form perpendicular to the stretching axis. The formation of multiple cracks reduces the number of conductive paths, causing a significant increase in the relative change in resistance with higher GCP loading, as shown in Figure 3.5(b). In contrast, the samples without GCP or with lower GCP content show smaller changes in resistance, as more conductive paths remain intact. These simulation findings align with the experimental results, indicating that the addition of GCP reduces stretchability while enhancing sensor response.

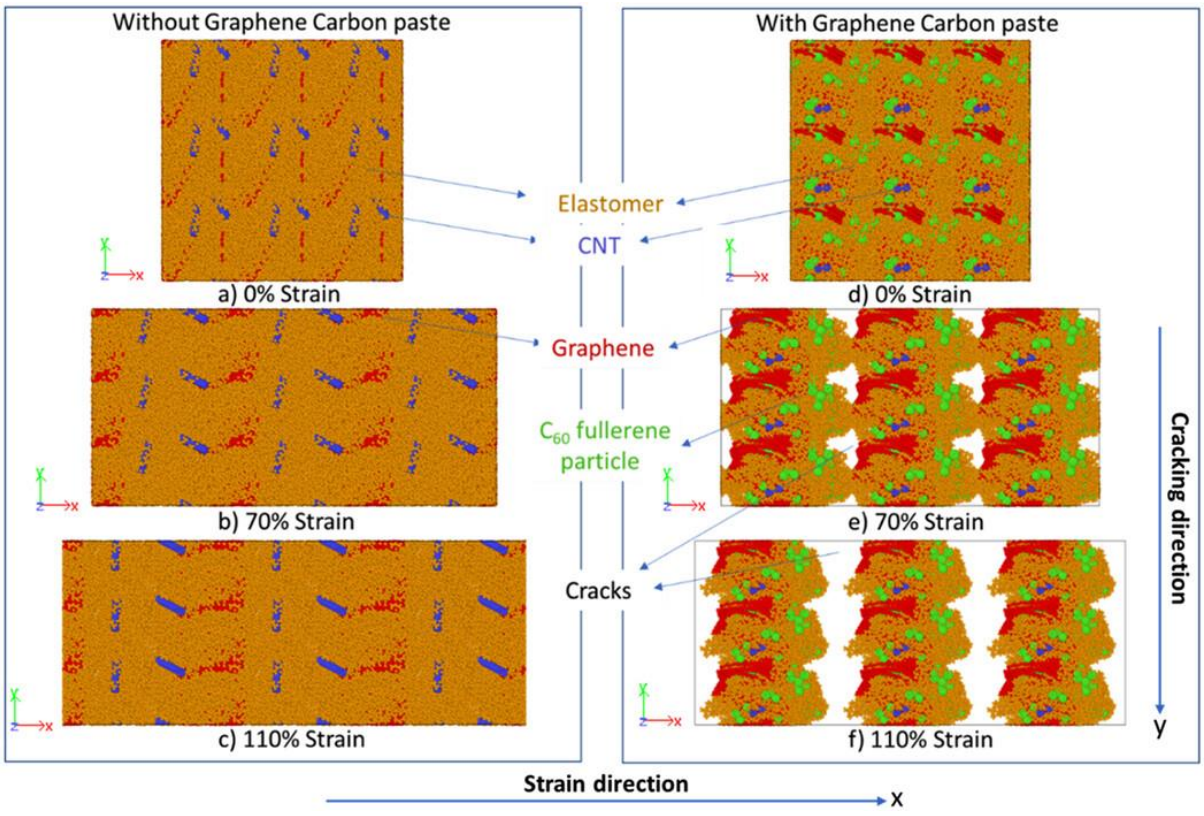

Figure 3.13: Snapshots from MD simulations for elastomer (PDMS)–GCP–filler composite.

3.3.4. Neuromorphic strain and bend sensing system based on developed sensors

Now, I will discuss about the neuromorphic system developed using the strain sensors highlighted in previous sections. As discussed in sections 3.2.1 and 3.2.2, one of the strain sensors having sensing layer composition as ecoflex, graphite and GCP in the weight ratio of 10:1:10 was attached to a wheatstone bridge and the output voltage of this circuit was fed to a LIF neuron encoding model. For demonstrating the application of such neuromorphic systems, two scenarios were taken i.e. unidirectional stretching and finger-joint bending.

Figure 3.14 illustrates the neural encoding process of converting strain sensor data into spiking signals when the sensor is stretched at various strain levels. As the sensor is stretched, structural changes in the sensing material's percolating network (graphite and GCP particles) cause its resistance to increase. This change in resistance is converted into sensor voltage (V_{sensor}) via a Wheatstone bridge circuit. Figure 3.14(a) shows that as strain increases, the sensor voltage rises in line with the resistance. The membrane voltage (V_{mem}) responds to V_{sensor}, spiking only when V_{sensor} exceeds the threshold voltage (V_{thr} = 0.2 V), effectively filtering out noise. Once V_{mem} reaches the threshold, a spike is generated, and it immediately resets to 0 V, repeating the process with each new input, as shown in Figure 3.14(b). At higher strain levels, V_{sensor} increases, resulting in a higher spiking frequency (Figure 3.14(c)), resembling the behavior of afferent nerve fibers as discussed in Chapter 2. Figure 3.14(d) shows that the spiking rate rises from 7 to 26 per minute as the strain varies from 5% to 50%, which exceeds the maximum strain typically experienced by human skin (about 30%)[210, 211].

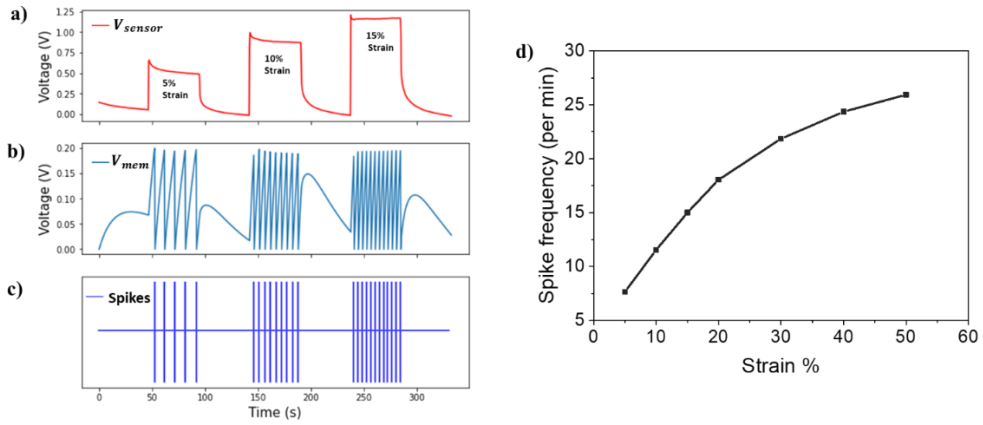

Figure 3.14: (a) Output voltage from wheatstone circuit at various stretching conditions, (b) corresponding changes in membrane voltage, (c) Generated spike signals from the simulated LIF neuron, (d) Relationship between spike frequency and strain levels

The strain-sensing mechanism was tested to mimic proprioceptors that detect finger joint bending. Sensors were placed on a finger joint (Figure 3.15(a)) and bent at various angles. The output spiking rate from the simulated LIF neuron increased proportionally with bending, as shown in Figure 3.15(b). The spiking rate ranged from 7 to 14 spikes per minute at different angles as shown in Figure 3.15(c), establishing a direct relationship between bending angles and spike rates.

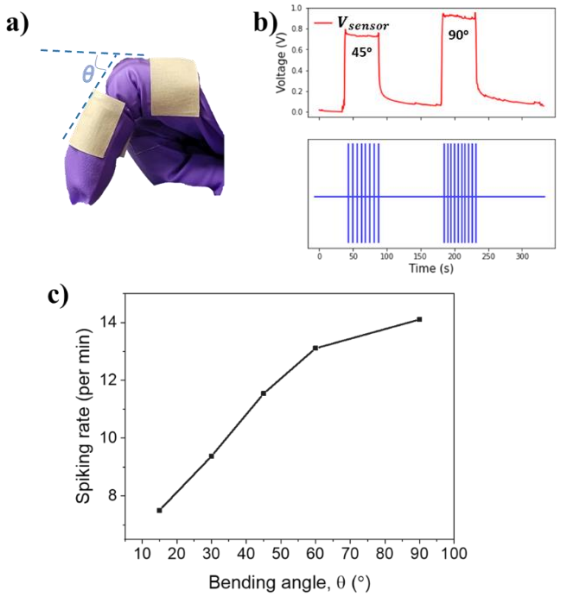

Figure 3.15: (a)Sensor mounted on finger joint to estimate its bending. (b) Output voltage from wheatstone circuit and spiking behaviour of simulated LIF neuron at 45^0 and 90^0 bending angles. (c) calculated relationship between spiking frequency and finger bending angles.

3.4. Summary

This chapter presents the development of a high-performance stretchable strain sensor designed for detecting human motion, with a focus on achieving wide-range stretchability, high sensitivity, and reliability. By incorporating carbon-based fillers and graphene-carbon paste (GCP) into an elastomer matrix, the sensor's performance is significantly enhanced. The elastomer-filler composite offers superior stretchability, while the addition of GCP increases sensitivity through crack formation under small strains. A sensor with 50 wt.% GCP loading demonstrated 500% stretchability and a gauge factor of 504, while increasing the GCP to 150 wt.% achieved 45% stretchability and an impressive gauge factor of 1,834,140. These sensors can detect both small- and large-scale strains, making them ideal for monitoring facial expressions and joint movements.

Additionally, the chapter explores the development of an artificial tactile system, mimicking human proprioception. The system uses the developed strain sensor, integrated with a Wheatstone bridge and a simulated leaky-integrate-and-fire (LIF) neuron, to generate neural spike trains corresponding to different strain levels. The spiking rate increased from 7 to 26 spikes per minute as strain ranged from 5% to 50%, mirroring the behavior of mechanoreceptors in human skin. This research advances the development of smart robots, prosthetics, and tactile sensors, enhancing their sensory and proprioceptive capabilities.

Chapter 4

Hybrid Capacitive-Triboelectric Pressure Sensor System for Enhanced Human-Like Tactile Sensing

This work is adopted from:

Journal Article:

- **Mishra, S.,** Nair, NM., Khandelwal, G., Rai,B., Georgiev, V., Capacitive-Triboelectric based Hybrid Sensor System for Human-like Tactile Perception, *IEEE Sensors Letters*, 8, 5500404 (2024)

Abstract:

Human skin contains slowly-adapting (SA) and rapidly-adapting mechanoreceptors (RA) through which it can discriminate between static and dynamic tactile stimuli. Bio-mimicking of such human tactile sensing systems using flexible and reliable sensors has recently gained importance for developing future robots and prosthetics with better sensory capabilities. In this work, a hybrid flexible sensor system consisting of a capacitive pressure sensor (CPS) (mimicking SA mechanoreceptors) firmly stacked over a triboelectric nanogenerator (TENG) (mimicking RA mechanoreceptors) was developed. CPS consisted of porous Ecoflex as the dielectric material, while the two layers used in

TENG were made using copper-nickel conducting fabric and ITO-coated PET sheet. This hybrid sensor system was characterized and showed good sensitivity for CPS and voltage response for the TENG device. Later, three distinct scenarios for the hybrid system have been demonstrated, in which it was used for the qualitative hardness assessment, slip detection and impact/vibration detection. In summary, the signals from both CPS and TENG complement each other, making this hybrid sensor system capable of simultaneously detecting both static and dynamic pressure signals.

4.1. Introduction

Human skin perceives the complex spatiotemporal patterns of external stimuli like touch, pressure, vibration etc., through various mechanoreceptors present in our skin. In general, these mechanoreceptors are of two types: slowly adapting (SA) and rapidly adapting (RA) (Figure 4.1(a)). The key function of SA mechanoreceptors is to provide information about the static or sustained aspects of touch and pressure[212]. They enable us to recognize and understand the shape, texture, and deformation of objects we touch. On the other hand, RA mechanoreceptors detect changes in touch and pressure quickly, and it plays a critical role in identifying dynamic and transient sensory information, including fine textures and vibrations[17]. Together, these receptors enable the skin to gather a wide range of tactile information, contributing to our ability to interact with and understand the physical world around us.

In recent times, biomimicking of human skin tactile perception system through fabrication of electronic or e-skin have gained importance for applications in human-machine interface, robotics and prosthetics or artificial limbs[14, 87, 95, 96, 213]. Traditionally, these e-skins are embedded with single type of pressure sensors like capacitive, piezoresistive, triboelectric, piezoelectric etc. through which it is difficult to sense both static pressure and vibrations simultaneously[192, 214, 215]. However, both

pressure and vibration sensing modalities are important for texture recognition, slip detection and object manipulation in various applications. Thus, to attain skin like properties, it is essential to put together multiple sensors that can sense both static pressure as well as dynamic properties like vibrations as well.

There are few previous works based on hybrid sensors to mimic both SA and RA like capabilities. For example, Chun et al. [30] made a self-powered sensor based on an artificial ion-channel combined with piezoelectric film. In another work, a capacitive pressure sensor (CPS) was integrated with a piezoelectric sensor to give both static and dynamic pressure signals[187]. On similar lines, in this work, we have made a hybrid sensor where a highly sensitive CPS was stacked over a triboelectric nanogenerator (TENG) device to discriminate the static and dynamic external pressure stimuli, as depicted in Figure 4.1(b). A porous Ecoflex-based CPS was used because of its simple device structure, low power consumption, temperature independence, good reliability, and better sensitivity due to its porous nature. This CPS mimics the skin SA properties by providing signals related to low frequency or static pressures. TENG device was made using combination of copper-nickel conducting textile and Indium tin oxide (ITO)-coated polyethylene terephthalate (PET) sheet as active layers. TENG device provides a response during dynamic changes in the external stimuli due to the voltage generated during contact-separation of the two layers. The advantage of TENG device is that it doesn't require any external power source, is responsive to a wide pressure range, is low-cost and is lightweight. Further, this hybrid sensor system was applied by demonstrating the hardness assessment, slip, and vibration detection of objects by deconvoluting the information from these stacked device structures.

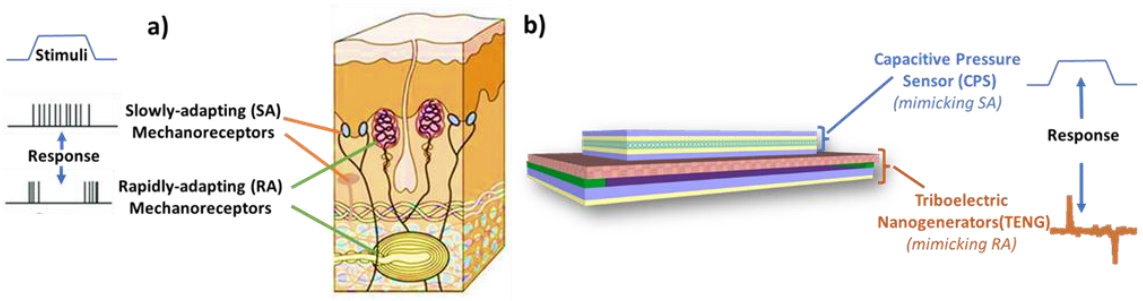

Figure 4.1: (a) Slowly-adapting (SA) and rapidly-adapting (RA) mechanoreceptors in human skin that help in discriminating static and dynamic external pressure stimuli. (b) Design of the hybrid sensor system used in this work. It consists of a capacitive pressure sensor (CPS) (mimicking SA) stacked over a triboelectric nanogenerator (TENG) (mimicking RA).

4.2. Materials and Methods

4.2.1. Fabrication Method

In this work a CPS was stacked over a TENG device to make the hybrid sensor system as shown in Figure 4.2(a). CPS used in this work has a parallel plate structure and consists of porous Ecoflex as the dielectric (of size 1.5 cm × 1.5 cm × 0.5 cm) and ITO-coated PET as the electrodes, as shown in Figure 4.2(b). Ecoflex is selected as the dielectric material of the capacitive pressure sensor because of its low elastic modulus and high dielectric constant in comparison to other soft materials such as PDMS[78]. The porosity will help to further reduce the elastic modulus, thereby more deformation to the external pressure, and hence the capacitive variations Sugar granules were filled in a mould that served as the template for the porous structure[216, 217]. Ecoflex 00-30 silicon rubber, prepared by mixing part A and part B in a 1:1 ratio, was poured into the mould and cured for 24 h at room temperature. After curing, the structure was removed from the mould and immersed in water for 5 h to dissolve the sugar granules completely. The structure was then cured at 100 ºC for 1 h to remove the excess water and then porous Ecoflex was obtained as seen in Figure 4.2(c). Figure 4.2(d) shows the zoomed optical microscopy image of the porous Ecoflex. The calculated average pore diameter in Ecoflex obtained was around 0.68±0.12 mm. The pore size is tunable by controlling the particle size of the

sugar granules [218]. The formed porous Ecoflex was stacked between two ITO-coated PET sheets with 60 Ω/sq—sheet resistance, purchased from Sigma Aldrich, to complete the parallel capacitive pressure sensor structure.

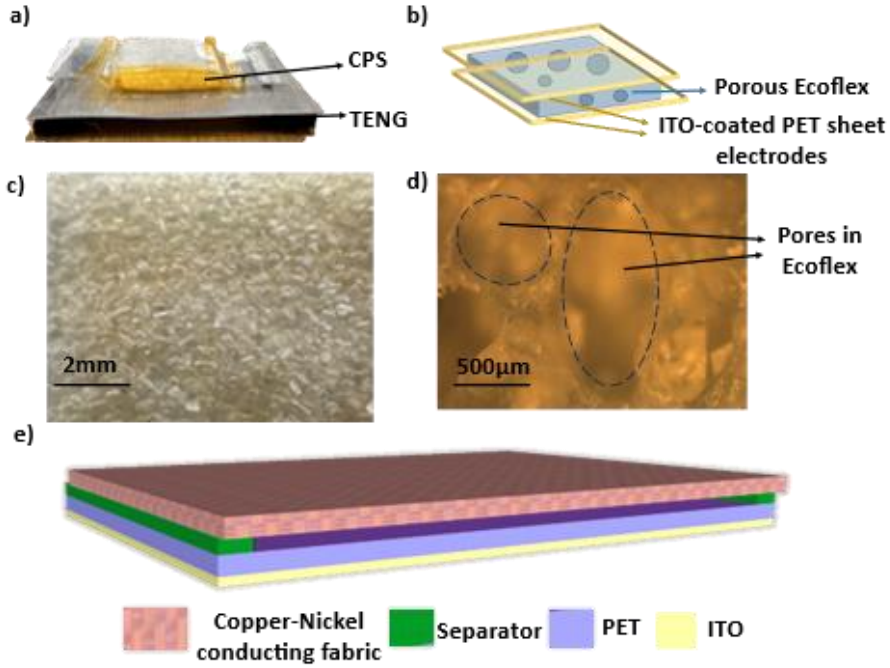

Figure 4.2: (a) Design of hybrid sensor developed, (b) design of CPS, (c) and (d) shows the optical microscopy of the porous Ecoflex used as dielectric in CPS and (e) design of the TENG device.

For fabricating the TENG device, two different sheets of copper-nickel conducting fabric and ITO-coated PET sheets (purchased from Sigma Aldrich) were chosen as active layers because of their easy accessibility, good flexibility and reliability properties as depicted in Figure 4.2(e). Then, they were stacked over each other with a constant separation of 4 mm using a separator. The top layer was copper-nickel conducting fabric, which functions as the electrode and charge-generating layer. For the bottom layer, an ITO-coated PET sheet was used where the PET side of the sheet was used as the charge-generating layer and ITO side was used as the charge collecting layer or electrode. Finally, the connections were taken out using copper wires. The dimensions of the resultant device were 3 cm × 4 cm.

4.2.2. Device characterisation

A E4980AL precision LCR meter (Keysight Technologies, Santa Clara, CA, USA) was used for capacitance measurement using a LabVIEW 2018 program. An electrodynamic shaker (TIRA, TV50018, Germany) was used to provide the pressure (sinusoidal cyclic loading and unloading as well) and vibration stimuli to the device. The voltage from the TENG device was measured using Keithley 6517B electrometer.

4.3. Results and Discussion

4.3.1. Device Performance of the hybrid sensor stack

Sensor characterisation for both CPS and TENG in the hybrid sensor system was carried out as depicted in Figure 4.3. For evaluating the performance of CPS in the hybrid sensor system, the system was loaded/unloaded at different step pressures between 1.4 to 22 kPa and the capacitance variations are shown in Figure 4.3(a). The response curve of CPS showing relative change in capacitance at different pressures was evaluated as shown in Figure 4.3(b) and three linear zones with different sensitivities were observed. Initially the sensitivity was 6% kPa^{-1} in the pressure range of 0-2.5 kPa, which decreased to 4% kPa^{-1} in the pressure range of 2.5-12.5 kPa. This finally got reduced to 2% kPa^{-1} between 12.5-23 kPa. The highest sensitivity value of 6% kPa^{-1} is lower than previous literature values [219] for porous Ecoflex-based sensors mainly because it is stacked over the flexible TENG that absorbs some pressure and deforms. However, the long-term stability of CPS, as shown in Figure 4.3(c), by observing the relative change in capacitance under cyclic loading and unloading with 2.2 kPa pressure at 0.5Hz frequency for 1000 cycles confirms that the CPS performance is reliable over a significant duration. There is little residual relative change in capacitance after each cycle (around 2%) because of presence of residual strain in porous Ecoflex after each cycle as there isn't sufficient recovery time for it to regain to its original shape. Figure 4.3(d-e) shows the output voltage profile of

the TENG in the hybrid stack with different applied frequencies (1-8 Hz) and pressure (3-22.4 kPa). Both the profiles show the typical TENG characteristics of increase in output voltage with both increasing pressure and frequency. Figure 4.3(f) shows the good stability of TENG while Figure 4.3(g) depicts the current output from the TENG.

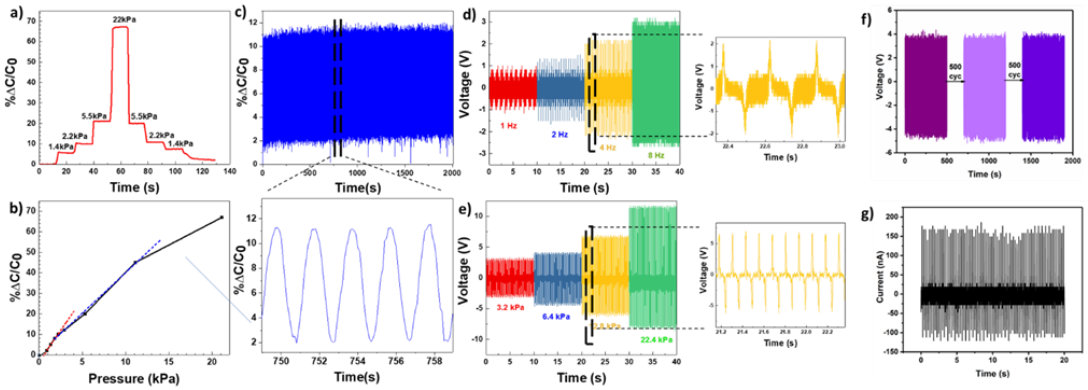

Figure 4.3: Relative change in capacitance in CPS during: (a)Stepwise load/unload process, (b)at different pressure values and (c) cyclic sinusoidal loading and at 2.2 kPa for 1000 cycles at 0.5Hz and its magnified graph below between 749-759s shows good stability and reliability of the CPS over long duration. Voltage generated by TENG at: (d) different frequencies for constant pressure of 6.4kPa and right graph shows magnified image of it and (e)different pressure magnitude at constant 8 Hz frequency and right graph shows magnified image (f) shows the stability of the TENG device and (g) shows the current output of TENG device.

4.3.2. Applications

To demonstrate the practical applications of the fabricated hybrid sensor, it was affixed onto a nitrile glove worn by a human, as depicted in Figure 4.4(a). Subsequently, three distinct experiments with atleast five trials in each experiment were conducted.

First, a qualitative hardness assessment of objects using the hybrid sensor was performed. Initially, a soft yellow ball (depicted in Figure 4.4(a)) was picked up and held for 5 seconds before being returned. Throughout the process of picking up, holding, and placing the ball, as the CPS gets pressed continuously, it generates a continuous capacitance change. However, TENG voltage signals were only obtained during the pick-up and placement phases. This happens because contact electrification in two layers of TENG, which gives rise to TENG voltage signals happens only during dynamic change in layers contact. A similar observation was made when picking up, holding, and placing

a water bottle. Notably, the magnitude of relative capacitance changes in CPS during bottle holding was more pronounced due to the water bottle's greater hardness compared to the soft ball. This demonstrates that both CPS and TENG signals can be employed to discern whether an object is picked up and replaced using the gloves. Furthermore, the relative changes in CPS readings can be utilized to gauge the hardness of the manipulated object.

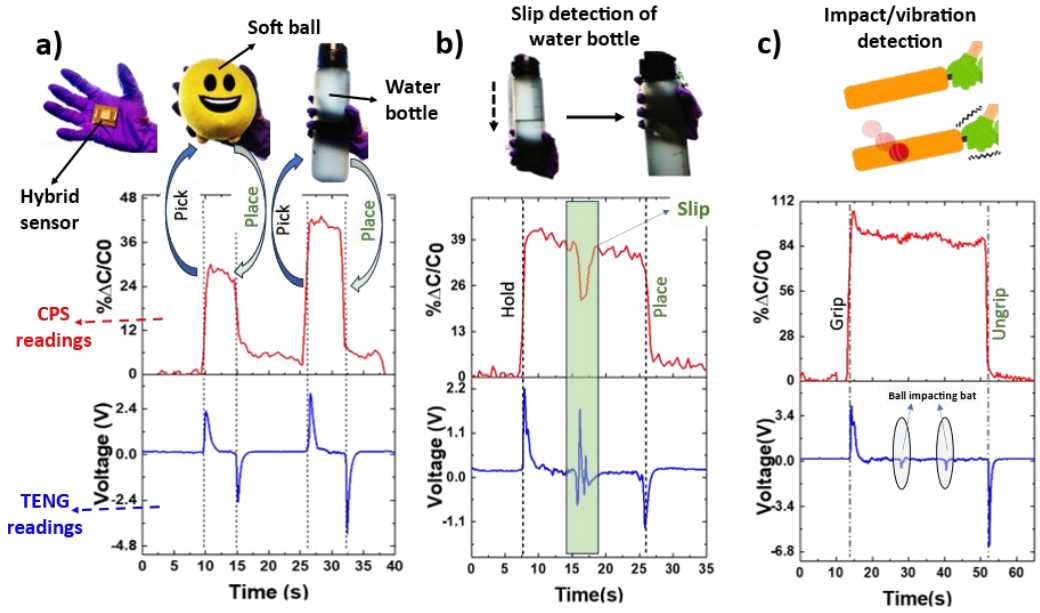

Figure 4.4: (a) Hybrid Sensor attached on nitrile glove and the readings of CPS and TENG during pick and place of soft ball and water bottle as shown (b)Slip detection of water bottle through CPS and TENG readings and (c) impact/vibration detection when ball is thrown at a cricket bat.

Secondly, a water bottle was picked up and aimed to detect any slipping motion. It was observed (as shown in Figure 4.4(b)) that during the bottle's slipping motion, the relative capacitance change of CPS decreased slightly due to the loose grip, but it returned to its original value once the bottle was securely held. In contrast, the TENG's output voltage exhibited a series of peaks in both positive and negative directions during the bottle's slipping motion because there is a continuous change in the contact between layers of the TENG during the slipping motion. This indicates that the TENG component of the hybrid sensor effectively mimics the functionality of skin's RA mechanoreceptors and can detect dynamic motions.

Lastly, the hybrid device was placed in the glove used to hold the cricket bat and the ball was thrown twice with a specific time interval between the throws. Figure 4.4(c) depicts no observed changes in the relative capacitance of the CPS during the ball's impact on the bat. However, on both occasions, the TENG output displayed signals during the ball's impact with the bat. This illustrates that the TENG part of the hybrid sensor successfully sensed the vibrations, which static sensors like CPS cannot detect. In summary, the signals from both CPS and TENG complement each other, making this hybrid sensor capable of simultaneously detecting both static and dynamic pressure signals and thus emulating a few tactile functionalities of human skin.

4.4. Conclusion

In this chapter, a hybrid sensor system comprising of CPS stacked over a TENG was developed. Both the sensors were characterised and demonstrated for reliable sensing response. The complementary signals provided by the hybrid sensor were implemented for practical applications by showcasing its ability to perform qualitative hardness assessment, detect slipping motion, and identify impacts and vibrations. These systems can help in making smart gloves and prosthetics and could pave the way for the development of next generation robots and artificial limbs.

Chapter 5

FEM Analysis of ZnO Nanowires Enabled Soft Capacitive Pressure Sensors

Some parts of this work are based on following publications:

Conference Paper

- **Mishra, S.,** Baghini, M.S., Shathivel, D., Rai, B., Dahiya, R., "Sensitivity analysis of ZnO NWs based soft capacitive pressure sensors using finite element modeling", *2022 IEEE FLEPS Conference,* Vienna, Austria

Abstract

Soft and flexible pressure sensors are essential components in large area electronic skin and their application in the field of robotics and human-machine interfaces. For attaining good sensitivity and reliable properties, soft capacitive pressure sensors based on elastomeric dielectric material and piezoelectric nanowires (NWs) have shown promising results in the low-pressure range of 0-10 kPa. In last chapter, fabrication methodology and performance of soft flexible pressure sensor was discussed. In this work, soft capacitive pressure sensors based on ZnO NWs incorporated into polydimethylsiloxane

(PDMS) dielectric material were simulated using finite element methods (FEM) to investigate the piezoelectric properties of ZnO NWs and its influence on the sensitivity of the sensors. The effect of ZnO NWs along with their orientation and aspect ratio on sensor's mechanical properties as well as sensitivity has also been discussed. The simulations indicate that the addition of ZnO NWs enhance the sensitivity of PDMS based sensors by ~3 times. Vertical ZnO NWs based sensors show better sensitivity than sensors with lateral ZnO NWs. Additionally, increasing the aspect ratio in vertical direction further enhances the sensitivity of the sensor with no significant impact on the mechanical properties of the sensor. Average piezoelectric polarisation and strain in each ZnO NW were also evaluated and they indicate higher polarisation in higher aspect ratio ZnO NWs which directly correlates with the sensitivity enhancement of the pressure sensor. The predicted values and trends were found to match well with previously reported experimental results. This chapter shows the potential of FEM simulations in optimizing the sensor design as well in understanding the underlying physics of the sensor's working mechanism.

5.1. Introduction

Soft and flexible sensors are key enablers for the development of electronic skin that has implications in the areas such as wearable systems, robotics, human-machine interfaces, prosthetics, and healthcare applications [13, 53, 54, 87, 102]. In that regard, mimicking the sensory capabilities of human skin is being attempted by various researchers. As mentioned in Chapter 2, pressure sensing is a vital component in biological e-skin which plays a crucial role in deciding how humans and animals interact with surroundings spontaneously. The human tactile sensing system helps to perceive touch (soft and hard), texture, shape, impact, vibrations, hardness, object recognition etc which allows smooth interaction with surroundings. Emulating such sensing capability through artificial e-skin

require carful design and meticulous fabrication of soft flexible pressure sensors with high sensitivity over wide pressure range i.e soft, medium, and hard touch[4, 11]. The crucial figure of merits for an e-skin sensing element are form factor, high sensitivity in the soft touch domain, fast response (~ms), low hysteresis, mechanical compliance, and low operating voltage. These requirements commonly met by a soft capacitive pressure sensor generally includes an elastomeric dielectric material like ecoflex, polydimethylsiloxane (PDMS), polyurethane (PU) etc. sandwiched between two electrodes[23, 65].

As explained in Chapter 2, the working mechanism of these PDMS elastomer based flexible capacitive pressure sensors resemble that of a conventional parallel plate capacitor. The capacitance of these sensors depends on the intrinsic parameters such as relative permittivity of the dielectric material (PDMS), area of the planar electrodes and separation (d) between them. These parameters vary when an external pressure is applied and thus, changing the capacitance of the sensor. So, varying these parameters by altering the PDMS microstructures or introducing inorganic nanostructured fillers (i.e., carbon nanotubes, graphene, silver and ZnO NWs etc.) in the matrix or combination of both enable better sensitivity of the sensor.

For example, sensitivity of pristine PDMS based sensor lies in the range of 0.01-0.016 kPa^{-1} , whereas, micro-arrayed PDMS structure-based sensors have sensitivity in the range of 0.6-2 kPa^{-1} in the pressure range of 0-2 kPa[220]. However, these sensors have drawbacks of limited working pressure range where they exhibit good sensitivity, delicate surface, and bulk microstructures prone to hysteresis effects and intricate fabrication techniques with areal restrictions. Alternatively, inorganic filler-based approaches offer many possibilities to engineer the capacitive structure to overcome the aforementioned drawbacks. Addition of metallic nanostructured fillers such as CNT, Ag NWs etc

contributes to improve charge transport than overall sensitivity[65, 221]. In this regard, piezoelectric NWs/particles such as ZnO, $BaTiO_3$ etc. were incorporated in the soft elastomer matrix which showed improved sensitivity while increasing the working pressure range 0-50 kPa[222, 223] (Figure 5.1). This pressure range is more appropriate for applications in e-skin to recognize soft and medium touch applied through external objects. The performance of the above three PDMS matrix based capacitive sensors are compared (Table. 5.1) in this pressure range which shows the suitability of oxide-based NWs to achieve high figure of merits. ZnO NWs are being explored as the preferred filler material for PDMS matrix due to single crystallinity, anisotropic structure, excellent dielectric, piezo electric and biocompatibility properties. Further, it can be conveniently grown in the sub-100 dimensions using vapour and hydrothermal synthesis process followed by spin-coating on various substrates[89]. Recently, capacitive sensors with ZnO NWs acting as interlayers between each PDMS-electrode interface was reported to effectively use its dielectric and piezoelectric properties [87]. An increase in sensitivity (~ 2-7 times) was observed in the pressure range of 0-10 kPa when compared with sensors based on bare PDMS.

Table 5.1: PDMS based sensor comparison with different microstructures and filler material

PDMS structure	Filler	Sensitivity (kPa^{-1})	Working Pressure Range (kPa)	Ref.
Planar	-	0.01-0.016	0-2	[102]
Micropillars	-	0.55	0-2	[224]
Porous	-	1.18	0-0.02	[55]
Planar	Carbon nanotubes	0.0066	0.240	[71]
Porous	Silver nanoparticles	0.11	0-1	[225]
Porous	Boron Nitride	0.854	0-0.5	[226]
Porous and micropillars	Barium Titanate	7.847 0.871 0.06	0-1 1-7 7-25	[85]
Planar	Zinc Oxide Nanowires	0.056	0-10	[87]

In general, incorporation of ZnO NWs filler in the PDMS strengthens the dielectric properties of the matrix and enhances the sensitivity of the capacitive sensor additionally using its inherent piezoelectric characteristics. However, the correlation of dielectric and piezoelectric properties of ZnO NWs through the application of pressure that drives the enhancement of sensitivity of the sensors is still unclear from the experimental works. Further, being anisotropic material there is a variation in the sensitivity of the sensors when ZnO is embedded in different orientations in the sensor structure (Figure 5.1). So, inspired by the design of the sensors used in the previous work [87], in this study we demonstrate the effect of addition of ZnO NWs, the influence of their aspect ratio and the orientation on the sensitivity of pressure sensors using Finite element method (FEM) simulations. Further, we tried to understand the driving mechanism (dielectric or piezoelectric) behind sensitivity enhancement. The simulation results have been validated against the previously reported experimental results and trends. Importantly, the work focused on the influence of piezoelectric effect of ZnO NWs on the sensitivity in the pressure range of 0-10 kPa and validated the effect for the soft sensing applications. We believe that the presented simulation study will aid in understanding the functioning and design the soft capacitive pressure sensors using piezoelectric NWs for e-skin application.

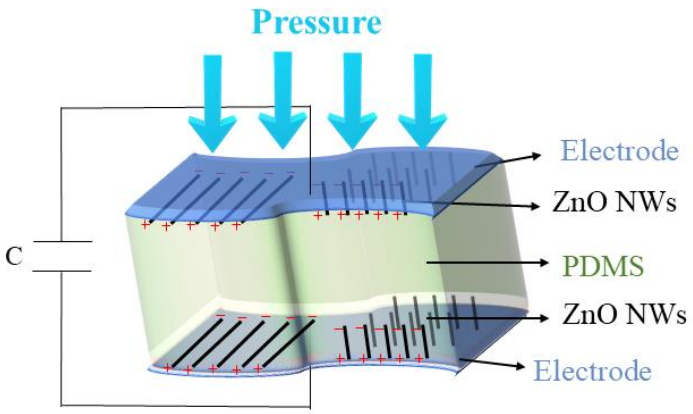

Figure 5.1: Schematic illustration of the presented PDMS based soft capacitive pressure sensor with two configurations of ZnO NWs embedment.

5.2. Simulation Methodology

In this work, initially, the effect of orientation of ZnO NWs on sensitivity of the pressure sensor has been studied. To perform this study, three configurations of sensors were considered as shown in Figure 5.2. A block of PDMS with dimensions 10 μm x 10 μm x 50 μm was used to calculate the sensitivity of pure PDMS based sensor and this was designated as configuration 1 as shown in Figure 5.2(a, d). In configuration 2, 144 cylindrical lateral ZnO NWs (forming 9 stacked horizontal layers of ZnO NWs with 16 NWs in each layer) were embedded near the top and bottom surfaces along z-axis inside a PDMS block having dimensions same as configuration 1 such that PDMS just encapsulate and keeping the nanowires near the electrodes which generally the case in experimental conditions as shown in Figure 5.2(b, e). Encapsulation eliminates the practical problems of plastic deformation of nanowires during the application of pressure. Similarly, in configuration 3, 16 x 16 vertical array of ZnO NWs (having their axis in z-direction as depicted in Figure 5.2(c, f) were placed uniformly in x- and y- direction near both the surfaces of PDMS in z-direction. Further, to study the effect of aspect ratio on the sensitivity of pressure sensor, the length (L) and radius (R) of the ZnO NWs were varied, and Table 5.2 shows the dimensions of ZnO NWs used in different sensors with their corresponding configurations. In all the cases the volume fraction, and the number of ZnO NWs inside the PDMS were kept constant. All the simulations were carried out in COMSOL® 6.0. Both Solid Mechanics and Electrostatics modules of COMSOL® were coupled together via the Piezoelectric Effect Multiphysics to carry out the simulations. In addition, to quantify the effect of piezoelectric effect of ZnO NWs on the sensitivity of the sensor, air was considered as dielectric material outside the sensors and moving mesh method was used to model the interaction between air and the sensors.

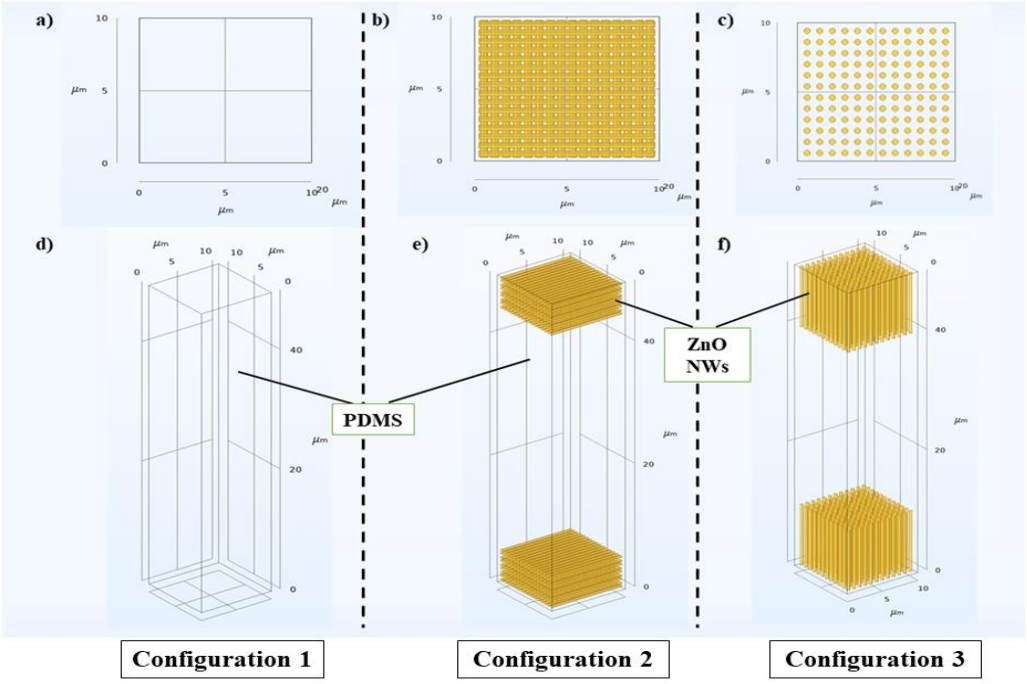

Figure 5.2: Geometry for three configurations (1, 2 and 3) used in the simulations. (a-c) are top view and (d-f) are their perspective views

Table 5.2: Configuration and dimensions of different sensors simulated (here P, H1 respectively and V(1-5) stands for pdms, horizontal and vertical)

Sensor/ Properties	P	H1	V1	V2	V3	V4	V5
Configuration	1	2	3	3	3	3	3
Radius of ZnO NW (in µm)	-	0.2	0.2	0.28	0.23	0.18	0.163
Length of ZnO NW (in µm)	-	9.5	10	5	7.5	12.5	15
Aspect Ratio (L:R)	-	47.5	50	17.68	32.5	69.9	91.86

PDMS was assumed to be purely elastic and dielectric material and its behavior was governed by Hooke's law (1) and Poisson's equation (2):

$$T = cS \tag{5.1}$$

$$\nabla . D = \rho_V \tag{5.2}$$

where T, S, c, D, and ρ_V are stress tensor, strain tensor, stiffness tensor, electrical field displacement and volume charge density respectively. Young's modulus and relative

permittivity of PDMS used in the simulations were 750 kPa and 2.75 respectively and taken from COMSOL materials property library.

ZnO NWs were considered as piezoelectric material and thus, its electrical and mechanical properties were coupled using following equations (3) and (4):

$$T = c_E S - e^t E \tag{5.3}$$

$$D = eS - \epsilon E \tag{5.4}$$

where c_E is the stiffness tensor for constant electric field E, *e* is the piezoelectric coupling tensor in the stress-charge notation, the superscript *t* stands for transpose of the matrix *e* and ϵ is the electric permittivity tensor. The material properties for ZnO NWs taken from the materials library of COMSOL Multiphysics and have shown promising results in previous theoretical works[181, 227] are as follows:

- Stiffness tensor $c_{ij}^E =$

$$\begin{bmatrix} 2.097 & 1.211 & 1.054 & 0 & 0 & 0 \\ 1.211 & 2.097 & 1.054 & 0 & 0 & 0 \\ 1.054 & 1.054 & 2.112 & 0 & 0 & 0 \\ 0 & 0 & 0 & 0.424 & 0 & 0 \\ 0 & 0 & 0 & 0 & 0.424 & 0 \\ 0 & 0 & 0 & 0 & 0 & 0.424 \end{bmatrix} \times 10^{11}$$

- Coupling tensor $e_{ij} =$

$$\begin{bmatrix} 0 & 0 & 0 & 0 & -0.480 & 0 \\ 0 & 0 & 0 & -0.480 & 0 & 0 \\ -0.567 & -0.567 & 1.320 & 0 & 0 & 0 \end{bmatrix}$$

- Relative dielectric permittivity $\varepsilon_{ij}^S =$

$$\begin{bmatrix} 8.545 & 0 & 0 \\ 0 & 8.545 & 0 \\ 0 & 0 & 10.204 \end{bmatrix}$$

- Dielectric losses = 1%

Using the above material properties and geometry specifications as given in Table 1, the

variation in capacitance of each sensor with applied pressure was measured in the range of 0-10 kPa. The relative change in capacitance (5) and sensitivity (S) (6) were also evaluated for each sensor:

$$\%\frac{\Delta C}{C_0} = \frac{(C - C_0)}{C_0} \times 100 \tag{5.5}$$

$$S = \Delta(\%\frac{\Delta C}{C_0})/\Delta P \tag{5.6}$$

where C and C_0 are Maxwell's capacitance of the sensors at any pressure and zero pressure respectively and ΔP is the change in pressure or it can be calculated as slope of the $\%\Delta C/C_0$ vs pressure curve.

5.3. Results and Discussion

5.3.1. Effect of addition of ZnO NWs and their orientation

Figure 5.3 shows the relative change in capacitance, sensitivity and compressive stress-strain for sensors labelled as P, H1 and V1. From Figure 5.3(a), it can be seen that the calculated sensitivity for sensor with bare PDMS (i.e. P) as dielectric is 0.26%kPa^{-1} which lies within the range of previous experimentally measured sensitivity (0.125-0.8%kPa^{-1}) for pristine PDMS based sensors[87, 101]. After the addition of ZnO NWs in the PDMS matrix closer to electrodes, the sensitivity for sensors H1 (i.e., sensor with NWs parallel to the PDMS surface) and V1 (i.e., sensor with NWs perpendicular to the PDMS surface) increased in comparison to sensitivity of sensor P. This shows that addition of ZnO NWs in the PDMS matrix enhances the sensitivity and in-line with previous experimental observations[87, 222, 228]. In Figure 5.3(b) it can be observed that the elastic moduli of sensors H1 and V1 is greater than the elastic modulus of sensor P. In other words, the pressure induced polarization followed by surface charge generation on ZnO NWs could

contribute to the better sensitivity compared to the bare PDMS despite the low displacement in the sensor at a given pressure. This shows that addition of ZnO NWs enhances the compressive strength of the nano-composite material, but it also improves the sensitivity of the sensor. We also observe that the sensor with vertical ZnO NWs (V1) have higher modulus and sensitivity when compared with sensors having horizontal NWs (H1). This shows that the orientation of NWs play can play critical role in performance of the sensors.

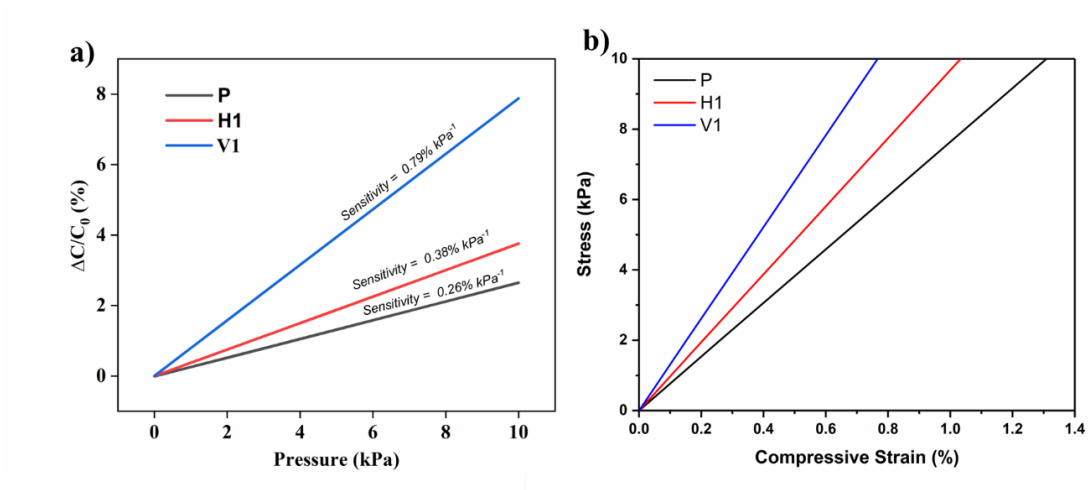

Figure 5.3: Variation in (a)relative change in capacitance and (b) stress-strain graph for sensors P, H1 and V1

5.3.2. Effect of aspect ratio of ZnO NWs on sensitivity and mechanical properties of sensor

Since it was apparent that the sensors with vertical ZnO NWs configuration (H1) have higher sensitivity than other sensors, further simulations for design optimisation of the capacitive sensors were carried out. The aspect ratio of ZnO NWs in configuration 3 varied such that the volume of each ZnO NW in all the sensors remain same as tabulated previously in Table 1. The extracted sensitivity through the change in capacitance value and stress-strain curves for sensors V1-V5 having ZnO NWs with different aspect ratio is presented in Figure 5.4(a-c). As seen from Figure 5.4(a-b), the increase in NWs aspect ratio leads to increment in sensitivity of sensors. Interestingly, the sensitivity of these

sensors shows a linear relation with the aspect ratio of ZnO NWs. The highest sensitivity (1.17% kPa^{-1}) is displayed by the NWs with the highest aspect ratio of 92. For all the sensors V1-V5, sensitivity is 1.8-4.5 times higher than the sensitivity of sensor P (pristine PDMS based sensor) and it's in the same order when compared with previous experimental results where an increase by 2-7 times was observed[87]. While observing the stress-strain curves for different sensors from Figure 5.4(c), increase in elastic modulus of sensors with increase in aspect ratio of ZnO NWs was seen. In general, polymer nanocomposites show increment elastic modulus with respect to aspect ratio of nanofillers which was observed in the previous reports [229-231]. However, with increasing elastic modulus the deformation in the sensor at a particular pressure decreases and thus the change in capacitance of the sensors due to change in the distance between the electrodes should reduce but opposite results were observed in this work. Thus, it seems that the piezoelectric properties of ZnO NWs play critical role in enhancement of sensitivity of these sensors[87].

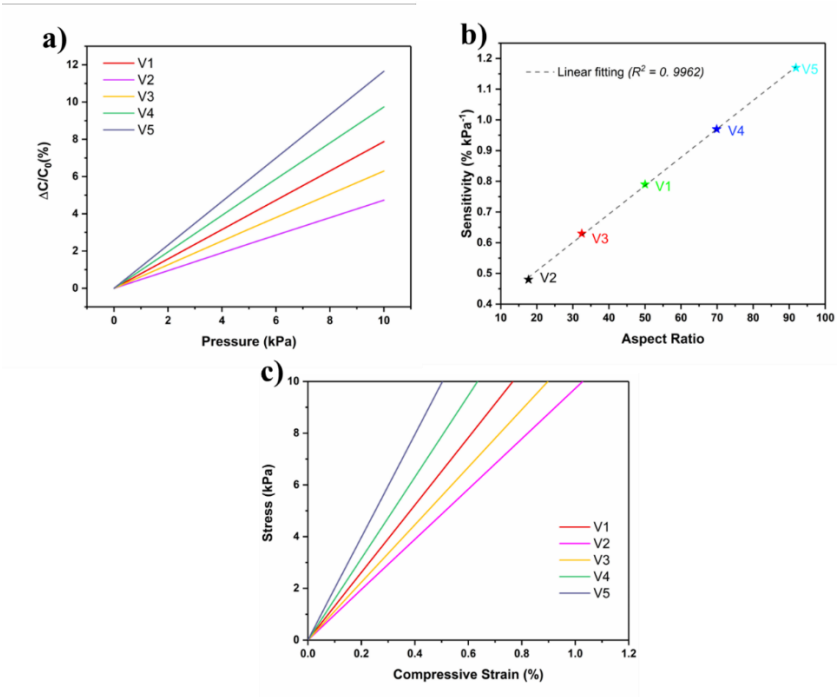

Figure 5.4: Effect of aspect ratio of ZNO NWs on (a)relative change in capacitance, (b)sensitivity and (c)stress-strain graph of sensors

5.3.3. Piezoelectric effect of embedded ZnO NWs on sensitivity

To further illustrate the effect of piezoelectric effect of ZnO NWs on the sensitivity, focused set of simulations were carried out in which the piezoelectric module of COMSOL® Multiphysics was disabled and the change in capacitance is observed due to change in interspacing between the electrodes. Figure 5.5 shows the relative change in capacitance when the piezoelectric effect for ZnO NWs is disabled and then it is compared with the sensitivity values obtained before when the piezoelectric effect was enabled. From Figure 5.5(a), the maximum change in relative capacitance is much lower in the pressure range of 0-10 kPa when compared with those in Figure 5.3(a) and Figure 5.4(a). Figure 5.5(b) compares the sensitivity with and without piezoelectric effect of ZnO NWs and reduction in sensitivity of all the sensors was observed in the absence of piezoelectric effect in ZnO NWs. Also, we observed that for all the sensors in configuration 3, with increasing aspect ratio the sensitivity of these sensors decreases when piezoelectric effect was disabled. This happens because of the increase in elastic modulus of the sensors with increasing aspect ratio as observed in Figure 5.4(c) and thus there is lower change in interspacing between the electrodes and hence lower change in capacitance. It can be also inferred from Figure 5.5(b) that with increasing aspect ratio there is larger contribution of piezoelectric effect towards the sensitivity of sensors, and it dominates over other mechanical effects in greater way. The reason behind increase in piezoelectric effect in higher aspect ratio ZnO NWs is reported in next sub-section.

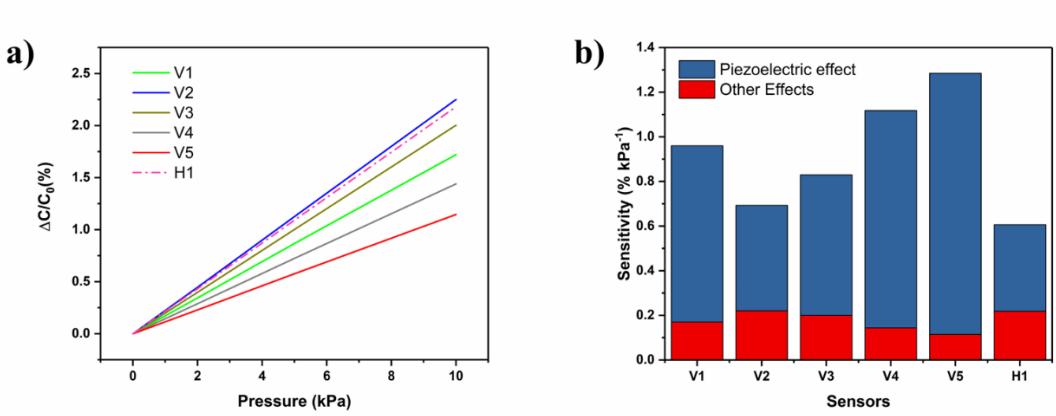

Figure 5.5: a) Relative change in capacitance when piezoelectric module was disabled and (b)comparison of sensitivity with and without piezoelectric effect in ZnO NWs. Here the other effects include dielectric and mechanical effects of ZnO

5.3.4. Evaluation of piezoelectric polarization in ZnO NWs

The current work is also attempted to analyse the magnitude of piezoelectric polarisation of embedded ZnO NWs in different sensor configurations due to strain caused by the external pressure. Figure 5.6(a-b) shows the schematic of piezoelectric polarisation in ZnO NWs embedded inside the sensors in horizontal and vertical orientations and Figure 5.6(c-d) depicts the magnitude of average strain and piezoelectric polarisation in each NW at different pressures in all the sensors. From Figure 5.6(c-d), it can be inferred that there is residual strain in NWs which lead to piezoelectric polarisation even at no load condition in all the sensors. This happens due to difference in the elastic modulii of PDMS and ZnO NWs. This creates stress at the NWs/PDMS interface and eventually the bulk of each NW experiences compression along horizontal and tensile stress in the longitudinal axis. However, the ability to withstand load varies with the increment of aspect ratio in the sub-500 nm diameter range and when pressure is applied, the strain increases linearly with pressure which leads to linear increase in piezoelectric polarisation in ZnO NWs. The order of magnitude of strain and piezoelectric polarisation in different sensors is V5>V4>V1>V3>V2>H1 and same order in sensitivity was also observed in Figure 5.5(b). This shows that the sensitivity of these sensors is directly proportional to the magnitude of piezoelectric polarisation in the ZnO NWs. We observe higher strain and

piezoelectric polarisation in ZnO NWs with higher aspect ratio because they show higher tendency to bend which has also been reported in previous studies[117, 232]. The bendability of the ZnO NWs embedded in PDMS matrix enhances the Zn^{2+} and O^{2-} charge separation which leads to the increases change in capacitance reflected in the observed sensitivity.

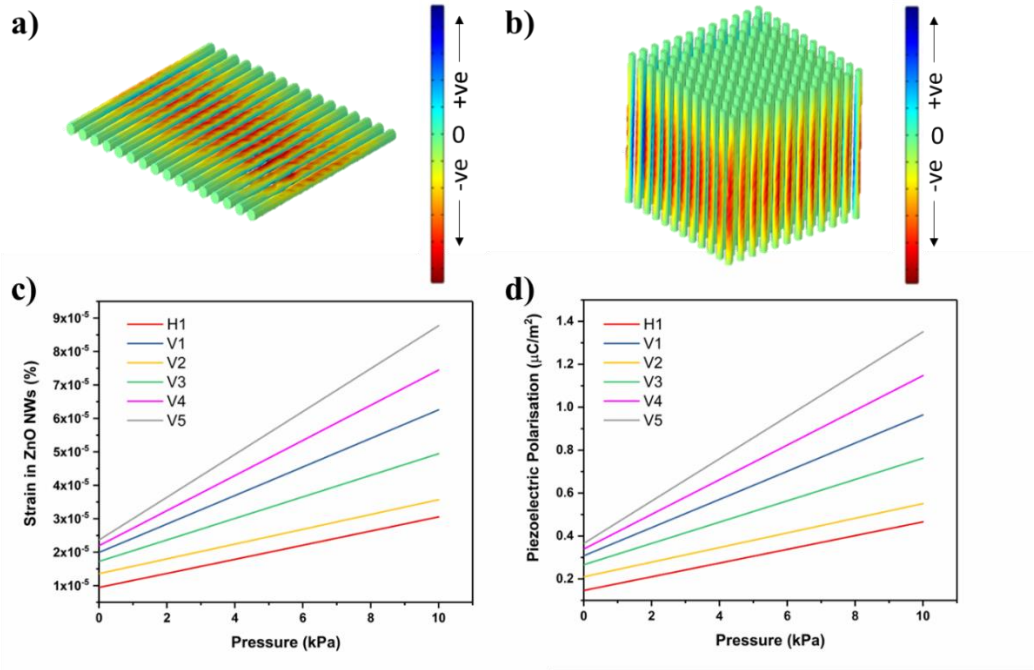

Figure 5.6: Schematic of piezoelectric polarization in sensors (a) H1 and (b) V1 and for better clarity and visualization, the PDMS block has been omitted. The graphs for change in (c)strain and (d) piezoelectric polarization in ZnO NWs at different pressure in different sensors is also presented.

5.4. Conclusion

In this chapter, FEM simulations were carried out to study the effect of the addition of piezoelectric ZnO NWs, their orientation and dimensions on the relative change in capacitance, sensitivity and mechanical properties of soft capacitive sensors using PDMS as dielectric material. The addition of ZnO NWs increases the relative change in capacitance, sensitivity and elastic modulus of the sensors when compared with sensors having pristine PDMS structure. Additionally, it was shown that on application of pressure, the vertical ZnO NWs based sensors have higher sensitivity than its lateral ZnO NWs based sensors at constant volume fraction of ZnO NWs. The variation in sensitivity

and mechanical properties of the sensors with aspect ratio of ZnO NWs was also explored. It showed that at same volume fraction, higher aspect ratio ZnO NWs show better sensitivity although the elasticity of these sensors decreases with increasing aspect ratio of NWs. It was also shown that the piezoelectric properties of ZnO NWs play a dominant role in enhancement in sensitivity of the sensors. The average magnitude of strain and piezoelectric polarisation in ZnO NWs were analysed and it was inferred that both strain and piezoelectric polarisation increases with their aspect ratio and thus increasing the sensitivity of these sensors. These observations were validated with previously reported experimental values and trends. The effect of other parameters such as dimension of PDMS layer, NW density, etc. as well sensors with mixed orientation, random and interconnected NWs can be further explored in future studies. Overall, the simulation studies presented in this chapter will help in designing and optimising performance of flexible capacitive pressure and other sensors that can be employed in the field of flexible and reliable tactile skins for robotics application.

Chapter 6

Molecular Dynamics Study of Water Trapping and Its Impact on Graphene-Gold Interfacial Properties

This work is adopted from:

Journal Article:

- **Mishra, S.,** Liu, F., Shakthivel, D., Rai,B., Georgiev, V., Molecular Dynamics Simulation based Study to Analyse the Properties of Entrapped Water Between Gold and Graphene 2D Interface, *Nanoscale Advances*, 6, 2371-2379 (2024)

Abstract

The heterostructures based on graphene and other 2D materials have received significant attention in recent years. However, it is challenging to fabricate them with ultra-clean interface due to unwanted foreign molecules, which usually get introduced during their transfer to a desired substrate. The clean nanofabrication is critical to the utilization of these materials in 2D nanoelectronics device and circuits and therefore, it important to understand the influence of "non-ideal" interface. Inspired by the wet-transfer process of CVD grown graphene, herein we present an atomistic simulation of graphene-Au interface, where water molecules often get trapped during transfer process. By using

molecular dynamics (MD) simulation, we investigated the structural variation of trapped water, and the traction-separation curve derived from the graphene-Au interface at 300K. We observe the formation of ice-like structure with square-ice patterns when thickness of water film is < 5Å. This could cause undesirable strain in the graphene layer and hence affect the performance of devices developed from it. We also observed that at higher thickness the water film is predominantly present in liquid state. The traction separation curve showed that the adhesion of graphene is better in the presence of ice-like structure. This study explains the behaviour of water confined at the nanoscale region and advances our understanding about graphene-Au interface in 2D nanoelectronics device and circuits.

6.1. Introduction

The graphene and other 2D materials have received significant attention in recent years as their excellent electrical, optical and mechanical properties are attractive for various types of sensors, energy and electronics devices needed in application such as wearables, electronic skin, robotics, and transparent electronics etc [233-236]. In particular, the Van der Waals (vdW) heterostructure based on 2D materials have opened new opportunities for electronic devices with exceptional electronic and structural properties[237-241]. Specifically, the large-scale fabrication and synthesis of 2D materials using CVD method and their transfer onto foreign substrate have been extensively studied in the past two decades, leading to various novel devices such as field effect transistors, photodetection, microelectromechanical systems (MEMS) and flexible sensors [240, 242, 243]. However, the realised large-scale vdW structures using CVD grown material are normally non-ideal as they come with unintended foreign species (e.g., water) trapped at the interface. These foreign species could have considerable impact on the uniformity of device response and hence on the large-scale implementation. Therefore, it is important to understand the widely observed non-ideal interface properties.

Various transfer mediums, including water, alcohol, isopropanol, heptane, etc, have been used to assist the wet transfer of 2D materials owing to the capillary force[16, 179, 244-249]. Among them, water is employed in all the fabrication stages (transfer, patterning and metallization) as medium and therefore, understanding the graphene-metal (Au) structure with trapped water has a profound meaning both for research and applications. For example, the graphene-Au interface has considerable influence over the performance of Graphene based Field Effect Transistors (GFETs) as it defines the contact resistance and hence the efficient charge transfer. Previous studies suggest that water clusters ranging 0.3-0.5 nm in height and 10-40 nm in width can be found between gold (111) electrode and graphene[250]. The trapped water cluster could alter the electronic properties of the graphene as well as the device by inducing strong and highly localised electron doping[250-252]. Additionally, interface with Au is relevant for many other 2D materials. As an example, in the last years, mechanical exfoliation of transition metal dichalcogenides (TMDs) and other 2D materials on the gold surfaces has been investigated by several research groups, and the method proved to be effective to achieve the exfoliation of large are membranes, by exploiting the interaction with Au, as in the case of MoS_2[253-256]. Interestingly, a certain variability in the morphological, vibrational and optical properties of exfoliated TMDs has been found by different authors, and this was ascribed to the differences in the gold surface morphology and the presence of hydrocarbon contaminants at the interface. The role played by trapped water at the 2D materials/Au interface on the interaction strength has not been discussed so far. The presence of entrapped water molecules could also alter the adhesion energy[247], which plays a crucial role in the fabrication and integration of graphene-based devices[16].

The confined water at nanometre scale exhibit anomalous phase behaviour[257, 258] and because of the restricted molecular degrees of freedom, hydrogen bonding and high

pressure in nanoconfinement, many unusual structural features have been observed [259, 260]. For example, multi-layered two-dimensional ice have been found even at room temperature and high-pressure condition[261]. Square ice, a rare form of ice, has been observed experimentally between graphene sheets even at ambient conditions[262]. The formation of square ice indicates ~1 GPa pressure within the confined space. Nanoconfined water has potential applications in molecular electronics as a nanoscale switch[257], capacitive sensing[263], and in desalination process[264]. These observations have led researchers to use computational techniques such as density functional theory (DFT) and molecular dynamics (MD) simulations to understand and analyse the properties of water under nanoconfinement conditions[258-260, 262, 265, 266]. However, most of these studies are limited to confinement between carbon-based nanostructures such as graphene and carbon nanotubes. Likewise, these simulation techniques have been separately used to study the adhesion and friction between the graphene and gold substrate for ambient dry conditions [249, 267-272]. However, these studies do not consider the role of adsorbed water molecules on the adhesion properties of graphene over the metallic substrate which has implications on the performance GFETs. It is important to study the effect of confined water molecules on the gold-graphene adhesion together as different phases of water in a nanoconfined region face the hydrophobic (graphene) and hydrophilic (gold) surfaces at same time.

In this study, we use MD simulations to investigate the structure of water confined between gold and graphene at sub-nanometer length scale. Range of water cluster sizes (~1200-3200 molecules) studied here correspond to the experimentally observed cluster size at the graphene/Au interface. Different phases of water structure were predicted by varying the thickness of water film in the simulations. The displayed phase changes (liquid to disordered with square-ice like pattern) were sensitive to the narrow difference

in water cluster sizes. The traction-separation properties between graphene and gold were also investigated in the presence of adsorbed confined water clusters to understand the variation in adhesion behaviour at different thickness of water films. We observed the formation of ice-like structure with square-ice patterns when thickness of water film is < 5Å. This could cause undesirable strain in the graphene layer and hence affect the performance of devices developed from it. We also observed that at higher thickness the water film is predominantly present in liquid state. This study will help to develop a better understanding of the effect of aqueous nanofabrication conditions on the properties of nano-scale devices especially the ones involving wet-transferred graphene.

6.2. Simulation Methodology

A simulation box of size 10nm x10nm x50nm was used for all the simulations presented in this work. It consisted of 2.5 nm thick Au (111) ([111] being the z-direction) substrate at the bottom of the box in which few of the bottom layers (0.6 nm thick) were kept fixed while others were free to move. A graphene sheet of size 10 nm x 10 nm was placed over this gold substrate. Water molecules were added between the gold and graphene using PACKMOL[273]. Periodic boundary conditions were applied in all the dimensions. A vacuum was kept in z-direction above the graphene layer to avoid any interaction with its periodic image.

The Au(111) substrate was modelled using the Embedded Atom Method (EAM) forcefield parameters[274, 275] while Adaptive Intermolecular Reactive empirical Bond Order (AIREBO)[276] parameters were used for graphene layer. The SPC/E forcefield parameters[277] were used to model the water molecules. The charges on gold and graphene atoms were taken as zero while for O and H atoms of water molecules the charges were -0.8476e and 0.4238e respectively. The interaction between gold and

graphene, graphene-water and gold-water was modelled using the 6,12 LJ potential with equation (1) and these parameters are given in Table 6.1.

$$V(r) = 4\epsilon\left\{\left(\frac{\sigma}{r}\right)^{12} - \left(\frac{\sigma}{r}\right)^{6}\right\} \tag{6.1}$$

Table 6.1: LJ potential coefficients used for various pair of atoms used in the simulations (denotes any atom type out of Au, C, O and H)*

Atom Pairs	ε (meV)	σ (Å)
Au - C	8	3.42
Au – O	25.5	3.6
C - O	6.74	3.17
O - O	4.06	3.19
H - *	0	0

To measure the equilibrium distance between the Au (111) and graphene, similar box was used withouth water molecules. This box was subjected to energy minimisation at 0K followed by NVT ensemble equilibration at 300K for 500 ps.

The simulation box with confined water molecules were also energy minimised and then equilibrated using NVT ensmeble at 300K for 500 ps. Water structures formed during last 50 ps were used at every 1 ps and analysed to get the average lateral O-O radial distribution and O-O-O angle distribution curves. Later, the equilibrated systems were used to get the traction-separation curves.

During the separation process, the sides of the graphene sheet were clamped and a series of displacement of 0.5 Å was applied stepwise in positive z direction to these clamped graphene atoms. Between every step of displacment of atoms, a relaxation process was applied in NVT ensemble for 100 ps. At each separation displacement, total interaction

force on graphene due to all other atoms (Au, O and H atoms) were computed using the following function:

$$\sigma\,(d) = \frac{\langle F(d)\rangle_t}{A} \tag{6.2}$$

where A is the area of undeformed graphene sheet, d is the applied displacement on graphene atoms and $\langle F(d)\rangle_t$ is time averaged total force on graphene sheet as a function of d. Similar method and equation were used succesfully by Gao[247] to obtain the traction-separation curve for silica-water-graphene system.

Lateral MSD for water in direction parallel to the surface of graphene sheet was calculated and using it, self diffusion coefficient, D_{self} for water molecules was also calculated by using following equation[278]:

$$D_{self} = \lim_{t\to\infty} \frac{1}{2t} \langle \frac{1}{2} \sum_{i=x,y} [r^i(t) - r^i(0)]^2 \rangle \tag{6.3}$$

where t is time, $r^i(t)$ refers to position of an atom at time t and $r^i(0)$ refers to its initial position.

All simulations were run in LAMMPS[205] simulation package. The timestep used for entire simulation was 1 fs. OVITO[279] visualisation software was used to analyse the simulations.

6.3. Results and Discussion

In the MD simulations, the interaction between C atoms of graphene and Au atoms of gold substrate were modelled using 6,12 Lennard-Jones (LJ) interactions with parameters σ = 3.42 Å and ε = 8 meV which have been used previously [268]. With these parameters, and after energy minimization at 0 K, the equilibrium distance (d_{equi}) and binding energy between gold and graphene were found to be 3.36 Å and 60.7 meV/C atoms, respectively

(Figure 1). When compared with previous DFT studies wherein different pseudopotentials were used to compute d_{equi} and binding energy in the range of 3.22-3.52 Å and 30-72 meV/C atoms, respectively), the LJ parameters used in this simulation are consistent with the predictions for these two parameters[271, 272]. This validates the LJ potential parameters used here for C and Au atoms. After energy minimisation at 0K, the above gold-graphene system was subjected to equilibration in canonical (NVT) ensemble at 300 K. The distance d_{equi} increased marginally to 3.42 Å due to thermal effect on the atoms.

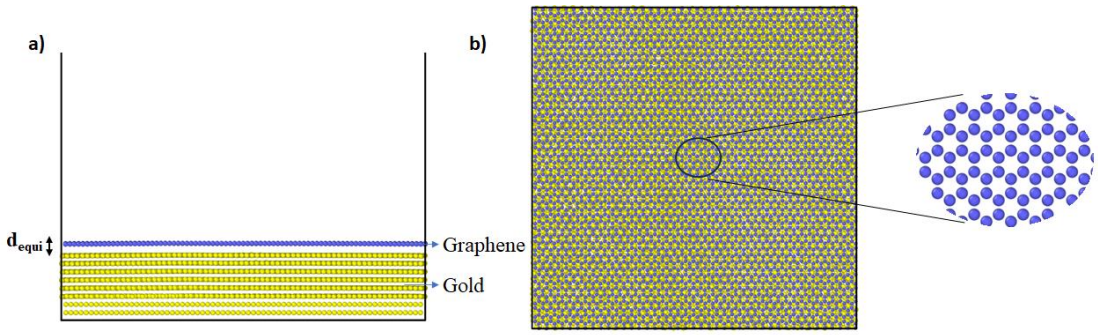

Figure 6.1: (a) Side and (b) top view of the simulated gold-graphene system with magnified view of graphene atoms

To study the effect of water, confined at gold – graphene interface, on d_{equi} and their structural properties, we considered three different scenarioss with varying number of water molecules (Table 1). The distances, d_{equi} and $d_{thick,}$ (average thickness of water film) for all these 3 scenarios (after NVT equilibration at 300K) are given in Table 1. It can be observed that d_{equi} and $d_{thick,}$ increases with increasing the number of water molecules. The predicted range of d_{thick} lies within 3.5 – 9.21 Å i.e., within 1 nm range which is also generally found in the experimental conditions[250]. The effect of varying thickness with number of water molecules on the structural properties of confined water between gold and graphene as well the effect on traction-separation properties of graphene has been discussed in below.

Table 6.2: Number of water molecules, the equilibrium distance between gold and graphene, and the thickness of water film

Scenario	Number of water molecules	Avg. equilibrium distance between gold and graphene, d_{equi} (Å)	Avg. thickness of water film, d_{thick} (Å)
A	1200	6.92	3.50
B	1623	8.06	4.64
C	3139	12.63	9.21

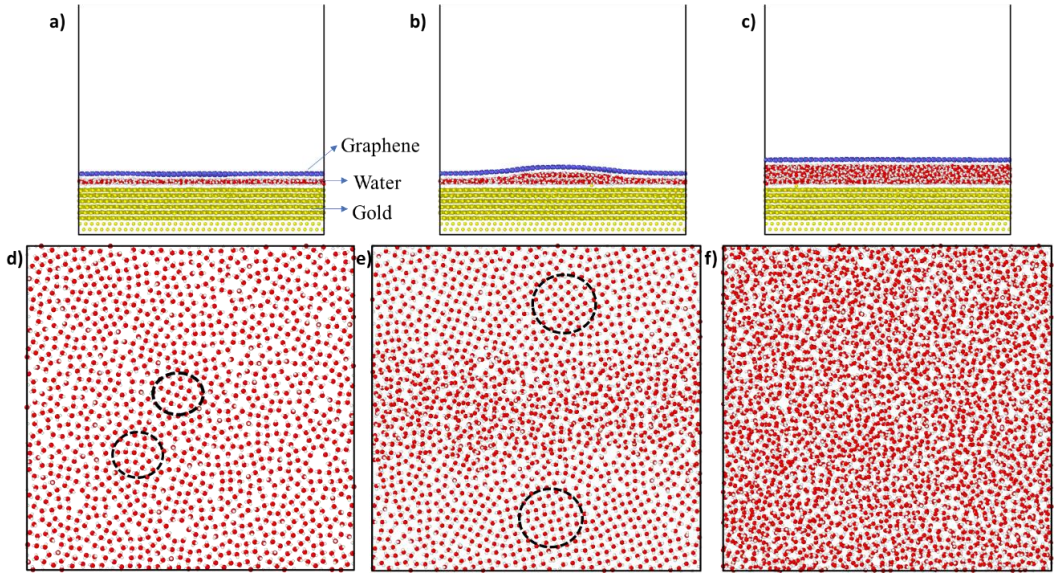

Figure 6.2: (a), (b),(c) are the side view snapshots for scenarios A, B and C respectively after NVT equilibration. (d), (e) and (f) depict the structure of water viewed from top in each of the scenarios after equilibration. The black dotted circles in (d) and (e) show the square-ice like patterns in the water structures. In all the figures, the red and white atoms correspond to O and H atoms of the water molecule while blue and yellow atoms correspond to the C and Au atoms of graphene and gold respectively.

Figure 6.2 shows the snapshots of the gold-water-graphene for three scenarios as well as the MD simulated structure of the water molecules after the NVT equilibration for each of these scenarios. In the scenario A (Figure 6.2(a)), which has the least number of water molecules, we observed the formation of a monolayer water film of 3.50 Å thickness (Table1) with patches of ice-like structure (Figure 1d). The thickness of this monolayer water film is similar to the thickness of the ice-like monolayer water film (3.7±0.2 Å) formed between graphene-graphene and graphene-mica confined surfaces[280, 281]. While in the case of scenario B, we observe a monolayer water film near the edges and a bilayer structure at the centre, potentially inducing a wrinkle in the graphene sheet

(Figures 6.2(b,d)).[257, 266, 282] Such wrinkles in graphene have also been found in previous experimental studies[283, 284], and therefore observed results confirm that the efficacy of presented simulations. In the case of scenario C, we observed a completely amorphous water film with higher thickness between gold and graphene, as seen in Figures 6.2(c,f). Unlike scenario B, in this case graphene has a planar structure.

Further analysis of the structure of water film in scenario A revealed a disordered structure with square ice like pattern at some regions (in black dotted circles) as well as some pentagonal and hexagonal rings of oxygen atoms (as shown in Figure 2d). In scenario B, the bilayer structure of water was sliced into two parts: bottom layer and upper layer as seen in Figure 6.3. In the bottom layer, the monolayer water film near the edges has ice-like structure. However, the ice structure is observed here is more ordered near the edges (having square ice like pattern) when compared to the structure in centre or middle of the box. In upper layer too, the structure is mostly disordered with some regions of square-ice like patterns. In the scenario C, the structure of water appeared to be disordered or amorphous. A layered structure (monolayer, bilayer or even trilayer) of water is typically observed when it is confined between two hydrophobic materials (i.e., two graphene sheets), it exhibits [257, 266, 282]. However, in this study, the water is confined between a strong hydrophobic surface (i.e., graphene) and a weakly hydrophilic surface (i.e., gold) and thus, at sub-nanometer thickness, the confined water transforms from layered ordered ice-like structure (thickness<= 5Å) to amorphous structure (thickness >5Å). Similar, transition from ice-like structure to liquid structure was observed for water confined between graphene (hydrophobic) and mica (hydrophilic) surfaces[281].

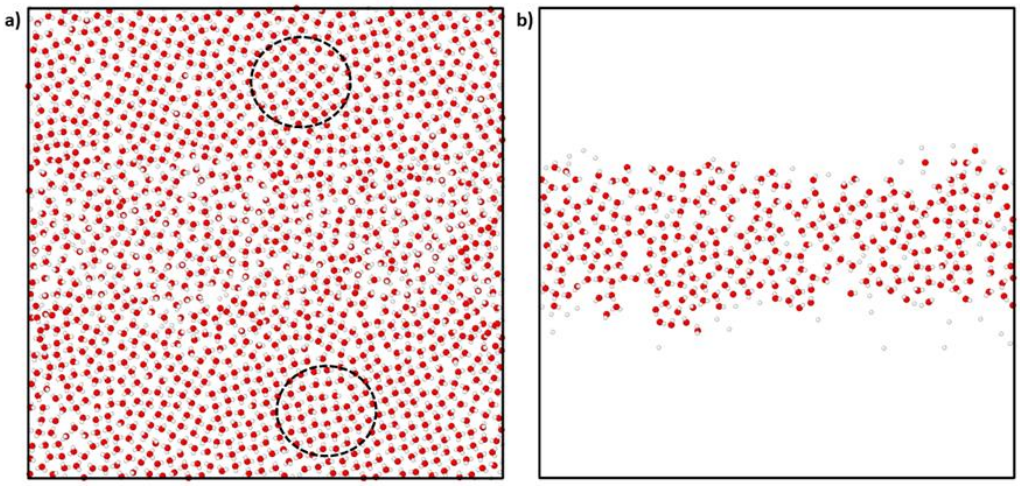

Figure 6.3: Top view of the snapshots of (a) bottom layer and (b) top layer seen from top in the case of scenario B after equilibration. The black dashed circles show the presence of square ice pattern in these water structures.

To further validate the presence of ice-like structure in scenarios A and B and amorphous structure in scenario C, the radial distribution curve between O-O atoms and angle distribution between O-O-O atoms were plotted, as shown in Figure 3. From Figure 3(a-b), we observed peaks in radial distribution curve at distances around 2.8 Å, 5.6 Å and 8.4 Å. The angle distribution curve exhibits two peaks, one broad peak around 90°-110° and another around 160° in the case of scenarios A and B. These are the characteristics of square-ice like structure, as observed in previous studies[266, 282]. However, in the case of scenario C, the radial distribution curve and angle distribution curve showed single peaks, which indicates the presence of liquid water. The water present in this case has the typical tetragonal structure with peak around 104° in the angle distribution curve[266, 282]. Lateral mean-square displacement (MSD) of water molecules were also obtained for all the scenarios, as shown in Fig. 3(c). The figure shows that the water molecules in the scenario C are more mobile when compared to other scenarios - thus indicating the higher proportion of liquid phase the former. The lateral self-diffusion, parallel to the surface of graphene sheet, for water molecules was obtained from these curves and

compared with the self-diffusion coefficient of bulk liquid water at 300K (from previous studies) as depicted in Fig. 3(d). The observed self-diffusion coefficient in scenarios A and B are much lower than the one for bulk liquid water (0.21 $Å^2$/ps)[278] and for scenarios C it is nearly equal (0.22 $Å^2$/ps). These observations indicate that in the case of scenario C, the water is present in liquid state while in other two scenarios some ice-like structure is also present. Although both A and B structure contains ice-like properties, the self-diffusion coefficient in scenario B is lower. This is due to higher capillary forces experienced in A, where the thickness of water film is lower than in scenario B. This is in agreement with observations made by Ghorbanfekr *et al[278]* where they showed that diffusivity of water molecules increases when the thickness of water film confined between hexagonal boron nitride nanocapillaries is reduced below 1nm and it increases to the level of bulk liquid after increasing the thickness above 1nm.

Typically, ice is found to possess hexagonal structure[257, 258]. However, in recent times, square ice like structure has been found both experimentally and theoretically, even at elevated temperature, for water confined between two hydrophobic surfaces like in graphene slits or bilayers [257, 262, 282]. The driving force for formation of square-ice like structure is the high lateral pressure (generally > 1GPa for monolayer water film) created by the interaction forces between confining surface and water atoms which leads to enhanced hydrogen bonding within the water molecules[285]. The lateral pressure on water molecules was also calculated in all the scenarios, as shown in Fig. 3(e). It can be observed that lateral pressure in water molecules is greater than 1GPa in all the cases. The lateral pressure in scenarios A and B is around 1.4 GPa and 1.7GPa which is sufficient for evolution of square-ice like patterns in water molecules at 300K, in accordance with the phase diagram of monolayer water film proposed by Kapil *et al[285]*. In these cases, because of higher lateral pressure values, we observe patches of square ice in very thin

film of water even when one of the surfaces is weakly hydrophilic (e.g., gold) as in scenario A and B. However, the formation of ice or square ice is limited to very thin film of water. At higher thickness of water film, much higher lateral pressure is needed to reach ice like phases as observed in the case of scenario C, where we do not observe ice like structure even if the lateral pressure is higher, i.e. 1.8 GPa[286].

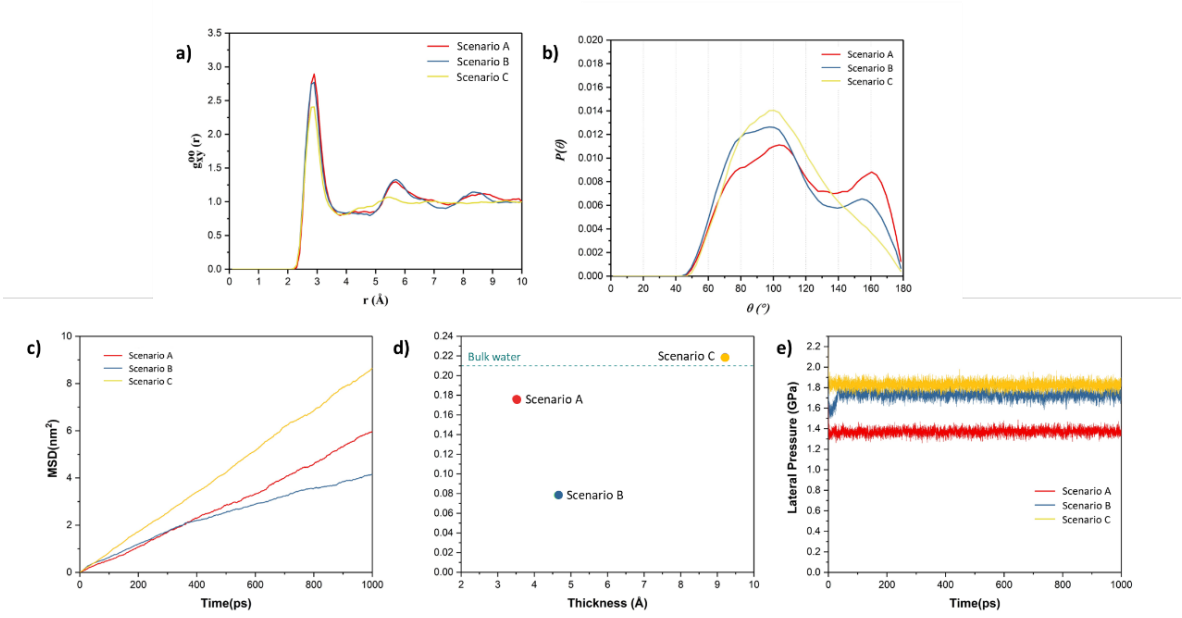

Figure 6.4: (a) Lateral O-O radial distribution function and (b) O-O-O angle distribution curve in water after NVT equilibration in each of the scenarios A, B and C; (c) Lateral MSD with time curve, (d) self-diffusion coefficient versus thickness of water films, (e) lateral pressure in the direction parallel to the surface of graphene sheet versus time.

Having established that variation of the phases of water with thickness in the nanoconfined region between gold and graphene, the next is to study their effect on adhesion strength of graphene and gold interface. To study this aspect, we clamped few carbon atoms of the graphene sheet along the edges in y-direction and these were pulled in z-direction as shown in Fig. 4(a). Then the total interaction force on graphene due to all other atoms was calculated at different separation/displacement in z-direction of graphene sheet from its initial position, as discussed in the Simulation Methodology section below. Figure 4(b) shows the calculated traction-separation graph for the three

scenarios. A gradual increase in the traction stress in noted in both A and B scenarios until the displacements of less than 5Å. For further displacement, we noted a steep fall in the stress and the stress declining to zero for displacement around 8-9 Å. The steep fall in the traction stress is a characteristic of traction stress profile obtained while pulling graphene away from ice as observed in a previous study[287]. This further proves the existence of ice-like structure in the scenarios A and B. We also observed a small peak around 2 Å in scenario B, after which the stress decreased and then again increased with further displacement, possibly due to the movement of wrinkles in graphene from the centre of the box to the edge of the box as explained later. The traction-separation profile for scenario C was found to be similar to the traction separation curve when graphene is pulled away from liquid water, as observed in a previous study[247]. In this case, the stress increases until the displacement of 2.5 Å, after which it decreases exponentially. The reason behind sudden fall in traction stress in scenarios A and B and slow gradual fall in the case of scenario C is the sudden detachment of graphene sheet from the water film in A and B (somewhere between displacement of 5 Å and 6 Å) and the slow detachment of graphene and adherence to the liquid water in some regions in the case of scenario C (until a displacement of 22 Å) as shown in supporting video V1. Interestingly, it can be also observed from this figure that the presence of ice structure in scenarios A and B, lead to short ranged (less than 1.5 nm) interaction between gold and graphene. On other hand, in scenario C, the interaction is long ranged (more than 3nm) due to presence of liquid water. It is also evident from this graph that the maximum traction stress required to pull the graphene sheet is higher in A and B when compared with C, which means the adhesion strength of graphene sheet with ice-like water structure and gold substrate is higher than in comparison to scenario when liquid water is present between gold and graphene.

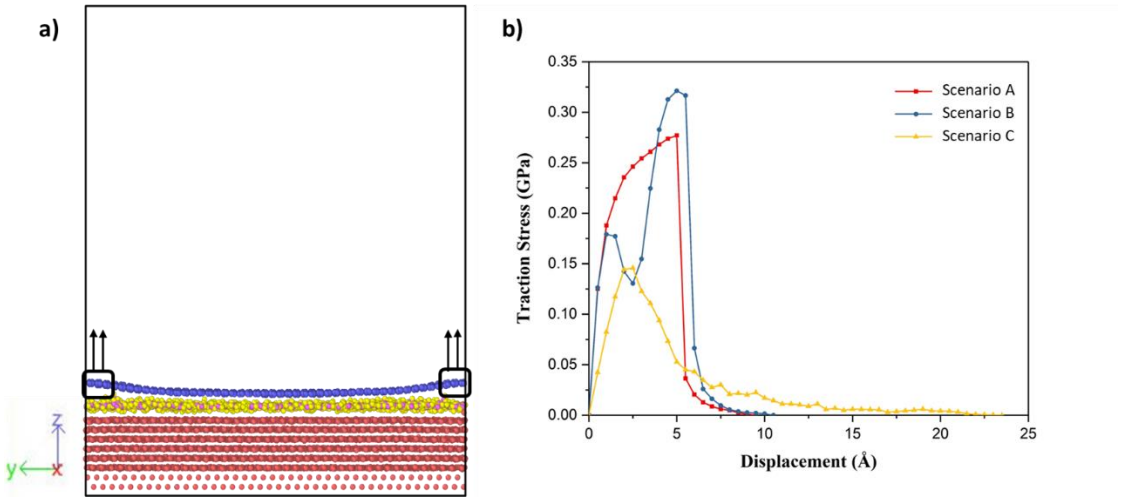

Figure 6.5: (a) Schematic of traction-separation process during simulations, (b) Calculated traction-separation curve for each of the scenarios.

The variations in local structure of water molecules during the traction separation process can explain the detachment mechanism of graphene from the water-gold interface. To this end, we observed the morphology evolution in water film during traction separation process in all the scenarios, as shown in Figure 5. This figure shows the 3×3 periodic replication snapshots after equilibrium and during traction process of water film trapped between gold and graphene with colour coding according to the height contour of the water molecules. From Figure 5 (a-c), it can be observed that in the case of scenario A the new cavities are formed in the water film during traction process. The size of these cavities increased with traction until 5Å and got stabilised after this separation distance. This means there was no adhesion between graphene sheet and water beyond this separation and thus, we a steep fall in traction separation curve was observed at this separation distance in the case of scenario A, as shown in Fig. 4(b). In the case of scenario B, from Figure 5(d-f), no pores or cavities were observed, and the capillary bridges (red coloured patches), formed due to bilayer water structure, were seen after equilibration process. During the traction separation process, these capillary bridges move from centre towards the edge of the box and a slight change in height of these bridges was noticed. After a separation of 5-6Å, the heights of capillary bridge got stabilised, which again

shows that there was no interaction between graphene and water beyond this separation distance. Thus, a steep decline in the traction separation graph in the scenario B is explained as well. In the case of C, initially, there is a smooth water film found between gold and graphene after equilibration observed in Figure 5(g). During traction-separation process, the capillary bridges were formed initially at lower displacements which broke into conical structure at higher displacements, as observed from Figure 5(h-m). The transformation of uniform water film from capillary bridge to conical structure due to presence of liquid water was also found in previous theoretical work[247] on traction-separation process of graphene over a wet-silica substrate. This shows the long-range interaction between gold and liquid water until a separation of 15Å in the case of scenario C. From above, it is evident that the morphologies of entrapped water film, with different heights and phases, during traction-separation process are not similar. Instead, they are quite different in nature.

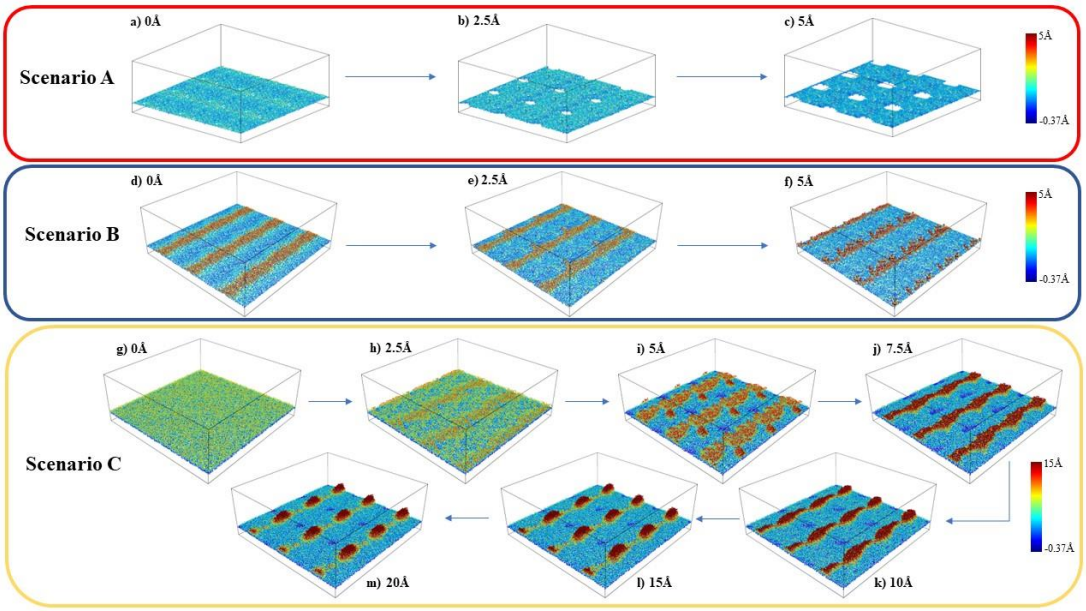

Figure 6.6: Snapshots of water molecules (3×3 periodic replication) from MD simulations during traction-separation process (atoms of gold and graphene are omitted for better understanding) with colour coding reflecting the height in z-direction.

6.4. Conclusion

Molecular dynamics simulations employed to study the structure and traction-separation properties of entrapped confined water molecules between gold and graphene suggest the presence of ice like structure in thinner water films (<5Å) and liquid water structure at higher thickness of water films. This work also predicts the formation of patches of square-ice like structure between a hydrophobic and a hydrophilic surface at very low separation (<5Å). Due to presence of different phases of water, the traction separation study highlights the differences in adhesion strength of graphene with the heights of water film. The varying structures of water could lead to different band gaps[288] and hence, the structure of water nanoconfined in the nanoregions between gold and graphene could influence the electronic properties of graphene devices such as GFETs. This will be studied in a future work with fabrication of GFETs. The results presented in this work are expected to help experimentalists to understand the influence of microscopic picture of water films confined in wet-transferred graphene device.

Chapter 7

Summary and Future Work

7.1 Summary

The human tactile perception mechanism involves skin mechanoreceptors that detect pressure, texture, vibration and other cues sending signals to the brain for interpretation. Biomimicking this process in tactile sensors could greatly enhance the sensitivity and functionality of robotics, prosthetics, and human-computer interfaces by replicating the natural sense of touch.

Flexible tactile sensors have emerged as a crucial technology in the development of advanced human-computer interfaces, robotics, and prosthetics. These sensors, often composed of soft, stretchable materials (as mentioned in Chapter 2), are designed to mimic the human sense of touch, enabling devices to detect pressure, strain, temperature, and other mechanical stimuli with high sensitivity and precision. In human-computer interfaces, flexible tactile sensors are employed to create more intuitive and natural user experiences, such as touch-sensitive screens or wearable devices that respond to physical gestures. In robotics, these sensors enhance the ability of machines to interact with their environment, allowing robots to grasp objects delicately, adjust grip strength, and perform complex tasks requiring precision handling. In the field of prosthetics, flexible tactile sensors play a vital role in developing artificial limbs with enhanced sensory feedback, enabling users to "feel" sensations like pressure and texture, thus improving their

interaction with the physical world. This integration of tactile sensors into various systems is driving innovation in creating more responsive and human-like robotic systems and assistive devices.

Through the research work presented in this thesis, I have tried to advance the field of flexible tactile sensors and following were the main outcomes from this research:

- Various soft stretchable strain sensors were developed by combining Ecoflex elastomer, conductive filler (CNT, graphite), and GCP including sensors with an unprecedented gauge factor of 1,834,140 in Chapter 3. Later, these sensors were used to develop neuromorphic systems that can generate spiking signals by attaching it to a wheatstone bridge and a simulated LIF neuron.
- In Chapter 4, a novel hybrid pressure sensing system was created by stacking triboelectric and capacitive pressure sensors, enabling the detection of both static and dynamic pressure stimuli simultaneously. This system was later employed to detect hardness assessment, slip and vibration motions successfully.
- Furthermore, theoretical studies, presented in Chapter 5, on incorporating ZnO nanowires (NWs) into PDMS-based pressure sensors using FEM simulations demonstrated that the addition of ZnO NWs enhanced sensitivity by approximately three times. It also showed the importance of piezoelectric properties of ZnO NWs in the sensistivity of the capacitive sensors.
- Lastly, atomistic simulations presented in Chapter 6 revealed that trapped water molecules at the graphene–Au interface in certain graphene-based field-effect transistors (GFETs) could form ice-like structures when the water film is thinner than 5 Å, potentially inducing strain in the graphene layer and affecting GFETs based sensor performance.

These findings provide a solid foundation for future work in the field of flexible and hybrid sensor systems, with potential applications in robotics, prosthetics, and human-computer interfaces.

7.2. Future Work

The research presented in this thesis can be further extended in the following ways:

- Smart gloves comprising of multiple strain sensors (presented in Chapter 3) and pressure sensors (presented in Chapter 4) and equivalent circuits to generate neural spike signals from these sensors. The signals generated from multiple sensors simultaneously can be analyzed using artificial intelligence or machine learning algorithms to identify hand gestures and interpret various object-related cues.
- The hybrid sensor described in Chapter 4 is relatively thick. Future efforts should focus on creating a thinner version, such as replacing the contact-separation-based TENG with a single-electrode TENG to achieve a more compact design.
- In Chapter 5, simulations indicated that vertically aligned ZnO nanowires in PDMS-based capacitive pressure sensors (CPS) significantly enhance sensitivity compared to horizontally aligned ones. This finding should be experimentally validated, and additional theoretical studies can explore the impact of ZnO NWs contacting each other on CPS sensitivity.
- Atomistics simulations in Chapter 6 predicted that water trapped between gold-graphene interfaces changes from an ice-like structure to a liquid structure depending on thickness. Future work should investigate how these structural variations affect the electronic properties and performance of GFET-based sensors.

References

[1] V. E. Abraira and D. D. Ginty, "The sensory neurons of touch," (in eng), *Neuron,* vol. 79, no. 4, pp. 618-639, 2013.

[2] C. D. Cox, N. Bavi, and B. Martinac, "Biophysical Principles of Ion-Channel-Mediated Mechanosensory Transduction," *Cell Rep,* vol. 29, no. 1, pp. 1-12, Oct 1 2019.

[3] U. B. Rongala, A. Mazzoni, A. Spanne, H. Jorntell, and C. M. Oddo, "Cuneate spiking neural network learning to classify naturalistic texture stimuli under varying sensing conditions," *Neural Netw,* vol. 123, pp. 273-287, Mar 2020.

[4] R. S. Dahiya, G. Metta, M. Valle, and G. Sandini, "Tactile Sensing—From Humans to Humanoids," *IEEE Transactions on Robotics,* vol. 26, no. 1, pp. 1-20, 2010.

[5] W. Navaraj, C. Smith, and R. Dahiya, "Chapter 5 - E-skin and wearable systems for health care," in *Wearable Bioelectronics,* O. Parlak, A. Salleo, and A. Turner, Eds.: Elsevier, 2020, pp. 133-178.

[6] O. Ozioko and R. Dahiya, "Smart Tactile Gloves for Haptic Interaction, Communication, and Rehabilitation," *Advanced Intelligent Systems,* https://doi.org/10.1002/aisy.202100091 vol. n/a, no. n/a, p. 2100091, 2021/09/12 2021.

[7] M. Ha, S. Lim, and H. Ko, "Wearable and flexible sensors for user-interactive health-monitoring devices," *J Mater Chem B,* vol. 6, no. 24, pp. 4043-4064, Jun 28 2018.

[8] J. Neto, R. Chirila, A. S. Dahiya, A. Christou, D. Shakthivel, and R. Dahiya, "Skin-Inspired Thermoreceptors-Based Electronic Skin for Biomimicking Thermal Pain Reflexes," *Advanced Science,* https://doi.org/10.1002/advs.202201525 vol. n/a, no. n/a, p. 2201525, 2022/07/25 2022.

[9] B. T. Nghiem *et al.*, "Providing a Sense of Touch to Prosthetic Hands," *Plastic and Reconstructive Surgery*, vol. 135, no. 6, 2015.

[10] C. M. Oddo *et al.*, "Intraneural stimulation elicits discrimination of textural features by artificial fingertip in intact and amputee humans," *eLife*, vol. 5, p. e09148, 2016/03/08 2016.

[11] R. Dahiya *et al.*, "Large-area soft e-skin: The challenges beyond sensor designs," *Proceedings of the IEEE*, vol. 107, no. 10, pp. 2016-2033, 2019.

[12] S. Khan, W. Dang, L. Lorenzelli, and R. Dahiya, "Flexible pressure sensors based on screen-printed P (VDF-TrFE) and P (VDF-TrFE)/MWCNTs," *IEEE Transactions on Semiconductor Manufacturing*, vol. 28, no. 4, pp. 486-493, 2015.

[13] Y. Kumaresan, O. Ozioko, and R. Dahiya, "Multifunctional Electronic Skin with a stack of Temperature and Pressure Sensor Arrays," *IEEE Sensors Journal*, 2021.

[14] N. M. Nair, D. Shakthivel, K. M. Panidhara, V. Adiga, P. C. Ramamurthy, and R. Dahiya, "Self-Powered e-Skin Based on Integrated Flexible Organic Photovoltaics and Transparent Touch Sensors," *Advanced Intelligent Systems*, vol. n/a, no. n/a, p. 2300103, 2023/07/26 2023.

[15] R. Dahiya *et al.*, "Large-Area Soft e-Skin: The Challenges beyond Sensor Designs," *Proc. IEEE*, vol. 107, p. 2016, 2019.

[16] A. Quellmalz *et al.*, "Influence of Humidity on Contact Resistance in Graphene Devices," *ACS Appl Mater Interfaces*, vol. 10, no. 48, pp. 41738-41746, Dec 5 2018.

[17] J. Hao, C. Bonnet, M. Amsalem, J. Ruel, and P. Delmas, "Transduction and encoding sensory information by skin mechanoreceptors," *Pflugers Arch*, vol. 467, no. 1, pp. 109-19, Jan 2015.

[18] A. Zimmerman, L. Bai, and D. Ginty David, "The gentle touch receptors of mammalian skin," *Science*, vol. 346, no. 6212, pp. 950-954, 2014/11/21 2014.

[19] M. Amjadi, K. U. Kyung, I. Park, and M. Sitti, "Stretchable, Skin-Mountable, and Wearable Strain Sensors and Their Potential Applications: A Review," *Adv. Funct. Mater.*, vol. 26, p. 1678, 2016.

[20] A. S. Dahiya *et al.*, "Review—Energy Autonomous Wearable Sensors for Smart Healthcare: A Review," *Journal of The Electrochemical Society*, vol. 167, no. 3, 2019.

[21] L. Duan, D. R. D'Hooge, and L. Cardon, "Recent progress on flexible and stretchable piezoresistive strain sensors: From design to application," *Progress in Materials Science*, vol. 114, p. 100617, 2020/10/01/ 2020.

[22] P. Escobedo, M. Ntagios, D. Shakthivel, W. T. Navaraj, and R. Dahiya, "Energy Generating Electronic Skin with Intrinsic Tactile Sensing without Touch Sensors," *IEEE Trans. Robot.*, vol. 37, p. 683, 2021.

[23] K.-H. Ha, H. Huh, Z. Li, and N. Lu, "Soft Capacitive Pressure Sensors: Trends, Challenges, and Perspectives," *ACS Nano*, vol. 16, no. 3, pp. 3442-3448, 2022/03/22 2022.

[24] A. Mazzoni, U. B. Rongala, and C. M. Oddo, "Decoding of naturalistic textures from spike patterns of neuromorphic artificial mechanoreceptors," *BMC Neuroscience*, vol. 16, no. S1, 2015.

[25] Y. Dong, S. Mihalas, S. S. Kim, T. Yoshioka, S. Bensmaia, and E. Niebur, "A simple model of mechanotransduction in primate glabrous skin," *J Neurophysiol*, vol. 109, no. 5, pp. 1350-9, Mar 2013.

[26] A. Handler and D. D. Ginty, "The mechanosensory neurons of touch and their mechanisms of activation," *Nat Rev Neurosci*, vol. 22, no. 9, pp. 521-537, Sep 2021.

[27] C. M. Walsh, D. M. Bautista, and E. A. Lumpkin, "Mammalian touch catches up," *Curr Opin Neurobiol*, vol. 34, pp. 133-9, Oct 2015.

[28] S. L. Geffeney and M. B. Goodman, "How we feel: ion channel partnerships that detect mechanical inputs and give rise to touch and pain perception," *Neuron*, vol. 74, no. 4, pp. 609-19, May 24 2012.

[29] H. P. Saal, B. P. Delhaye, B. C. Rayhaun, and S. J. Bensmaia, "Simulating tactile signals from the whole hand with millisecond precision," *Proceedings of the National Academy of Sciences*, vol. 114, no. 28, p. E5693, 2017.

[30] K.-Y. Chun, Y. J. Son, E.-S. Jeon, S. Lee, and C.-S. Han, "A Self-Powered Sensor Mimicking Slow- and Fast-Adapting Cutaneous Mechanoreceptors," *Advanced Materials,* vol. 30, no. 12, p. 1706299, 2018.

[31] D. R. Lesniak and G. J. Gerling, "Predicting SA-I mechanoreceptor spike times with a skin-neuron model," *Mathematical Biosciences,* vol. 220, no. 1, pp. 15-23, 2009/07/01/ 2009.

[32] A. Parvizi-Fard, M. Amiri, D. Kumar, M. M. Iskarous, and N. V. Thakor, "A functional spiking neuronal network for tactile sensing pathway to process edge orientation," *Sci Rep,* vol. 11, no. 1, p. 1320, Jan 14 2021.

[33] L. J. Drew, F. Rugiero, and J. N. Wood, "Touch," in *Mechanosensitive Ion Channels, Part B*(Current Topics in Membranes, 2007, pp. 425-465.

[34] M. Ayyildiz, M. Scaraggi, O. Sirin, C. Basdogan, and B. N. J. Persson, "Contact mechanics between the human finger and a touchscreen under electroadhesion," *Proceedings of the National Academy of Sciences,* vol. 115, no. 50, p. 12668, 2018.

[35] J. C. Gumbart, "A Novel Approach to Simulating the Gating Transitions of Mechanosensitive Channels," *Biophys J,* vol. 120, no. 2, pp. 185-186, Jan 19 2021.

[36] B. Martinac, "Mechanosensitive ion channels: molecules of mechanotransduction," *Journal of Cell Science,* vol. 117, no. 12, pp. 2449-2460, 2004.

[37] J. L. Nourse and M. M. Pathak, "How cells channel their stress: Interplay between Piezo1 and the cytoskeleton," *Semin Cell Dev Biol,* vol. 71, pp. 3-12, Nov 2017.

[38] M. Nakatani, S. Maksimovic, Y. Baba, and E. A. Lumpkin, "Mechanotransduction in epidermal Merkel cells," *Pflugers Arch,* vol. 467, no. 1, pp. 101-8, Jan 2015.

[39] J. M. Kefauver, A. B. Ward, and A. Patapoutian, "Discoveries in structure and physiology of mechanically activated ion channels," *Nature,* vol. 587, no. 7835, pp. 567-576, 2020/11/01 2020.

[40] E. Perozo, D. M. Cortes, P. Sompornpisut, A. Kloda, and B. Martinac, "Open channel structure of MscL and the gating mechanism of mechanosensitive channels," *Nature,* vol. 418, no. 6901, pp. 942-948, 2002/08/01 2002.

[41] V. Oakes, S. Furini, and C. Domene, "Voltage-Gated Sodium Channels: Mechanistic Insights From Atomistic Molecular Dynamics Simulations," *Curr Top Membr,* vol. 78, pp. 183-214, 2016.

[42] H. Katsuta, Y. Sawada, and M. Sokabe, "Biophysical Mechanisms of Membrane-Thickness-Dependent MscL Gating: An All-Atom Molecular Dynamics Study," *Langmuir,* vol. 35, no. 23, pp. 7432-7442, Jun 11 2019.

[43] F. Khalili-Araghi, J. Gumbart, P. C. Wen, M. Sotomayor, E. Tajkhorshid, and K. Schulten, "Molecular dynamics simulations of membrane channels and transporters," *Curr Opin Struct Biol,* vol. 19, no. 2, pp. 128-37, Apr 2009.

[44] W. Jiang *et al.*, "Crowding-induced opening of the mechanosensitive Piezo1 channel in silico," *Commun Biol,* vol. 4, no. 1, p. 84, Jan 19 2021.

[45] W. Zheng, Y. A. Nikolaev, E. O. Gracheva, and S. N. Bagriantsev, "Piezo2 integrates mechanical and thermal cues in vertebrate mechanoreceptors," *Proc Natl Acad Sci U S A,* vol. 116, no. 35, pp. 17547-17555, Aug 27 2019.

[46] R. Dahiya, "E-Skin: From Humanoids to Humans [Point of View]," *Proceedings of the IEEE,* vol. 107, no. 2, pp. 247-252, 2019.

[47] E. W. Hill, A. Vijayaragahvan, and K. Novoselov, "Graphene Sensors," *IEEE Sens. J.,* vol. 11, p. 3161, 2011.

[48] P. Karipoth, A. Pullanchiyodan, A. Christou, and R. Dahiya, "Graphite-Based Bioinspired Piezoresistive Soft Strain Sensors with Performance Optimized for Low Strain Values," *ACS Applied Materials & Interfaces,* vol. 13, no. 51, pp. 61610-61619, 2021/12/29 2021.

[49] E. K. Kim, S. A. Wellnitz, S. M. Bourdon, E. A. Lumpkin, and G. J. Gerling, "Force Sensor in Simulated Skin and Neural Model Mimic Tactile SAI Afferent Spiking Response to Ramp and Hold Stimuli," *J. NeuroEng. Rehabil.,* vol. 9, p. 45, 2012.

[50] H. C. Koydemir and A. Ozcan, "Wearable and Implantable Sensors for Biomedical Applications," *Annu. Rev. Anal. Chem.*, p. 127, 2018.

[51] X. Wang, L. Dong, H. Zhang, R. Yu, C. Pan, and Z. L. Wang, "Recent Progress in Electronic Skin," *Advanced Science,* vol. 2, no. 10, p. 1500169, 2015/10/01 2015.

[52] X. Wang, Z. Liu, and T. Zhang, "Flexible Sensing Electronics for Wearable/Attachable Health Monitoring," *Small,* vol. 13, p. 1602790, 2017.

[53] S. Bilent, T. H. N. Dinh, E. Martincic, and P.-Y. Joubert, "Porous Polymer Based Flexible Pressure Sensors for Medical Applications," presented at the Eurosensors 2018, 2018.

[54] C. M. Boutry *et al.*, "A stretchable and biodegradable strain and pressure sensor for orthopaedic application," *Nature Electronics,* vol. 1, no. 5, pp. 314-321, 2018.

[55] B.-Y. Lee, J. Kim, H. Kim, C. Kim, and S.-D. Lee, "Low-cost flexible pressure sensor based on dielectric elastomer film with micro-pores," *Sensors and Actuators A: Physical,* vol. 240, pp. 103-109, 2016/04/01/ 2016.

[56] M. Bhattacharjee, F. Nikbakhtnasrabadi, and R. Dahiya, "Printed Chipless Antenna as Flexible Temperature Sensor," *IEEE Internet of Things Journal,* vol. 8, no. 6, pp. 5101-5110, 2021.

[57] J. C. Yang *et al.*, "Microstructured Porous Pyramid-Based Ultrahigh Sensitive Pressure Sensor Insensitive to Strain and Temperature," *ACS Applied Materials & Interfaces,* vol. 11, no. 21, pp. 19472-19480, 2019/05/29 2019.

[58] S. H. Bae, Y. Lee, B. K. Sharma, H. J. Lee, H. J. Kim, and J. H. Ahn, "Graphene-Based Transparent Strain Sensor," *Carbon,* vol. 51, no. 23, p. 6, 2013.

[59] Q. Chen, Y. Sun, Y. Wang, H. Cheng, and Q.-M. Wang, "ZnO nanowires–polyimide nanocomposite piezoresistive strain sensor," *Sensors and Actuators A: Physical,* vol. 190, pp. 161-167, 2013/02/01/ 2013.

[60] F. He *et al.*, "Stretchable, biocompatible, and multifunctional silk fibroin-based hydrogels toward wearable strain/pressure sensors and triboelectric nanogenerators," *ACS applied materials & interfaces,* vol. 12, no. 5, pp. 6442-6450, 2020.

[61] D. J. Lipomi *et al.*, "Skin-Like Pressure and Strain Sensors Based on Transparent Elastic Films of Carbon Nanotubes," *Nat. Nanotechnol.*, vol. 6, p. 788, 2011.

[62] J. J. Park, W. J. Hyun, S. C. Mun, Y. T. Park, and O. O. Park, "Highly Stretchable and Wearable Graphene Strain Sensors with Controllable Sensitivity for Human Motion Monitoring," *ACS Appl. Mater. Interfaces*, vol. 7, p. 6317, 2015.

[63] A. Beniwal, P. Ganguly, A. K. Aliyana, G. Khandelwal, and R. Dahiya, "Screen-printed graphene-carbon ink based disposable humidity sensor with wireless communication," *Sensors and Actuators B: Chemical*, vol. 374, p. 132731, 2023/01/01/ 2023.

[64] D. J. Joshi, J. R. Koduru, N. I. Malek, C. M. Hussain, and S. K. Kailasa, "Surface modifications and analytical applications of graphene oxide: A review," *TrAC Trends in Analytical Chemistry*, vol. 144, p. 116448, 2021/11/01/ 2021.

[65] R. Li *et al.*, "Research progress of flexible capacitive pressure sensor for sensitivity enhancement approaches," *Sensors and Actuators A: Physical*, vol. 321, p. 112425, 2021/04/15/ 2021.

[66] Y. Liu *et al.*, "Moisture-resistant MXene-sodium alginate sponges with sustained superhydrophobicity for monitoring human activities," *Chemical Engineering Journal*, vol. 432, p. 134370, 2022/03/15/ 2022.

[67] T. D. Nguyen and J. S. Lee, "Recent Development of Flexible Tactile Sensors and Their Applications," *Sensors (Basel)*, vol. 22, no. 1, Dec 22 2021.

[68] V. Adepu, N. Bokka, V. Selamneni, T. G. Paramasivan, and P. Sahatiya, "Flexible and Wearable Strain/Pressure Sensors," in *Encyclopedia of Materials: Electronics*, A. S. M. A. Haseeb, Ed. Oxford: Academic Press, 2023, pp. 180-198.

[69] Y. Tang *et al.*, "Highly Stretchable and Ultrasensitive Strain Sensor Based on Reduced Graphene Oxide Microtubes-Elastomer Composite," *ACS Appl. Mater. Interfaces*, vol. 7, p. 27432, 2015.

[70] L. Chen *et al.*, "Strain-Gated Field Effect Transistor of a MoS2-ZnO 2D-1D Hybrid Structure," *ACS Nano*, vol. 10, no. 1, pp. 1546-51, Jan 26 2016.

[71] Y. Zhao *et al.*, "Advancing the pressure sensing performance of conductive CNT/PDMS composite film by constructing a hierarchical-structured surface," *Nano Materials Science*, 2022/01/04/ 2022.

[72] R. Chirila, A. S. Dahiya, and R. Dahiya, "Flexible Strain and Pressure Sensors for Electronic Skin," in *Encyclopedia of Materials: Electronics*, A. S. M. A. Haseeb, Ed. Oxford: Academic Press, 2023, pp. 138-150.

[73] n. Alamusi, N. Hu, H. Fukunaga, S. Atobe, Y. Liu, and J. Li, "Piezoresistive Strain Sensors Made from Carbon Nanotubes Based Polymer Nanocomposites," *Sensors*, vol. 11, p. 10691, 2011.

[74] P. Won *et al.*, "Stretchable and Transparent Kirigami Conductor of Nanowire Percolation Network for Electronic Skin Applications," *Nano Lett*, vol. 19, no. 9, pp. 6087-6096, Sep 11 2019.

[75] H. Souri *et al.*, "Wearable and Stretchable Strain Sensors: Materials, Sensing Mechanisms, and Applications," *Advanced Intelligent Systems*, vol. 2, no. 8, p. 2000039, 2020/08/01 2020.

[76] C. S. Boland *et al.*, "Sensitive, High-Strain, High-Rate Bodily Motion Sensors Based on Graphene–Rubber Composites," *ACS Nano*, vol. 8, p. 8819, 2014.

[77] Y. Gao, X. Fang, J. Tan, T. Lu, L. Pan, and F. Xuan, "Highly sensitive strain sensors based on fragmentized carbon nanotube/polydimethylsiloxane composites," *Nanotechnology*, vol. 29, no. 23, p. 235501, 2018/04/12 2018.

[78] Z. Wen *et al.*, "Ultra-highly sensitive, low hysteretic and flexible pressure sensor based on porous MWCNTs/Ecoflex elastomer composites," *Journal of Materials Science: Materials in Electronics*, vol. 29, no. 24, pp. 20978-20983, 2018/12/01 2018.

[79] W. Zhai *et al.*, "Multifunctional flexible carbon black/polydimethylsiloxane piezoresistive sensor with ultrahigh linear range, excellent durability and oil/water separation capability," *Chemical Engineering Journal*, vol. 372, pp. 373-382, 2019/09/15/ 2019.

[80] J. Chen, Y. Zhu, and W. Jiang, "A stretchable and transparent strain sensor based on sandwich-like PDMS/CNTs/PDMS composite containing an ultrathin

conductive CNT layer," *Composites Science and Technology,* vol. 186, p. 107938, 2020/01/20/ 2020.

[81] R. B. Mishra, N. El-Atab, A. M. Hussain, and M. M. Hussain, "Recent Progress on Flexible Capacitive Pressure Sensors: From Design and Materials to Applications," *Advanced Materials Technologies,* https://doi.org/10.1002/admt.202001023 vol. 6, no. 4, p. 2001023, 2021/04/01 2021.

[82] S. C. Mannsfeld *et al.*, "Highly Sensitive Flexible Pressure Sensors with Microstructured Rubber Dielectric Layers," *Nat. Mater.,* vol. 9, p. 859, 2010.

[83] T. Pakawan *et al.*, "Compressive Behaviors of Micropillar Sheets Made of PDMS Material Using the Finite Element Method," *Engineering Journal,* vol. 24, no. 4, pp. 73-84, 2020.

[84] S. Mishra, M. S. Baghini, D. Shakthivel, B. Rai, and R. Dahiya, "Sensitivity Analysis of ZnO NWs Based Soft Capacitive Pressure Sensors using Finite Element Modeling," in *2022 IEEE International Conference on Flexible and Printable Sensors and Systems (FLEPS)*, 2022, pp. 1-4.

[85] C.-R. Yang, L.-J. Wang, and S.-F. Tseng, "Arrayed porous polydimethylsiloxane/barium titanate microstructures for high-sensitivity flexible capacitive pressure sensors," *Ceramics International,* vol. 48, no. 9, pp. 13144-13153, 2022/05/01/ 2022.

[86] B. Zhuo, S. Chen, M. Zhao, and X. Guo, "High Sensitivity Flexible Capacitive Pressure Sensor Using Polydimethylsiloxane Elastomer Dielectric Layer Micro-Structured by 3-D Printed Mold," *IEEE Journal of the Electron Devices Society,* vol. 5, no. 3, pp. 219-223, 2017.

[87] Y. Kumaresan, S. Ma, O. Ozioko, and R. Dahiya, "Soft Capacitive Pressure Sensor with Enhanced Sensitivity assisted by ZnO NW Interlayers and Airgap," *IEEE Sensors Journal,* pp. 1-1, 2022.

[88] H.-J. Tseng, W.-C. Tian, and W.-J. Wu, "Flexible PZT thin film tactile sensor for biomedical monitoring," *Sensors,* vol. 13, no. 5, pp. 5478-5492, 2013.

[89] D. Shakthivel, A. S. Dahiya, R. Mukherjee, and R. Dahiya, "Inorganic semiconducting nanowires for green energy solutions," *Current Opinion in Chemical Engineering*, vol. 34, p. 100753, 2021/12/01/ 2021.

[90] E. S. Hosseini, L. Manjakkal, D. Shakthivel, and R. Dahiya, "Glycine–chitosan-based flexible biodegradable piezoelectric pressure sensor," *ACS applied materials & interfaces*, vol. 12, no. 8, pp. 9008-9016, 2020.

[91] X. Xiao *et al.*, "High-Strain Sensors Based on ZnO Nanowire/Polystyrene Hybridized Flexible Films," *Adv. Mater.*, vol. 23, p. 5440, 2011.

[92] L. Persano *et al.*, "High performance piezoelectric devices based on aligned arrays of nanofibers of poly (vinylidenefluoride-co-trifluoroethylene)," *Nature communications*, vol. 4, no. 1, p. 1633, 2013.

[93] S. Deswal, G. Khandelwal, and R. Dahiya, "Molecular Ferroelectric Based Biocompatible Flexible Piezoelectric Pressure Sensor," *IEEE Sensors Letters*, vol. 7, no. 6, pp. 1-4, 2023.

[94] F.-R. Fan, L. Lin, G. Zhu, W. Wu, R. Zhang, and Z. L. Wang, "Transparent Triboelectric Nanogenerators and Self-Powered Pressure Sensors Based on Micropatterned Plastic Films," *Nano Letters*, vol. 12, no. 6, pp. 3109-3114, 2012/06/13 2012.

[95] G. Khandelwal, N. P. Maria Joseph Raj, and S.-J. Kim, "Triboelectric nanogenerator for healthcare and biomedical applications," *Nano Today*, vol. 33, p. 100882, 2020/08/01/ 2020.

[96] G. Khandelwal and R. Dahiya, "Self-Powered Active Sensing Based on Triboelectric Generators," *Advanced Materials*, vol. 34, no. 33, p. 2200724, 2022/08/01 2022.

[97] Z. L. Wang, "Triboelectric nanogenerators as new energy technology and self-powered sensors–Principles, problems and perspectives," *Faraday discussions*, vol. 176, pp. 447-458, 2014.

[98] Z. L. Wang, J. Chen, and L. Lin, "Progress in triboelectric nanogenerators as a new energy technology and self-powered sensors," *Energy & Environmental Science*, vol. 8, no. 8, pp. 2250-2282, 2015.

[99] X. Pu *et al.*, "Ultrastretchable, transparent triboelectric nanogenerator as electronic skin for biomechanical energy harvesting and tactile sensing," *Science Advances*, vol. 3, no. 5, p. e1700015.

[100] C. Garcia, I. Trendafilova, R. Guzman de Villoria, and J. Sanchez del Rio, "Self-powered pressure sensor based on the triboelectric effect and its analysis using dynamic mechanical analysis," *Nano Energy*, vol. 50, pp. 401-409, 2018/08/01/ 2018.

[101] J. Pignanelli, K. Schlingman, T. B. Carmichael, S. Rondeau-Gagné, and M. J. Ahamed, "A comparative analysis of capacitive-based flexible PDMS pressure sensors," *Sensors and Actuators A: Physical*, vol. 285, pp. 427-436, 2019/01/01/ 2019.

[102] L. Ma *et al.*, "A highly sensitive and flexible capacitive pressure sensor based on a micro-arrayed polydimethylsiloxane dielectric layer," *Journal of Materials Chemistry C*, 10.1039/C8TC04297G vol. 6, no. 48, pp. 13232-13240, 2018.

[103] Y. Qin *et al.*, "Mechanically Flexible Graphene / Polyimide Nanocomposite Foam for Strain Sensor Application," *ACS Nano*, vol. 9, p. 8933, 2015.

[104] A. Usman, K. M. Zia, M. Zuber, S. Tabasum, S. Rehman, and F. Zia, "Chitin and chitosan based polyurethanes: A review of recent advances and prospective biomedical applications," *International journal of biological macromolecules*, vol. 86, pp. 630-645, 2016.

[105] D. J. Cohen, D. Mitra, K. Peterson, and M. M. Maharbiz, "A Highly Elastic, Capacitive Strain Gauge Based on Percolating Nanotube Networks," *Nano Lett.*, vol. 12, p. 1821, 2012.

[106] C. Parameswaran and D. Gupta, "Large area flexible pressure/strain sensors and arrays using nanomaterials and printing techniques," *Nano Convergence*, vol. 6, no. 1, p. 28, 2019/09/09 2019.

[107] M. Amjadi, Y. J. Yoon, and I. Park, "Ultra-Stretchable and Skin-Mountable Strain Sensors Using Carbon Nanotubes–Ecoflex Nanocomposites," *Nanotechnology*, vol. 26, p. 375501, 2015.

[108] C. Mattmann, F. Clemens, and G. Tröster, "Sensor for Measuring Strain in Textile," *Sensors*, vol. 8, p. 3719, 2008.

[109] S. Zhai *et al.*, "Textile Energy Storage: Structural Design Concepts, Material Selection and Future Perspectives," *Energy Storage Mater.*, p. 123, 2016.

[110] F. Lourussi, E. M. Scilingo, M. Tesconi, A. Tognetti, and D. D. Rossi, "Strain Sensing Fabric for Hand Posture and Gesture Monitoring," *IEEE Trans. Inf. Technol. Biomed.*, p. 372, 2005.

[111] T. Yang *et al.*, "Tactile Sensing System Based on Arrays of Graphene Woven Microfabrics: Electromechanical Behavior and Electronic Skin Application," *ACS Nano*, vol. 9, p. 10867, 2015.

[112] Y. Zhang, S. Sezen, M. Ahmadi, X. Cheng, and R. Rajamani, "Paper-Based Supercapacitive Mechanical Sensors," *Sci. Rep.*, vol. 8, p. 16284, 2018.

[113] X. Li *et al.*, "Large-Area Synthesis of High-Quality and Uniform Graphene Films on Copper Foils," *Science*, vol. 324, p. 1312, 2009.

[114] E. O. Polat, O. Balci, N. Kakenov, H. B. Uzlu, C. Kocabas, and R. Dahiya, "Synthesis of Large Area Graphene for High Performance in Flexible Optoelectronic Devices," *Scientific Reports*, vol. 5, no. 1, p. 16744, 2015/11/18 2015.

[115] F. Chen, Q. Chen, Q. Song, H. Lu, and M. Ma, "Strong and Stretchable Polypyrrole Hydrogels with Biphase Microstructure as Electrodes for Substrate-Free Stretchable Supercapacitors," *Adv. Mater. Interfaces*, vol. 6, p. 1900133, 2019.

[116] G. F. Yu *et al.*, "Patterned, Highly Stretchable and Conductive Nanofibrous PANI/PVDF Strain Sensors Based on Electrospinning and in situ Polymerization," *Nanoscale*, vol. 8, p. 2944, 2016.

[117] R. S. Kammel and R. S. Sabry, "Effects of the aspect ratio of ZnO nanorods on the performance of piezoelectric nanogenerators," *Journal of Science: Advanced Materials and Devices*, vol. 4, no. 3, pp. 420-424, 2019/09/01/ 2019.

[118] D. Shakthivel, M. Ahmad, M. R. Alenezi, R. Dahiya, and S. R. P. Silva, 1D Semiconducting Nanostructures for Flexible and Large-Area Electronics: Growth

Mechanisms and Suitability, Cambridge: Cambridge University Press, 2019. [Online]. Available: https://www.cambridge.org/core/elements/1d-semiconducting-nanostructures-for-flexible-and-largearea-electronics/AB256ABD4C286D6E270A8021CFD930FE.

[119] X. Zang, Q. Zhou, J. Chang, Y. Liu, and L. Lin, "Graphene and carbon nanotube (CNT) in MEMS/NEMS applications," *Microelectronic Engineering*, vol. 132, pp. 192-206, 2015/01/25/ 2015.

[120] Y. Zhang *et al.*, "Carbon nanotubes/acetylene black/Ecoflex with corrugated microcracks for enhanced sensitivity for stretchable strain sensors," *Journal of Materials Science: Materials in Electronics*, vol. 31, no. 17, pp. 14145-14156, 2020/09/01 2020.

[121] A. Esteghamat and O. Akhavan, "Graphene as the ultra-transparent conductive layer in developing the nanotechnology-based flexible smart touchscreens," *Microelectronic Engineering*, 2022.

[122] S. W. Lee *et al.*, "Enhanced Sensitivity of Patterned Graphene Strain Sensors Used for Monitoring Subtle Human Body Motions," *ACS Applied Materials & Interfaces*, vol. 9, no. 12, pp. 11176-11183, 2017/03/29 2017.

[123] L. Manjakkal, A. Pullanchiyodan, N. Yogeswaran, E. S. Hosseini, and R. Dahiya, "A Wearable Supercapacitor Based on Conductive PEDOT:PSS-Coated Cloth and a Sweat Electrolyte," *Adv. Mater.*, vol. 32, p. 1907254, 2020.

[124] Z. R. Ramadhan *et al.*, "Conductive PEDOT:PSS on surface-functionalized chitosan biopolymers for stretchable skin-like electronics," *Organic Electronics*, vol. 94, 2021.

[125] M. Soni, M. Bhattacharjee, M. Ntagios, and R. Dahiya, "Printed Temperature Sensor Based on PEDOT: PSS-Graphene Oxide Composite," *IEEE Sensors Journal*, vol. 20, no. 14, pp. 7525-7531, 2020.

[126] X. Yu *et al.*, "Stretchable, Conductive, and Stable PEDOT-Modified Textiles through a Novel In Situ Polymerization Process for Stretchable Supercapacitors," *Adv. Mater. Technol.*, vol. 1, p. 1600009, 2016.

[127] S. Masihi *et al.*, "Highly Sensitive Porous PDMS-Based Capacitive Pressure Sensors Fabricated on Fabric Platform for Wearable Applications," *ACS Sensors*, vol. 6, no. 3, pp. 938-949, 2021/03/26 2021.

[128] X. Yang, Y. Wang, and X. Qing, "A flexible capacitive pressure sensor based on ionic liquid," *Sensors*, vol. 18, no. 7, p. 2395, 2018.

[129] X. Yang, Y. Wang, H. Sun, and X. Qing, "A flexible ionic liquid-polyurethane sponge capacitive pressure sensor," *Sensors and Actuators A: Physical*, vol. 285, pp. 67-72, 2019.

[130] V. K. Rao, N. Shauloff, X. Sui, H. D. Wagner, and R. Jelinek, "Polydiacetylene hydrogel self-healing capacitive strain sensor," *Journal of Materials Chemistry C*, vol. 8, no. 18, pp. 6034-6041, 2020.

[131] A. Wang *et al.*, "Hydrogen-bonded network enables semi-interpenetrating ionic conductive hydrogels with high stretchability and excellent fatigue resistance for capacitive/resistive bimodal sensors," *Chemical Engineering Journal*, vol. 411, p. 128506, 2021.

[132] J. Qian *et al.*, "A nonmetallic stretchable nylon-modified high performance triboelectric nanogenerator for energy harvesting," *Advanced functional materials*, vol. 30, no. 4, p. 1907414, 2020.

[133] S. S. Rana *et al.*, "Cation functionalized nylon composite nanofibrous mat as a highly positive friction layer for robust, high output triboelectric nanogenerators and self-powered sensors," *Nano Energy*, vol. 88, p. 106300, 2021.

[134] J. Han, J. Yang, W. Gao, and H. Bai, "Ice-Templated, Large-Area Silver Nanowire Pattern for Flexible Transparent Electrode," *Advanced Functional Materials*, vol. 31, no. 16, 2021.

[135] L. Hu, H. S. Kim, J. Y. Lee, P. Peumans, and Y. Cui, "Scalable Coating and Properties of Transparent, Flexible, Silver Nanowire Electrodes," *ACS Nano*, vol. 4, p. 2955, 2010.

[136] Y. Altin, M. Tas, İ. Borazan, A. Demir, and A. Bedeloglu, "Solution-processed transparent conducting electrodes with graphene, silver nanowires and

PEDOT:PSS as alternative to ITO," *Surface and Coatings Technology,* vol. 302, pp. 75-81, 2016.

[137] K. Liu *et al.*, "Polyaniline nanofiber wrapped fabric for high performance flexible pressure sensors," *Polymers,* vol. 11, no. 7, p. 1120, 2019.

[138] R. S. Datta *et al.*, "Flexible Two-Dimensional Indium Tin Oxide Fabricated Using a Liquid Metal Printing Technique," *Nat. Electron.*, vol. 3, p. 51, 2020.

[139] W. J. Hyun, E. B. Secor, M. C. Hersam, C. D. Frisbie, and L. F. Francis, "High-resolution patterning of graphene by screen printing with a silicon stencil for highly flexible printed electronics," *Adv Mater,* vol. 27, no. 1, pp. 109-15, Jan 7 2015.

[140] N. Zavanelli and W. H. Yeo, "Advances in Screen Printing of Conductive Nanomaterials for Stretchable Electronics," *ACS Omega,* vol. 6, no. 14, pp. 9344-9351, Apr 13 2021.

[141] L. Wang, L. Wu, Y. Wang, J. Luo, H. Xue, and J. Gao, "Drop casting based superhydrophobic and electrically conductive coating for high performance strain sensing," *Nano Materials Science,* vol. 4, no. 2, pp. 178-184, 2022.

[142] J. Yang, L. Chang, C. Ma, Z. Cao, and H. Liu, "Highly Electrically Conductive Flexible Ionogels by Drop-Casting Ionic Liquid/PEDOT: PSS Composite Liquids onto Hydrogel Networks," *Macromolecular Rapid Communications,* vol. 43, no. 1, p. 2100557, 2022.

[143] T. H. da Costa and J. W. Choi, "Fabrication and patterning methods of flexible sensors using carbon nanomaterials on polymers," *Advanced Intelligent Systems,* vol. 2, no. 5, p. 1900179, 2020.

[144] M. J. Bathaei *et al.*, "Photolithography-Based Microfabrication of Biodegradable Flexible and Stretchable Sensors," *Advanced Materials,* vol. 35, no. 6, p. 2207081, 2023.

[145] L. Huang, Y. Huang, J. Liang, X. Wan, and Y. Chen, "Graphene-based conducting inks for direct inkjet printing of flexible conductive patterns and their applications in electric circuits and chemical sensors," *Nano Research,* vol. 4, pp. 675-684, 2011.

[146] J. Sun *et al.*, "A novel pre-deposition assisted strategy for inkjet printing graphene-based flexible pressure sensor with enhanced performance," *Carbon*, vol. 196, pp. 85-91, 2022.

[147] K. Yan, J. Li, L. Pan, and Y. Shi, "Inkjet printing for flexible and wearable electronics," *Apl Materials*, vol. 8, no. 12, 2020.

[148] M. Alsharari, B. Chen, and W. Shu, "Sacrificial 3D printing of highly porous, soft pressure sensors," *Advanced Electronic Materials*, vol. 8, no. 1, p. 2100597, 2022.

[149] Y. Guo *et al.*, "Degradable and Fully Recyclable Dynamic Thermoset Elastomer for 3D-Printed Wearable Electronics," *Advanced Functional Materials*, vol. 31, no. 9, 2020.

[150] O. Ozioko, H. Nassar, and R. Dahiya, "3D Printed Interdigitated Capacitor Based Tilt Sensor," *IEEE Sensors Journal*, vol. 21, no. 23, pp. 26252-26260, 2021.

[151] Z. Tang, S. Jia, C. Zhou, and B. Li, "3D printing of highly sensitive and large-measurement-range flexible pressure sensors with a positive piezoresistive effect," *ACS applied materials & interfaces*, vol. 12, no. 25, pp. 28669-28680, 2020.

[152] V. Mitrakos, L. Macintyre, F. C. Denison, P. J. Hands, and M. P. Desmulliez, "Design, manufacture and testing of capacitive pressure sensors for low-pressure measurement ranges," *Micromachines*, vol. 8, no. 2, p. 41, 2017.

[153] J. Park *et al.*, "Individually addressable and flexible pressure sensor matrixes with ZnO nanotube arrays on graphene," *NPG Asia Materials*, vol. 14, no. 1, p. 40, 2022.

[154] X. Fu, A. M. Al-Jumaily, M. Ramos, A. Meshkinzar, and X. Huang, "Stretchable and sensitive sensor based on carbon nanotubes/polymer composite with serpentine shapes via molding technique," *Journal of Biomaterials Science, Polymer Edition*, vol. 30, no. 13, pp. 1227-1241, 2019/09/02 2019.

[155] T. Han, A. Nag, N. Afsarimanesh, S. C. Mukhopadhyay, S. Kundu, and Y. Xu, "Laser-assisted printed flexible sensors: a review," *Sensors*, vol. 19, no. 6, p. 1462, 2019.

[156] Y. Zhu, H. Cai, H. Ding, N. Pan, and X. Wang, "Fabrication of low-cost and highly sensitive graphene-based pressure sensors by direct laser scribing polydimethylsiloxane," *ACS applied materials & interfaces,* vol. 11, no. 6, pp. 6195-6200, 2019.

[157] T. H. N. Dinh, E. Martincic, E. Dufour-Gergam, and P.-Y. Joubert, "Capacitive flexible pressure sensor: microfabrication process and experimental characterization," *Microsystem Technologies,* vol. 22, pp. 465-471, 2016.

[158] H. Li, G. Ding, and Z. Yang, "A high sensitive flexible pressure sensor designed by silver nanowires embedded in polyimide (AgNW-PI)," *Micromachines,* vol. 10, no. 3, p. 206, 2019.

[159] T. Kim, A. Canlier, G. H. Kim, J. Choi, M. Park, and S. M. Han, "Electrostatic Spray Deposition of Highly Transparent Silver Nanowire Electrode on Flexible Substrate," *ACS Appl. Mater. Interfaces,* vol. 5, p. 788, 2013.

[160] F. Selzer *et al.*, "A spray-coating process for highly conductive silver nanowire networks as the transparent top-electrode for small molecule organic photovoltaics," *Nanoscale,* vol. 7, no. 6, pp. 2777-83, Feb 14 2015.

[161] A. Zumeit, A. S. Dahiya, A. Christou, D. Shakthivel, and R. Dahiya, "Direct roll transfer printed silicon nanoribbon arrays based high-performance flexible electronics," *npj Flexible Electronics,* vol. 5, no. 1, 2021.

[162] Y. Ma *et al.*, "A highly flexible and sensitive piezoresistive sensor based on MXene with greatly changed interlayer distances," *Nature communications,* vol. 8, no. 1, p. 1207, 2017.

[163] X. Zhao, B. Chen, G. Wei, J. M. Wu, W. Han, and Y. Yang, "Polyimide/graphene nanocomposite foam-based wind-driven triboelectric nanogenerator for self-powered pressure sensor," *Advanced Materials Technologies,* vol. 4, no. 5, p. 1800723, 2019.

[164] J. Shi *et al.*, "Multiscale Hierarchical Design of a Flexible Piezoresistive Pressure Sensor with High Sensitivity and Wide Linearity Range," *Small,* Article vol. 14, no. 27, 2018, Art. no. 1800819.

[165] C. Mu *et al.*, "Enhanced piezocapacitive effect in CaCu3Ti4O12–polydimethylsiloxane composited sponge for ultrasensitive flexible capacitive sensor," *ACS Applied Nano Materials*, vol. 1, no. 1, pp. 274-283, 2017.

[166] N. Bai *et al.*, "Graded intrafillable architecture-based iontronic pressure sensor with ultra-broad-range high sensitivity," *Nature communications*, vol. 11, no. 1, p. 209, 2020.

[167] J. Jia, G. Huang, J. Deng, and K. Pan, "Skin-inspired flexible and high-sensitivity pressure sensors based on rGO films with continuous-gradient wrinkles," *Nanoscale*, vol. 11, no. 10, pp. 4258-4266, 2019.

[168] C. Yang *et al.*, "Highly sensitive wearable pressure sensors based on three-scale nested wrinkling microstructures of polypyrrole films," *ACS applied materials & interfaces*, vol. 10, no. 30, pp. 25811-25818, 2018.

[169] O. Ozioko, P. Karipoth, P. Escobedo, M. Ntagios, A. Pullanchiyodan, and R. Dahiya, "SensAct: The Soft and Squishy Tactile Sensor with Integrated Flexible Actuator," *Advanced Intelligent Systems*, vol. 3, no. 3, 2021.

[170] M. Ntagios, W. T. Navaraj, and R. Dahiya, "3D printed phalanx packaged with embedded pressure sensor," in *2018 IEEE SENSORS*, 2018, pp. 1-4: IEEE.

[171] S. Y. Kim, S. Park, H. W. Park, D. H. Park, Y. Jeong, and D. H. Kim, "Highly sensitive and multimodal all-carbon skin sensors capable of simultaneously detecting tactile and biological stimuli," *Advanced materials*, vol. 28, no. 27, pp. 4178-4185, 2015.

[172] M. Amjadi, A. Pichitpajongkit, S. Lee, S. Ryu, and I. Park, "Highly Stretchable and Sensitive Strain Sensor Based on Silver Nanowire-Elastomer Nanocomposite," *ACS Nano*, vol. 8, p. 5154, 2014.

[173] W. Zhang, R. Zhu, V. Nguyen, and R. Yang, "Highly sensitive and flexible strain sensors based on vertical zinc oxide nanowire arrays," *Sensors and Actuators A: Physical*, vol. 205, pp. 164-169, 2014.

[174] H. Sun *et al.*, "A highly sensitive and stretchable yarn strain sensor for human motion tracking utilizing a wrinkle-assisted crack structure," *ACS applied materials & interfaces*, vol. 11, no. 39, pp. 36052-36062, 2019.

[175] X. Wang, J. Li, H. Song, H. Huang, and J. Gou, "Highly stretchable and wearable strain sensor based on printable carbon nanotube layers/polydimethylsiloxane composites with adjustable sensitivity," *ACS applied materials & interfaces,* vol. 10, no. 8, pp. 7371-7380, 2018.

[176] X. Li, K. H. Koh, M. Farhan, and K. W. C. Lai, "An ultraflexible polyurethane yarn-based wearable strain sensor with a polydimethylsiloxane infiltrated multilayer sheath for smart textiles," *Nanoscale,* vol. 12, no. 6, pp. 4110-4118, 2020.

[177] Z. Pei *et al.*, "Highly sensitive, stretchable strain sensor based on Ag@ COOH-functionalized CNTs for stroke and pronunciation recognition," *Advanced Electronic Materials,* vol. 5, no. 7, p. 1900227, 2019.

[178] M. Soni and R. Dahiya, "Soft Eskin: Distributed Touch Sensing with Harmonized Energy and Computing," *Philos. Trans. R. Soc., A,* vol. 378, p. 20190156, 2020.

[179] F. Liu, W. T. Navaraj, N. Yogeswaran, D. H. Gregory, and R. Dahiya, "van der Waals Contact Engineering of Graphene Field-Effect Transistors for Large-Area Flexible Electronics," *ACS Nano,* vol. 13, no. 3, pp. 3257-3268, 2019/03/05 2019.

[180] Y. Liu *et al.*, "Strain-Isolation Bridge Structure to Improve Stretchability of Highly Sensitive Strain Sensors," *Advanced Materials Technologies,* vol. 4, no. 9, p. 1900309, 2019/09/01 2019.

[181] N. Doumit and G. Poulin-Vittrant, "A New Simulation Approach for Performance Prediction of Vertically Integrated Nanogenerators," *Advanced Theory and Simulations,* vol. 1, no. 6, p. 1800033, 2018.

[182] S. Xu, O. Rezvanian, K. Peters, and M. A. Zikry, "The Viability and Limitations of Percolation Theory in Modeling the Electrical Behavior of Carbon Nanotube–Polymer Composites," *Nanotechnology,* vol. 24, p. 155706, 2013.

[183] S. Luo *et al.*, "Tunable-sensitivity flexible pressure sensor based on graphene transparent electrode," *solid-state electronics,* vol. 145, pp. 29-33, 2018.

[184] B. He, Z. Yan, Y. Zhou, J. Zhou, Q. Wang, and Z. Wang, "FEM and experimental studies of flexible pressure sensors with micro-structured dielectric layers," *Journal of Micromechanics and Microengineering,* vol. 28, no. 10, 2018.

[185] J. Han, Z. Li, W. Zheng, and Y. Zhang, "Hardware Implementation of Spiking Neural Networks on FPGA," *Tsinghua Sci. Technol.*, vol. 25, p. 479, 2020.

[186] N. Salimi-Nezhad, M. Amiri, E. Falotico, and C. Laschi, "A Digital Hardware Realization for Spiking Model of Cutaneous Mechanoreceptor," *Front Neurosci*, vol. 12, p. 322, 2018.

[187] S. Chun, W. Son, H. Kim, S. K. Lim, C. Pang, and C. Choi, "Self-Powered Pressure- and Vibration-Sensitive Tactile Sensors for Learning Technique-Based Neural Finger Skin," *Nano Letters*, vol. 19, no. 5, pp. 3305-3312, 2019/05/08 2019.

[188] S. Chun *et al.*, "An artificial neural tactile sensing system," *Nature Electronics*, vol. 4, no. 6, pp. 429-438, 2021/06/01 2021.

[189] B. P. Delhaye, X. Xia, and S. J. Bensmaia, "Rapid geometric feature signaling in the simulated spiking activity of a complete population of tactile nerve fibers," *J Neurophysiol*, vol. 121, no. 6, pp. 2071-2082, Jun 1 2019.

[190] B. Rostamian *et al.*, "Texture recognition based on multi-sensory integration of proprioceptive and tactile signals," *Scientific Reports*, vol. 12, no. 1, p. 21690, 2022/12/15 2022.

[191] D. Sengupta, M. Mastella, E. Chicca, and A. G. P. Kottapalli, "Skin-Inspired Flexible and Stretchable Electrospun Carbon Nanofiber Sensors for Neuromorphic Sensing," *ACS Applied Electronic Materials*, vol. 4, no. 1, pp. 308-315, 2022/01/25 2022.

[192] N. M. Nair, S. Mishra, and R. Dahiya, "Graphene-Based Touch Sensors," in *Encyclopedia of Materials: Electronics*, A. S. M. A. Haseeb, Ed. Oxford: Academic Press, 2023, pp. 54-70.

[193] W. Navaraj and R. Dahiya, "Fingerprint-Enhanced Capacitive-Piezoelectric Flexible Sensing Skin to Discriminate Static and Dynamic Tactile Stimuli," *Advanced Intelligent Systems*, https://doi.org/10.1002/aisy.201900051 vol. 1, no. 7, p. 1900051, 2019/11/01 2019.

[194] P. Escobedo, M. Bhattacharjee, F. Nikbakhtnasrabadi, and R. Dahiya, "Flexible Strain and Temperature Sensing NFC Tag for Smart Food Packaging Applications," *IEEE Sensors Journal,* vol. 21, no. 23, pp. 26406-26414, 2021.

[195] P. Escobedo, M. Bhattacharjee, F. Nikbakhtnasrabadi, and R. Dahiya, "Smart Bandage With Wireless Strain and Temperature Sensors and Batteryless NFC Tag," *IEEE Internet of Things Journal,* vol. 8, no. 6, pp. 5093-5100, 2021.

[196] T. Huang *et al.*, "Porous Fibers Composed of Polymer Nanoball Decorated Graphene for Wearable and Highly Sensitive Strain Sensors," *Adv. Funct. Mater.*, vol. 29, p. 1903732, 2019.

[197] P. Karipoth, A. Christou, A. Pullanchiyodan, and R. Dahiya, "Bioinspired Inchworm- and Earthworm-like Soft Robots with Intrinsic Strain Sensing," *Advanced Intelligent Systems*, vol. 4, no. 2, p. 2100092, 2022.

[198] D. Sengupta *et al.*, "Single and Bundled Carbon Nanofibers as Ultralightweight and Flexible Piezoresistive Sensors," *npj Flex. Electron.*, vol. 4, p. 9, 2020.

[199] C. X. Liu and J. W. Choi, "An Embedded PDMS Nanocomposite Strain Sensor toward Biomedical Application," *31st Ann. Int. Conf. IEEE EMBS*, p. 6391, 2009.

[200] M. Amjadi, A. Pichitpajongkit, S. Lee, S. Ryu, and I. Park, "Highly Stretchable and Sensitive Strain Sensor Based on Silver Nanowire–Elastomer Nanocomposite," *ACS Nano,* vol. 8, no. 5, pp. 5154-5163, 2014/05/27 2014.

[201] W. Li, J. Guo, and D. Fan, "3D Graphite–Polymer Flexible Strain Sensors with Ultrasensitivity and Durability for Real-Time Human Vital Sign Monitoring and Musical Instrument Education," *Advanced Materials Technologies,* vol. 2, no. 6, p. 1700070, 2017/06/01 2017.

[202] P. Karipoth, A. Christou, A. Pullanchiyodan, and R. Dahiya, "Bioinspired Inchworm- and Earthworm-like Soft Robots with Intrinsic Strain Sensing," *Advanced Intelligent Systems*, 2021.

[203] A. Pullanchiyodan, L. Manjakkal, M. Ntagios, and R. Dahiya, "MnOx-Electrodeposited Fabric-Based Stretchable Supercapacitors with Intrinsic Strain Sensing," *ACS Applied Materials & Interfaces*, vol. 13, no. 40, pp. 47581-47592, 2021/10/13 2021.

[204] S. Hsiao, "Central mechanisms of tactile shape perception," *Curr Opin Neurobiol,* vol. 18, no. 4, pp. 418-24, Aug 2008.

[205] A. P. Thompson *et al.,* "LAMMPS - a flexible simulation tool for particle-based materials modeling at the atomic, meso, and continuum scales," *Computer Physics Communications,* vol. 271, p. 108171, 2022/02/01/ 2022.

[206] W. L. Jorgensen, D. S. Maxwell, and J. Tirado-Rives, "Development and Testing of the OPLS All-Atom Force Field on Conformational Energetics and Properties of Organic Liquids," *Journal of the American Chemical Society,* vol. 118, no. 45, pp. 11225-11236, 1996/11/13 1996.

[207] V. Selen, Ö. Güler, D. Özer, and E. Evin, "Synthesized multi-walled carbon nanotubes as a potential adsorbent for the removal of methylene blue dye: kinetics, isotherms, and thermodynamics," *Desalination and Water Treatment,* vol. 57, no. 19, pp. 8826-8838, 2016/04/01/ 2016.

[208] Y. Zare and K. Y. Rhee, "Expression of characteristic tunneling distance to control the electrical conductivity of carbon nanotubes-reinforced nanocomposites," *Journal of Materials Research and Technology,* vol. 9, no. 6, pp. 15996-16005, 2020/11/01/ 2020.

[209] Z.-Y. Li *et al.,* "An Ultrasensitive, Durable and Stretchable Strain Sensor with Crack-wrinkle Structure for Human Motion Monitoring," *Chinese Journal of Polymer Science,* vol. 39, no. 3, pp. 316-326, 2021/03/01 2021.

[210] H. Joodaki and M. B. Panzer, "Skin mechanical properties and modeling: A review," *Proceedings of the Institution of Mechanical Engineers, Part H: Journal of Engineering in Medicine,* vol. 232, no. 4, pp. 323-343, 2018.

[211] A. Buganza Tepole, A. K. Gosain, and E. Kuhl, "Stretching skin: The physiological limit and beyond," *International Journal of Non-Linear Mechanics,* vol. 47, no. 8, pp. 938-949, 2012/10/01/ 2012.

[212] P. Slavík and J. Bell, "A mechanoreceptor model for rapidly and slowly adapting afferents subjected to periodic vibratory stimuli," *Mathematical Biosciences,* vol. 130, no. 1, pp. 1-23, 1995/11/01/ 1995.

[213] Y. Kumaresan, S. Mishra, O. Ozioko, R. Chirila, and R. Dahiya, "Ultra-High Gauge Factor Strain Sensor with Wide-Range Stretchability," *Advanced Intelligent Systems,* https://doi.org/10.1002/aisy.202200043 vol. n/a, no. n/a, p. 2200043, 2022/06/16 2022.

[214] N. P. Maria Joseph Raj, N. R. Alluri, A. Chandrasekhar, G. Khandelwal, and S.-J. Kim, "Self-powered ferroelectric NTC thermistor based on bismuth titanate," *Nano Energy,* vol. 62, pp. 329-337, 2019/08/01/ 2019.

[215] V. Vivekananthan, N. R. Alluri, A. Chandrasekhar, Y. Purusothaman, A. Gupta, and S.-J. Kim, "Zero-power consuming intruder identification system by enhanced piezoelectricity of K0.5Na0.5NbO3 using substitutional doping of BTO NPs," *Journal of Materials Chemistry C,* 10.1039/C8TC06626D vol. 7, no. 25, pp. 7563-7571, 2019.

[216] M. N. Biutty, J. M. Koo, M. Zakia, P. L. Handayani, U. H. Choi, and S. I. Yoo, "Dielectric control of porous polydimethylsiloxane elastomers with Au nanoparticles for enhancing the output performance of triboelectric nanogenerators," *RSC Advances,* 10.1039/D0RA03522J vol. 10, no. 36, pp. 21309-21317, 2020.

[217] Z. He, Y. Zhuo, J. He, and Z. Zhang, "Design and preparation of sandwich-like polydimethylsiloxane (PDMS) sponges with super-low ice adhesion," *Soft Matter,* 10.1039/C8SM00820E vol. 14, no. 23, pp. 4846-4851, 2018.

[218] D. Zhu, S. Handschuh-Wang, and X. Zhou, "Recent progress in fabrication and application of polydimethylsiloxane sponges," *Journal of Materials Chemistry A,* 10.1039/C7TA04577H vol. 5, no. 32, pp. 16467-16497, 2017.

[219] D. Kwon *et al.*, "Highly Sensitive, Flexible, and Wearable Pressure Sensor Based on a Giant Piezocapacitive Effect of Three-Dimensional Microporous Elastomeric Dielectric Layer," *ACS Applied Materials & Interfaces,* vol. 8, no. 26, pp. 16922-16931, 2016/07/06 2016.

[220] L. Ma *et al.*, "Highly sensitive flexible capacitive pressure sensor with a broad linear response range and finite element analysis of micro-array electrode," *Journal of Materiomics,* vol. 6, no. 2, pp. 321-329, 2020.

[221] H. Wang *et al.*, "Flexible capacitive pressure sensors for wearable electronics," *Journal of Materials Chemistry C*, 10.1039/D1TC05304C vol. 10, no. 5, pp. 1594-1605, 2022.

[222] A. R. Tripathy *et al.*, "Polymer matrix composite engineering for PDMS based capacitive sensors to achieve high-performance and broad-range pressure sensing," *Applied Surface Science Advances*, vol. 3, p. 100062, 2021/03/01/ 2021.

[223] J. Zhou, X. Gou, D. Fan, J. Wang, and Z. Wan, "Polydimethylsiloxane/BaTiO3 Nanogenerators with a Surface-Assembled Mosaic Structure for Enhanced Piezoelectric Sensing," *ACS Applied Materials & Interfaces*, vol. 14, no. 33, pp. 38105-38115, 2022/08/24 2022.

[224] S. C. B. Mannsfeld *et al.*, "Highly sensitive flexible pressure sensors with microstructured rubber dielectric layers," *Nature Materials*, vol. 9, no. 10, pp. 859-864, 2010/10/01 2010.

[225] S. Y. Liu, J. G. Lu, and H. P. D. Shieh, "Influence of Permittivity on the Sensitivity of Porous Elastomer-Based Capacitive Pressure Sensors," *IEEE Sensors Journal*, vol. 18, no. 5, pp. 1870-1876, 2018.

[226] R. Y. Tay *et al.*, "Lightweight, Superelastic Boron Nitride/Polydimethylsiloxane Foam as Air Dielectric Substitute for Multifunctional Capacitive Sensor Applications," *Advanced Functional Materials*, vol. 30, no. 10, p. 1909604, 2020.

[227] N. Doumit and G. Poulin-Vittrant, "Effect of the Dielectric and Mechanical Properties of the Polymer Matrix on ZnO-Nanowire-Based Composite Nanogenerators Performance," *Advanced Theory and Simulations*, vol. 3, no. 9, 2020.

[228] S. Ma, Y. Kumaresan, O. Ozioko, and R. Dahiya, "Highly Sensitive Flexible Capacitive Pressure Sensor with ZnO NW interlayers," in *2021 IEEE International Conference on Flexible and Printable Sensors and Systems (FLEPS)*, 2021, pp. 1-4.

[229] P. Kumar and J. Srinivas, "Numerical evaluation of effective elastic properties of CNT-reinforced polymers for interphase effects," *Computational Materials Science*, vol. 88, pp. 139-144, 2014/06/01/ 2014.

[230] F. Aghadavoudi, H. Golestanian, and Y. Tadi Beni, "Investigating the effects of CNT aspect ratio and agglomeration on elastic constants of crosslinked polymer nanocomposite using multiscale modeling," *Polymer Composites*, https://doi.org/10.1002/pc.24557 vol. 39, no. 12, pp. 4513-4523, 2018/12/01 2018.

[231] U. Galan, Y. Lin, G. J. Ehlert, and H. A. Sodano, "Effect of ZnO nanowire morphology on the interfacial strength of nanowire coated carbon fibers," *Composites Science and Technology*, vol. 71, no. 7, pp. 946-954, 2011/05/04/ 2011.

[232] V. F. Rivera *et al.*, "Length-Dependent Charge Generation from Vertical Arrays of High-Aspect-Ratio ZnO Nanowires," *Chemistry – A European Journal*, https://doi.org/10.1002/chem.201204429 vol. 19, no. 43, pp. 14665-14674, 2013/10/18 2013.

[233] G. Khandelwal, S. Deswal, D. Shakthivel, and R. Dahiya, "Recent developments in 2D materials for energy harvesting applications," *Journal of Physics: Energy*, 2023.

[234] A. Paul, N. Yogeswaran, and R. Dahiya, "Ultra-Flexible Biodegradable Pressure Sensitive Field Effect Transistors for Hands-Free Control of Robot Movements," *Advanced Intelligent Systems*, vol. 4, no. 11, p. 2200183, 2022.

[235] N. Yogeswaran, E. S. Hosseini, and R. Dahiya, "Graphene Based Low Voltage Field Effect Transistor Coupled with Biodegradable Piezoelectric Material Based Dynamic Pressure Sensor," *ACS Applied Materials & Interfaces*, vol. 12, no. 48, pp. 54035-54040, 2020/12/02 2020.

[236] P. K. Dubey, N. Yogeswaran, F. Liu, A. Vilouras, B. K. Kaushik, and R. Dahiya, "Monolayer $MoSe_2$-based tunneling field effect transistor for ultrasensitive strain sensing," *IEEE Transactions on Electron Devices*, vol. 67, no. 5, pp. 2140-2146, 2020.

[237] S. Z. Butler *et al.*, "Progress, Challenges, and Opportunities in Two-Dimensional Materials Beyond Graphene," *ACS Nano*, vol. 7, no. 4, pp. 2898-2926, 2013/04/23 2013.

[238] D. Jariwala, T. J. Marks, and M. C. Hersam, "Mixed-dimensional van der Waals heterostructures," *Nature Materials*, vol. 16, no. 2, pp. 170-181, 2017/02/01 2017.

[239] A. K. Geim and I. V. Grigorieva, "Van der Waals heterostructures," *Nature*, vol. 499, no. 7459, pp. 419-425, 2013/07/01 2013.

[240] Y. Gong *et al.*, "Vertical and in-plane heterostructures from WS2/MoS2 monolayers," *Nature Materials*, vol. 13, no. 12, pp. 1135-1142, 2014/12/01 2014.

[241] K. S. Novoselov, A. Mishchenko, A. Carvalho, and A. H. Castro Neto, "2D materials and van der Waals heterostructures," *Science*, vol. 353, no. 6298, p. aac9439, 2016/07/29 2016.

[242] S. Susarla *et al.*, "Deformation Mechanisms of Vertically Stacked WS2 /MoS2 Heterostructures: The Role of Interfaces," *ACS Nano*, vol. 12, no. 4, pp. 4036-4044, 2018/04/24 2018.

[243] G. R. Bhimanapati *et al.*, "Recent Advances in Two-Dimensional Materials beyond Graphene," *ACS Nano*, vol. 9, no. 12, pp. 11509-11539, 2015/12/22 2015.

[244] Y.-C. Shen *et al.*, "Rational Design on Wrinkle-Less Transfer of Transition Metal Dichalcogenide Monolayer by Adjustable Wettability-Assisted Transfer Method," *Advanced Functional Materials*, vol. 31, no. 45, p. 2104978, 2021.

[245] J. Zhang *et al.*, "Clean Transfer of Large Graphene Single Crystals for High-Intactness Suspended Membranes and Liquid Cells," *Advanced Materials*, https://doi.org/10.1002/adma.201700639 vol. 29, no. 26, p. 1700639, 2017/07/01 2017.

[246] H. H. Kim, S. K. Lee, S. G. Lee, E. Lee, and K. Cho, "Wetting-Assisted Crack- and Wrinkle-Free Transfer of Wafer-Scale Graphene onto Arbitrary Substrates over a Wide Range of Surface Energies," *Advanced Functional Materials*, https://doi.org/10.1002/adfm.201504551 vol. 26, no. 13, pp. 2070-2077, 2016/04/01 2016.

[247] W. Gao, K. M. Liechti, and R. Huang, "Wet adhesion of graphene," *Extreme Mechanics Letters*, vol. 3, pp. 130-140, 2015.

[248] G. Zhao *et al.*, "The physics and chemistry of graphene-on-surfaces," *Chem Soc Rev*, vol. 46, no. 15, pp. 4417-4449, Jul 31 2017.

[249] X. F. Fan, W. T. Zheng, V. Chihaia, Z. X. Shen, and J. L. Kuo, "Interaction between graphene and the surface of SiO2," *J Phys Condens Matter,* vol. 24, no. 30, p. 305004, Aug 1 2012.

[250] P. Cao, J. O. Varghese, K. Xu, and J. R. Heath, "Visualizing local doping effects of individual water clusters on gold(111)-supported graphene," *Nano Lett,* vol. 12, no. 3, pp. 1459-63, Mar 14 2012.

[251] T. O. Wehling, A. I. Lichtenstein, and M. I. Katsnelson, "First-principles studies of water adsorption on graphene: The role of the substrate," *Applied Physics Letters,* vol. 93, no. 20, p. 202110, 2008/11/17 2008.

[252] O. Leenaerts, B. Partoens, and F. M. Peeters, "Water on graphene: Hydrophobicity and dipole moment using density functional theory," *Physical Review B,* vol. 79, no. 23, p. 235440, 06/29/ 2009.

[253] Y. Huang *et al.*, "Universal mechanical exfoliation of large-area 2D crystals," *Nature Communications,* vol. 11, no. 1, p. 2453, 2020/05/15 2020.

[254] S. E. Panasci *et al.*, "Substrate impact on the thickness dependence of vibrational and optical properties of large area MoS2 produced by gold-assisted exfoliation," *Applied Physics Letters,* vol. 119, no. 9, 2021.

[255] M. Velický *et al.*, "Mechanism of Gold-Assisted Exfoliation of Centimeter-Sized Transition-Metal Dichalcogenide Monolayers," *ACS Nano,* vol. 12, no. 10, pp. 10463-10472, 2018/10/23 2018.

[256] S. E. Panasci *et al.*, "Strain, Doping, and Electronic Transport of Large Area Monolayer MoS2 Exfoliated on Gold and Transferred to an Insulating Substrate," *ACS Applied Materials & Interfaces,* vol. 13, no. 26, pp. 31248-31259, 2021/07/07 2021.

[257] P. Bampoulis, K. Sotthewes, E. Dollekamp, and B. Poelsema, "Water confined in two-dimensions: Fundamentals and applications," *Surface Science Reports,* vol. 73, no. 6, pp. 233-264, 2018.

[258] K. Koga and H. Tanaka, "Phase diagram of water between hydrophobic surfaces," *J Chem Phys,* vol. 122, no. 10, p. 104711, Mar 8 2005.

[259] F. Corsetti, P. Matthews, and E. Artacho, "Structural and configurational properties of nanoconfined monolayer ice from first principles," *Scientific Reports,* vol. 6, no. 1, p. 18651, 2016/01/05 2016.

[260] J. Chen, G. Schusteritsch, C. J. Pickard, C. G. Salzmann, and A. Michaelides, "Double-layer ice from first principles," *Physical Review B,* vol. 95, no. 9, p. 094121, 03/31/ 2017.

[261] Y. Zhu, F. Wang, J. Bai, X. C. Zeng, and H. Wu, "Compression Limit of Two-Dimensional Water Constrained in Graphene Nanocapillaries," *ACS Nano,* vol. 9, no. 12, pp. 12197-12204, 2015/12/22 2015.

[262] G. Algara-Siller *et al.*, "Square ice in graphene nanocapillaries," *Nature,* vol. 519, no. 7544, pp. 443-445, 2015/03/01 2015.

[263] E. J. Olson *et al.*, "Capacitive Sensing of Intercalated H2O Molecules Using Graphene," *ACS Applied Materials & Interfaces,* vol. 7, no. 46, pp. 25804-25812, 2015/11/25 2015.

[264] J. R. Werber, C. O. Osuji, and M. Elimelech, "Materials for next-generation desalination and water purification membranes," *Nature Reviews Materials,* vol. 1, no. 5, p. 16018, 2016/04/05 2016.

[265] T. A. Pascal, C. P. Schwartz, K. V. Lawler, and D. Prendergast, "The purported square ice in bilayer graphene is a nanoscale, monolayer object," *J Chem Phys,* vol. 150, no. 23, p. 231101, Jun 21 2019.

[266] L. Ruiz Pestana, L. E. Felberg, and T. Head-Gordon, "Coexistence of Multilayered Phases of Confined Water: The Importance of Flexible Confining Surfaces," *ACS Nano,* vol. 12, no. 1, pp. 448-454, Jan 23 2018.

[267] S. Kawai *et al.*, "Superlubricity of graphene nanoribbons on gold surfaces," *Science,* vol. 351, no. 6276, pp. 957-61, Feb 26 2016.

[268] L. Gigli *et al.*, "Detachment Dynamics of Graphene Nanoribbons on Gold," *ACS Nano,* vol. 13, no. 1, pp. 689-697, Jan 22 2019.

[269] M. Yortanli and E. Mete, "Common surface structures of graphene and Au(111): The effect of rotational angle on adsorption and electronic properties," *J Chem Phys,* vol. 151, no. 21, p. 214701, Dec 7 2019.

[270] W. Gao, P. Xiao, G. Henkelman, K. M. Liechti, and R. Huang, "Interfacial adhesion between graphene and silicon dioxide by density functional theory with van der Waals corrections," *Journal of Physics D: Applied Physics*, vol. 47, no. 25, 2014.

[271] C. Gong, G. Lee, B. Shan, E. M. Vogel, R. M. Wallace, and K. Cho, "First-principles study of metal–graphene interfaces," *Journal of Applied Physics*, vol. 108, no. 12, 2010.

[272] G. Giovannetti, P. A. Khomyakov, G. Brocks, V. M. Karpan, J. van den Brink, and P. J. Kelly, "Doping graphene with metal contacts," *Phys Rev Lett*, vol. 101, no. 2, p. 026803, Jul 11 2008.

[273] L. Martínez, R. Andrade, E. G. Birgin, and J. M. Martínez, "PACKMOL: A package for building initial configurations for molecular dynamics simulations," *Journal of Computational Chemistry*, https://doi.org/10.1002/jcc.21224 vol. 30, no. 13, pp. 2157-2164, 2009/10/01 2009.

[274] M. S. Daw and M. I. Baskes, "Embedded-atom method: Derivation and application to impurities, surfaces, and other defects in metals," *Physical Review B*, vol. 29, no. 12, pp. 6443-6453, 06/15/ 1984.

[275] M. W. Finnis and J. E. Sinclair, "A simple empirical N-body potential for transition metals," *Philosophical Magazine A*, vol. 50, no. 1, pp. 45-55, 1984/07/01 1984.

[276] D. W. Brenner, O. A. Shenderova, J. A. Harrison, S. J. Stuart, B. Ni, and S. B. Sinnott, "A second-generation reactive empirical bond order (REBO) potential energy expression for hydrocarbons," *Journal of Physics: Condensed Matter*, vol. 14, no. 4, pp. 783-802, 2002/01/18 2002.

[277] H. J. C. Berendsen, J. R. Grigera, and T. P. Straatsma, "The missing term in effective pair potentials," *The Journal of Physical Chemistry*, vol. 91, no. 24, pp. 6269-6271, 1987/11/01 1987.

[278] H. Ghorbanfekr, J. Behler, and F. M. Peeters, "Insights into Water Permeation through hBN Nanocapillaries by Ab Initio Machine Learning Molecular

Dynamics Simulations," *The Journal of Physical Chemistry Letters,* vol. 11, no. 17, pp. 7363-7370, 2020/09/03 2020.

[279] A. Stukowski, "Visualization and analysis of atomistic simulation data with OVITO–the Open Visualization Tool," *Modelling and Simulation in Materials Science and Engineering,* vol. 18, no. 1, p. 015012, 2009/12/15 2009.

[280] K. Xu, P. Cao, and J. R. Heath, "Graphene Visualizes the First Water Adlayers on Mica at Ambient Conditions," *Science,* vol. 329, no. 5996, pp. 1188-1191, 2010/09/03 2010.

[281] J. Song *et al.,* "Evidence of Stranski–Krastanov growth at the initial stage of atmospheric water condensation," *Nature Communications,* vol. 5, no. 1, p. 4837, 2014/09/08 2014.

[282] J. Majumdar, M. Moid, C. Dasgupta, and P. K. Maiti, "Dielectric Profile and Electromelting of a Monolayer of Water Confined in Graphene Slit Pore," *J Phys Chem B,* vol. 125, no. 24, pp. 6670-6680, Jun 24 2021.

[283] J. Kashyap, E. H. Yang, and D. Datta, "Computational study of the water-driven graphene wrinkle life-cycle towards applications in flexible electronics," *Sci Rep,* vol. 10, no. 1, p. 11315, Jul 9 2020.

[284] T. Oznuluer, E. Pince, E. O. Polat, O. Balci, O. Salihoglu, and C. Kocabas, "Synthesis of graphene on gold," *Applied Physics Letters,* vol. 98, no. 18, 2011.

[285] V. Kapil, C. Schran, A. Zen, J. Chen, C. J. Pickard, and A. Michaelides, "The first-principles phase diagram of monolayer nanoconfined water," *Nature,* vol. 609, no. 7927, pp. 512-516, 2022/09/01 2022.

[286] Z. Gao, N. Giovambattista, and O. Sahin, "Phase Diagram of Water Confined by Graphene," *Scientific Reports,* vol. 8, no. 1, p. 6228, 2018/04/18 2018.

[287] S. Xiao, B. H. Skallerud, F. Wang, Z. Zhang, and J. He, "Enabling sequential rupture for lowering atomistic ice adhesion," *Nanoscale,* vol. 11, no. 35, pp. 16262-16269, Sep 21 2019.

[288] S. Ghasemi *et al.,* "Electronic, dielectric, and optical properties of two-dimensional and bulk ice: A multiscale simulation study," *Physical Review B,* vol. 101, no. 18, p. 184202, 05/06/ 2020.